DURBAN UNIVERSITY OF TECHNOLOGY

DEVELOPMENT OF GRANULAR-MEDIUM-BASED ENERGY MANAGEMENT SYSTEM FOR AUTOMOTIVE BUMPER APPLICATIONS

MWANGI FESTUS MAINA

DEVELOPMENT OF GRANULAR-MEDIUM-BASED ENERGY MANAGEMENT SYSTEM FOR AUTOMOTIVE BUMPER APPLICATIONS

A THESIS SUBMITTED TO THE

DURBAN UNIVERSITY OF TECHNOLOGY

FOR THE MASTER OF TECHNOLOGY DEGREE

(IN MECHANICAL ENGINEERING)

BY

MWANGI FESTUS MAINA

DEPARTMENT OF MECHANICAL ENGINEERING

FACULTY OF ENGINEERING AND THE BUILT ENVIRONMENT

DURBAN 4000, SOUTH AFRICA

2009

FINAL APPROVED SUBMISSION

_____ _____

Supervisor (Prof. K. Kanny) Date

DECLARATION

This thesis is being submitted to the Durban University of Technology for the award of the degree of Master of Technology (Mechanical Engineering). I declare that the thesis entitled **"DEVELOPMENT OF GRANULAR-MEDIUM-BASED ENERGY MANAGEMENT SYSTEM FOR AUTOMOTIVE BUMPER APPLICATIONS"** is a record of research work carried out by myself. The content of this thesis, in full or in parts, have not been submitted to any other Institute or University for the award of any degree or diploma.

_____ _____

Signature of Student Date

_____ _____

Signature of Supervisor Date

To my late dad
for believing in me

Acknowledgements

I would like to thank God for affording me His divine guidance, endowing me with passion for my research area and project, will-power to hang on at difficult times, and linking me up with great people without whom the project would not have come to fruition. Of these people, I would like to specially thank Prof. K. Kanny for his selfless all-round support, guidance, constructive criticism, inspiration and motivation through out the research programme. I am forever indebted to him for masterminding and mapping-out the logistics aspect of the programme, right from funding, publicity of progressive output, through to my private life endeavours. Much gratitude also to Dr. J. Paulraj who served as my co-supervisor at the project's inception stage. His brainstorming sessions and motivational support are very much appreciated.

My experience at DUT would not have been as much exciting and rewarding without the helpful discussions and moments shared with my research group colleagues; Mr. A. Ramsaroop, Mr. V. K. Moodley, and Mr. S. Yang. I am grateful for the direct and indirect contribution from Mr. G. Gumede, Mr. S. D. Kazadi, S. P. Naidoo, A. Jugnarayan, N. Bholai, and M. B. Chili.

I am grateful for the enormous support that I have received from DUT staff members and their respective departments. I would like to specially thank Prof. A. Jordaan for her financial support through the post graduate development support (PGDS) directorate without which support this programme would have become just but a pipe dream. Much thanks also to the director of technology transfer and innovation directorate, Prof. G. Prinsloo for facilitating patenting of some of my work. For timely access to publications,

I would like to register my utmost gratitude to Mr. V. Mayela and Ms. H. Dlamini of Steve Biko Campus library. For assistance during experimentation procedures, I want to specially thank Mr. E. Magagane, Mr. P. P. Chamane, J. Veerasamy, and S.V. Nyawo.

I am blessed to have every possible form of support from my small family – thanks to my dear loving wife, Philile, and my kids; Sandiso and Emma. They have been a great well of love, encouragement, motivation, inspiration and understanding especially during difficult moments during my academic pursuits. Much gratitude to my loving mom for having cultured in me a sense of pride in education despite never having been to school herself. Special thanks also go to my mother-in-law for her reliable presence at the centre of my life, being a beacon of support and personal icon of academic excellence. Finally but not the least, I want to thank my distant sister, brothers, relatives and friends who have indirectly contributed to the programme's success.

May the almighty God bless you all.

TABLE OF CONTENTS

LIST OF FIGURES

LIST OF TABLES

LIST OF ABBREVIATIONS

ABREVIATION	
FMVSS	Federal Motor Vehicle Safety Standards
TPO	Thermoplastic Olefin
RIM	Reaction-Injection Moulding
GM	General Motors (Corporation)
SRIM	Structural Reaction Injection Moulding
EPP	Expanded Polypropylene
EVA	Ethylene Vinyl Acetate
ETP	Engineering Thermoplastic
PC	Polycarbonate
PBT	Polybutylene Telephthalate
EA	Energy Absorber
BBS	Beamless Bumper System
MDO	Multidesign Optimization (Technique)
MPa	Megapascals
UK	United Kingdom
USA	United States of America
GNP	Gross National Product
NASA	National Aeronautics and Space Administration
MGM	Mechanics of Granular Material (Experiment)
CT	Computed Tomography (Scan)
BCC	Body Centred Cubic
FCC	Face Centred Cubic

ASTM	American Society for Testing and Materials
PP	Polypropylene
ISO	International Standards Organization
DEM	Discrete Element Modeling
d.i.a	Distance from Incidence Axis
CMVSS	Canadian Motor Vehicle Safety Standards

ABSTRACT

Automotive bumpers are installed primarily to minimize damage and harm to both the automobile and passengers during minor and low speed collisions. The efficacy of the current bumper systems lies in absorbing the impact energy. The primary mechanism for energy absorption is damage.

In this study an attempt is made to shift from this traditional design platform by exploring non-destructive energy dissipation mechanisms. In pursuit of this, an alternative bumper system that simulates human-arm ergonomic response to impact has been proposed. The system capitalizes on the characteristic dissipative mechanics of granular media.

A mathematical model describing the dissipative mechanics of the system is presented. The model shows that granular media can be used effectively to re-direct the impulse wave away from its axis of incidence. The resulting effect is that the impulse wave is attenuated through the thickness. A second mathematical model, based on the Concept of Energy Balance has been developed. Here, the total impact energy is shown to be absorbed or dissipated by the individual components of the system. The largest component of this energy is taken up by sliding and rotation of the granular media. Both models are validated by experimentation.

A prototype system has been built and tested. The system effectively manages impact energy with minimal or no damage to the constituent components. The system demonstrates an ability to recover dimensionally when loaded under FMVSS conditions.

CHAPTER 1:

INTRODUCTION

1.1. Automotive Bumpers

Automotive bumpers are primarily installed to protect both the car and the passengers from incurring too much damage during minor and low speed collisions. They are expected to absorb as much shock as they can during such accidents or collisions [1]. Front and rear bumpers became standard equipment on all cars as early as back in 1925 [2]. Significant advancements have taken place over the years. In the 50's the concentration was in making bumpers shinier and bigger. In the 90's, looking good was only a small part of the job; bumpers not only had to be attractive and accentuating the rest of the vehicle's lines, but in most cases they had to absorb 8Km/h impacts without damage, in addition to cutting weight and costs [3].

One of the most frequently replaced and repaired automobile part is the bumper [4]. A good bumper system is expected to withstand low speed impacts without damage to safety systems, viz, lights, brakes and steering systems.

Most bumpers are composed of three basic components: (1) an outer skin, (2) a rigid inner beam of steel, aluminium, or reinforced plastic, and (3) an energy absorber of some sort [3]. These components are however, functionally interdependent and may thus be treated and/or analyzed as a system.

1.1.1. The Outer Skin

The outer skin is mainly for aesthetic purposes and has received enormous progressive

research efforts. The majority of modern plastic car bumper system fascias are made of thermoplastic olefins, polycarbonates, polyesters, polypropylene, polyurethanes, polyamides, or blend of these with, for instance, glass fibers, for strength and structural rigidity [2]. Bumper covers made from low-cost injection molded thermoplastic olefins (TPOs) have gained market share from reaction-injection moulded (RIM) urethanes in applications where bumpers do not have to be painted and perfectly match the colour of the rest of the body [3]. It is estimated that 93% of fascias are made of TPO - this material is high gloss, has thin wall capability, improved paintability, and low coefficient of thermal expansion [5].

1.1.2. Inner Beam

Heavy-duty steel used to be the preferred material for manufacture of bumpers, as they have great tolerance against crushes and collisions [1]. Due to weight and costs limitations, bumpers have been made of rubber, lightweight metals such as aluminium, or plastic. However, most of these lightweight bumper systems had to be equipped with hydraulic or pneumatic cylinders for shock absorbing purposes [1]. Notable progress has been made in weight and costs optimization efforts without necessarily compromising the functional requirements.

For instance, GM's 1997 Saturn Coupe model saw the introduction of an injection molded one-piece bumper beam that could meet stringent performance requirements; it passed the 8km/h pole impact tests by optimizing rib placement and thickness in the centre of the beam. Weight was reduced by 2.5 pounds, in addition to cost reduction [2]. Further costs savings were realized in assembly through elimination of 13 parts from previous designs.

Lightweight composite Structural Reaction Injection Moulded (SRIM) bumper beams trimmed 15kg off the Buick Road Master [3]. The use of SRIM bumper beams have not grown as fast as initially hoped, in part because most automotive moulders lack the expertise required to make SRIM parts.

1.1.3. Energy Absorbers

Energy absorber designs may store or dissipate energy [7]. Storing implies a subsequent return of the impact energy in a rebound reaction (for example, springs). Dissipation on the other hand can be either destructive, as in metal flow, or nondestructive, as in shearing of a working fluid. Automobile bumper systems are of maximum value from a performance and aesthetic standpoint only when at the design position, implying "self-restoration" after impact. In some passenger cars, sensors that could reduce the amount of impact to the passengers or warn the vehicle of the impending impact have been used [6].

1.2. Impact Energy Absorption and/or Dissipation Dynamics

From a simplistic view-point, if a system is designed to absorb and/or dissipate impact energy, then its efficiency may be evaluated in terms of the impact energy transfer factor from the incidence surface through to the rear surface. This may be ascertained by using sensors that can measure the variation of stress wave through the system's cross-section. Such factor would be dependent on at least two interdependent parameters, viz, (1.) the *material* from which the different components of the system are made, and (2.) the impact energy absorption and/or dissipation *mechanics*.

The *first* parameter is directly related to systems functional capability. Apparently, in the last millennium, this has been the central focus in the design of impact energy

management systems. It has seen, among others, materials such as steel / aluminium metal, timber, plastics, compressible and incompressible fluids, and rubber being used in the design of automotive bumpers and other impact energy absorbing systems. The essence of selecting a certain material for a particular design context lies in its intrinsic properties. Arguably, the more solid and rigid a material is, the more the impact energy it will transfer through its cross-section. Put in another way, the more deformable a material or design structure is, the greater its impact energy absorption capacity per unit weight.

The *second* parameter on the other hand capitalizes on the aspects of geometry, i.e. form. Several geometrical shapes have been explored to this end, among others, U-sections, frusta, cones, hollow tubes (e.g. Cylindrical, square, e.t.c.) cellular solids (e.g. foam, honeycomb structures, e.t.c), and egg-crates. The essence of geometry in this context lies in its ability to re-direct the incident force vectors, and consequently the transfer factor across the geometrical cross-section.

An optimal impact energy management system should be designed around an optimization process of the two elucidated parameters. Somewhere along the process lies a combination of material and geometry that minimizes the impact energy transfer from the impactor, across the protective system (e.g. bumper), to the shielded object (e.g. a car).

1.3. A Leaf from Mother Nature

Mother-nature has been a great source of many insightful man-made systems. These systems have been derived from scientific processes of trying to emulate natural

phenomena. Examples include robots and other intelligent systems. In this line of thought, an effort has been made toward understanding human behavior in response to external impact forces.

1.3.1. The Human Arm Versus Impact Force

Imagine you are stretching your arm horizontally in front of your face, preparing to stop a falling solid object the size (and shape) of a tennis ball. Figure 1.1 illustrates the scenario.

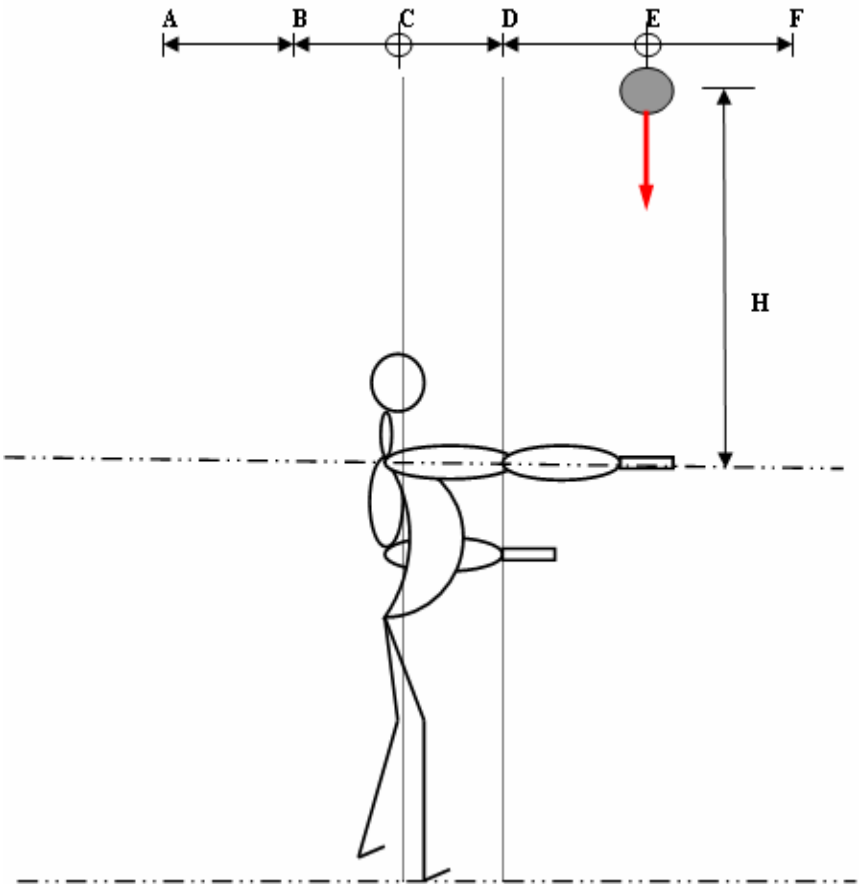

Figure 1.1: Human impact-response phenomenon.

In response to the anticipated impact, there are at least three possibilities:

(1) Direct all your energy to the palm to make it steady enough to stop the ball upon

contact. Figure 1.2 illustrates a person stopping the ball by steadying the arm, which is typical of the traditionally designed bumpers. By stopping the ball, the palm would have absorbed all the impact energy of the ball. This will be accompanied by a significant amount of pain / strain. The shock of the impact will be felt all along the arm's length as it resists a vertical displacement. There are, however, very good chances of a slight downward displacement.

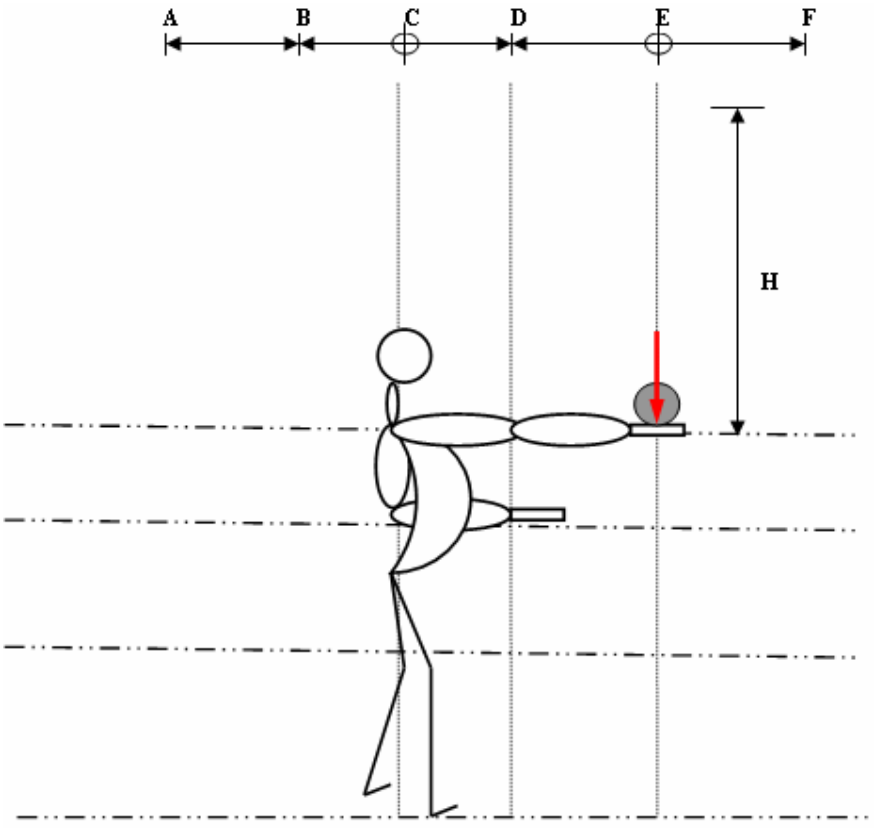

Figure 1.2: Possibility 1 – Stopping a ball by steadying the arm.

(2) Upon contact, contain the ball in the palm instantaneously and simply let the arm to freely swing along path (i) at a radius equivalent to the arm's length. Figure 1.3 illustrates a person stopping the ball by freely swinging the arm along with it. This allows the ball to continue motion in its initial direction, gradually attenuating the impact energy by

gradually re-directing its line of action. Only minimal energy will be required by the arm in bringing the ball to a stand still along the path. Little or no strain will be felt along the arm's length. This strain decreases with the rate of the arm's swing, i.e. velocity being a vector, the strain effect on the arm decreases almost proportionally with the rate of deceleration. The provision for total vertical displacement, d_1, is equivalent to the total arm's length, CDE.

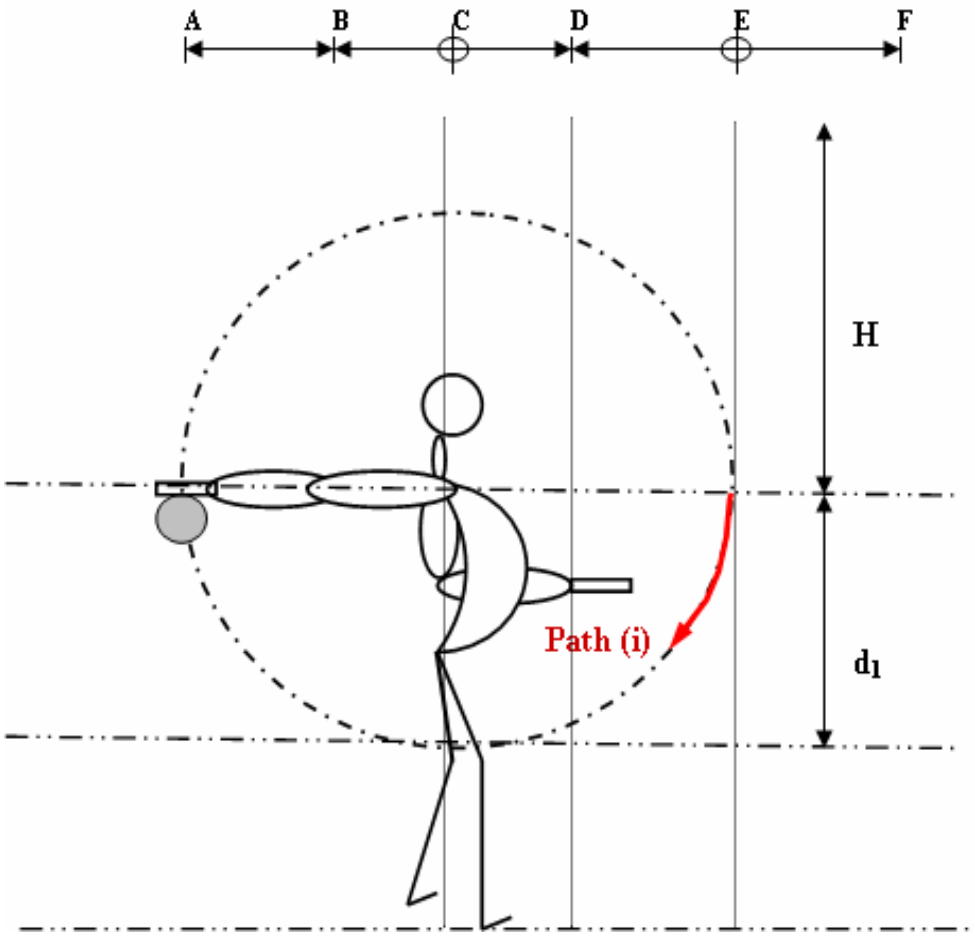

Figure 1.3: Possibility 2 – Stopping a ball by *Freely* swinging the arm.

(3) Upon contact, contain the ball in the palm instantaneously and *consciously* let the arm to swing by flexing it at the elbow as shown in Figure 1.4 below. Notice that the elbow's path will be *circular*, whereas that of the palm (and ball) seems to be *parabolic*, i.e. path

(ii). The effect is, however, almost similar to that in 'Possibility 2' above. Maintaining part DE horizontally will require some energy to resist the force exerted by the ball. Nevertheless, the required resistance is much less than that required in 'Possibility 1'. Further, the provision for total vertical displacement, d_2, is limited to length CD of the arm (Shoulder to the elbow). As noted in possibility two, the higher the rate of the arm's swing, the lesser the strain effect felt by the arm.

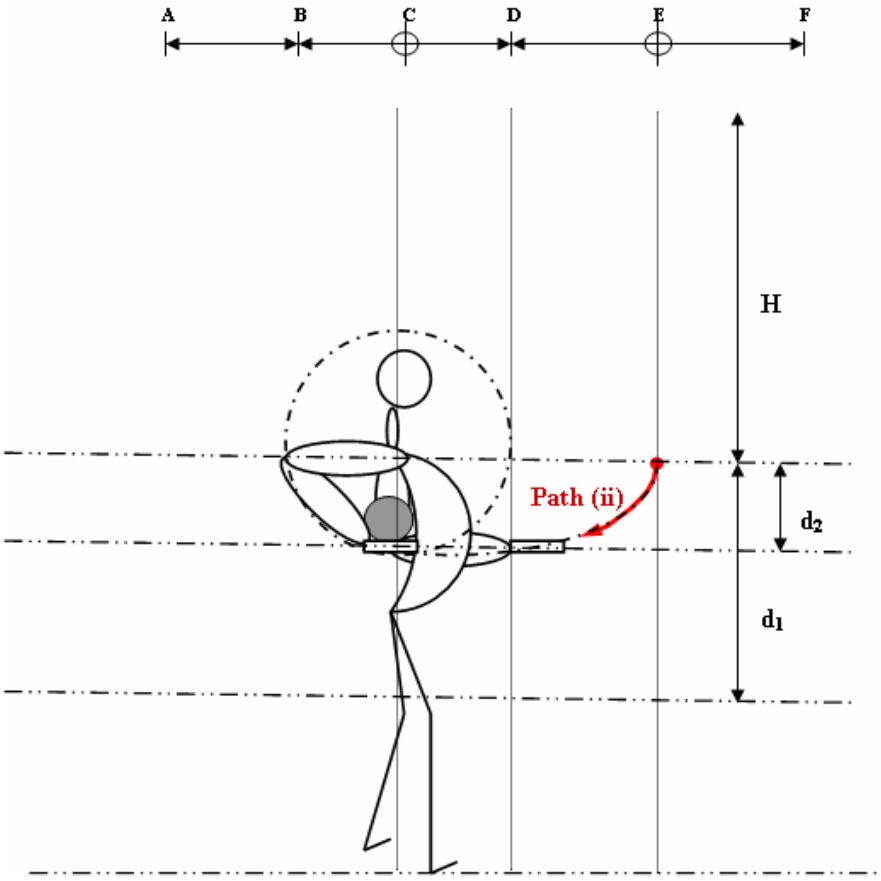

Figure 1.4: Possibility 3 – *Consciously* flexing the arm about the elbow.

By virtue of letting the ball continue motion in its initial direction but re-directing its line of action, this scenario also gradually attenuates the impact energy, as contended in Possibility 2. In light of the strain energy required by the arm, the space and shock effect (stress wave propagation) on the arm, this scenario is the most favorable and/or effective

of the three. Naturally, this is the way a human being responds to an impacting falling object, through reflex action.

1.3.2. Analytical Interpolation

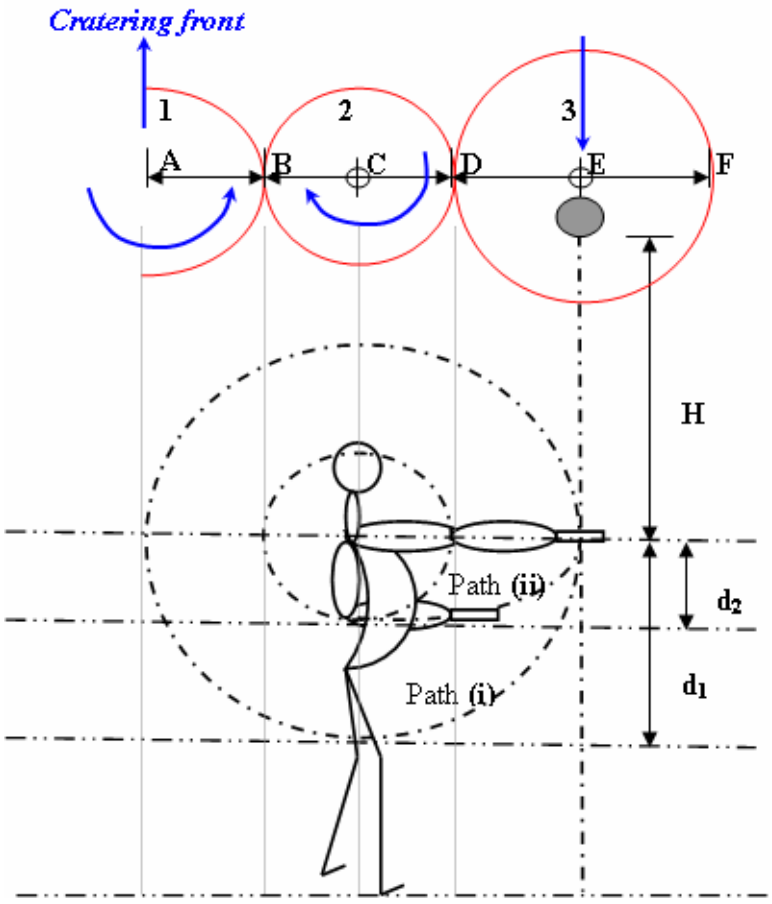

Figure 1.5: Analytical interpolation.

In the context of low velocity impact, an analogy is drawn from analytical extrapolation of possibility three, thereby relating *human ergonomic response* to the *granular medium response.* Figure 1.5 illustrates dimensional relationship between the two. Points BCD conform to the diameter of spherical granule 2, adjacent to another granule 3 with diameter DEF, with centre of mass at E. Angular displacement of the elbow (Point D) conforms to angular displacement of a point D on surface of granule 2 through angular

spinning about its centre in response to a linear vertical displacement of granule 3 through d_2.

Connection between the arm's behavior and granular media may be found by asking the following three questions: *Firstly*, what if the arm had more than one elbow? – If all other factors remain constant, then it would be possible to slice the vertical displacement to a much smaller value than d_2, and such may be the dynamics of stopping a ball using a granular medium like sand. The hypothesized numerous elbows of the arm conform to several equivalent contact points (e.g. B, D, F) between adjacent spherical granules. The arm's muscular energy employed in bringing the ball to stand-still conforms to energy dissipated through granular mechanics such as relative displacement (granular flow), spinning, elastic or inelastic inter-granular collisions (dependent upon material's properties), and inter-granular friction (dependent primarily on the force confining the grains together, if any.

Secondly, as for paths (i) and (ii), what if the arm (or elbow) could swing beyond the initial horizontal level on the rear of the head? – Simplistically, the actual extent of the swing would depend on the weight of the ball, i.e. the magnitude of the incident impact energy. Such behavior is synonymous to the formation of craters in granular media whereby the crater depth and diameter scales with the impact's magnitude.

Lastly, what if the magnitude of the impact energy was to be greater than the arm's critical capacity, bearing in mind that the hand's motion is biologically restrained to the horizontal level at A and B? – Naturally, the arm would release the ball, with the latter tending to spin off the palm with a global horizontal displacement in an effort to maintain

equilibrium. Once the different forms of energy absorption and/or dissipation for a particular granule as exhausted, the surplus energy will be passed on to the adjacent granules, possibly explaining the so called “force chains” characterizing granular medium response to impact forces.

1.3.3. Design Relevance

In light of the three possibilities, sensitivity to “pain” in the arm would be more in possibility 1 than in possibility 2 and 3. It’s worth noting that possibility 3 employs more strength of the arm than possibility 2, but has the advantage of using less space. The arm attenuates the impact energy by gradually re-directing the incident force vector. It is contended that the parabolic physical path of the ball conforms to the global virtual energy dissipation path.

If CD equals DE, both quotients d_1/AE for path (i) and d_2/CE for path (ii) are equal to 0.5. – based on respective initial and final position of the ball. Possibility 3 is a compromise between the other two i.e. it employs more arm’s strength to *control* the situation than possibility 2 does, but has the advantage of using less space, i.e. $\{d_2 \times CE\} - Vs - \{d_1 \times AE\}$. Despite using more space than possibility 1, it employs relatively less strength. It has thus been adopted in this project in modeling of an energy management system for, among others, automotive bumper applications. In that pursuit, a granular medium has been adopted as the core energy absorbing and/or dissipating component in the design process.

CHAPTER 2:

LITERATURE REVIEW

2.1. Introduction

Automotive bumper systems are continually being refined so as to optimize the aesthetics as well as performance. Many researchers have over the last three decades attempted to improve the impact energy management mechanisms of the systems. Review of documented research work to date shows continued interests in harnessing a wide range of engineering materials' properties, including among others, temperature changes, relative density, viscoelastic behaviour, and strain rate. This has been in addition to optimizing the geometrical aspects of the respective designs. In this chapter, a few of the aforementioned research works have been discussed. With granular media as a potential design element in mind owing to its impact energy dissipative characteristics, granular mechanics have also been reviewed in the context of low-to-medium velocity impacts.

2.2. Automotive Bumpers - Design Trend

Several researchers have investigated the impact absorption aspect of automotive bumpers. Most of them, however, have shown great concentration on impact energy *absorption*, with little or no regard to energy *dissipation*. With respect to energy absorption, these researchers have used materials engineering (intrinsic properties) as their core domain. This kind of an approach is, arguably, self-limiting in that it often entails trade-offs between one set of intrinsic materials properties for another. As regards energy dissipation, the dissipative mechanics explored thus far have mainly been destructive in nature, such that self-restoration of the system has ended up being

dispensed with, in addition to elevated repair costs. These dissipative mechanics have ranged from collapsible structures to material's shearing and geometrical inversions.

Going back to history, Keith H. Carpenter and Lamar L. Kerr presented features of the 1973 General Motors hydraulic-pneumatic energy absorber bumper system that dissipated energy and also self-restored [7]. Traditionally, hydraulic shock absorbers have been used to absorb the energy of minor impacts but they have weight and costs limitations [3]. So, increasingly big sections of polystyrene or polyurethane foam or injection moulded thermoplastic "egg crates" have been designed into bumpers to absorb energy without the aid of strokers.

Following is an account of few examples of porous structures as have been applied in the design of automotive bumpers. They all have varied and perfectly justifiable scope of use. However, they do have limitations [8] that cannot be ignored and need be borne in mind while reviewing them, including, (1) polymer-based foams and honeycombs have stress / strain curves that are significantly affected by temperature, age, exposure to ultraviolet light, solvents, and other environmental factors, (2) honeycombs exhibit their characteristic stress / strain curve only if the compression direction is within a few degrees of their orthogonal cell axis, or if they are constrained in a tube to prevent lateral buckling, and (3) honeycombs and closed cell foams trap gasses within their cells, thus adding a pneumatic "spring" effect that not only disrupts the flat crush plateau, but can add a "rebound" behaviour that partially negates the original energy absorption curve.

Despite the aforementioned general shortcomings, it's worth noting contributions towards harnessing properties of lighter engineering materials by researchers such as B.E.

Lampinen and R.A. Jeryan who investigated the effectiveness of polyurethane foam in energy absorbing structures [9]. High density foam was found to be weight effective as a structural reinforcement, but not as an energy absorber. Medium density foam improves the energy absorption capability. Equivalent energy, however, can be absorbed more weight effectively by changing the metal thickness or the foam section size. Based on energy absorbed per unit weight, low density foam proved to be weight ineffective as an energy absorber in typical automotive structures. These findings relate quite well to the microstructure of the foam in that, at high densities, most of the foam cells are closed up, smaller in size, and with more walls material. As such, the global foam structure ends up being relatively more rigid, harder and less resilient. Further, the air so entrapped in the majority closed cells can only exhibit low compression ratios. This is unlike in low and medium foam structures where most cells are open and relatively larger in size, thereby giving increased deformability that mechanically interprets to higher energy absorption capability per unit weight. Complimentary to the deformability concept is the introduction of viscoelastic effect to the flexible polyurethane foam technology, in which case strain rate become an important design factor.

P.R. Stupak and J.A. Donovan proposed a new design procedure and energy absorption models that improve material and absorber geometry selection for given service condition [10]. Design diagram were constructed that showed the energy absorption of uniaxial and trapezoidal absorber geometries as a function of foam density and strain rate for closed cell polyethylene packaging foam. Energy absorption models that were developed generated design data incorporating load spreading, impacting object geometry, polymer deformation and gas compression that agreed within ten percent of measured values.

Peter A. Welter presented concepts and data for the design and application of microcellular urethane foam for absorbing energy in automobile bumpers [11]. Of particular significance was the demonstration of temperature compensation that overcomes the significant variation in modulus with change in temperature that is characteristic of urethane. It was shown that by appropriate design techniques, peak force could be maintained constant even with variations in modulus as high as 6:1.

L.M. Niebylski and R.J. Fanning studied the energy absorption properties of aluminium alloy foams under low and medium speed impact, up to 25mph (40Km/h) [12]. They determined the foam density, volume, and size required for a 5mph (8Km/h) "single shot" impact for two automotive weight classes. They went on to develop non-shearing, columnar, high-density foam structures to withstand basal compressive loads. These columns had the potential for multi-impact shock-absorbing applications.

The most widely used energy absorber construction is made from expanded-polypropylene foam (EPP) [13]. Honeycomb energy absorbers, which are made from an ethylene vinyl acetate (EVA) copolymer, are also still used on some cars. Darin A. Evans and Terry Morgan sought to address an alternative to these bumper energy absorber systems. By using a novel design approach using an engineering thermoplastic (ETP) prototype, they were able to take advantage of the excellent energy absorption properties of the material by maximizing the amount of available material actually involved in attenuating the impact energy. Results of the study and prototype program showed fast load-up and high-energy absorption efficiency compared with EPP foam, suggesting the potential to lower rail loads and minimize the amount of intrusion to the vehicle. The

design was comparable in weight to foam energy absorbers as was projected to be economically competitive. They also reviewed the simulated performance of the prototype ETP energy absorber and compared its actual test results for 8km/h FMVSS Part 581 impact series to the performance of EPP foam packaged in the same environment.

Through a combination of material properties and design, injection-moulded ETP energy absorption systems using polycarbonate/polybutylene terephthalate (PC/PBT) alloys have been shown to promote faster loading and superior energy absorption efficiency than conventional foam systems [14]. This allows the ETP to provide the required impact protection within a smaller package space. In order to make optimal use of this efficiency, the reinforcing beam and energy absorber (EA) must be considered together as an energy management system. Stephen S. et al developed a predictive tool intended to simplify and shorten the process of engineering efficient and cost-effective beam/EA energy management system.

In 2003, Kay Ogiyama et al proposed a Beamless Bumper System (BBS) for small passenger cars in an effort to answer important issues facing the automotive society: cost reduction, higher fuel efficiency, and recyclability [15]. The innovative aspect of the system was to utilize the ability of expanded polypropylene (EPP) as an energy absorber and eliminate the entire metal beam from the bumper system. The system was a semi-module system that consisted of a fascia, an EPP energy absorber, and brackets for assembly to the body. Elimination of the metal beam resulted in weight reduction and better fuel efficiency, while maintaining the key performance criteria. The use of EPP

improves the recyclability of the system. Michael E. Carley made further advancements in EPP foam energy management for bumper systems by introducing new and innovative foam technologies and techniques [16].

Shifting from the energy *absorption* focus, A.A.A. Alghamdi reviewed the use of collapsible impact energy "absorbers" in addition to the different modes of deformation of most of the common ones [18]. The common shapes that have been used include tubes (circular, square, corrugated), frusta, multicorner columns, struts, sandwich plates, honeycomb cells. Other shapes that have been utilized in energy absorption work includes W-frame made of four rods connected by three elbows, polygonal cross-section cylinders subjected to lateral and axial loads, wave-shape guard fence made of bent pipes, cubic rod cell, three-dimensional tubular system, inversion of spherical shells and axial crushing between rigid plates, single-hat and double-hat thin walled sections, and symmetric stepped circular thin-walled tube. These elements were used when filled with liquids, foams, wood shavings and sand. Energy dissipation by these EA systems is through plastic deformation of the metal by way of axial crushing, lateral indentation, lateral flattening, inversion, or splitting.

Hamidreza Z. and Mathias K. applied a multidesign optimization technique (MDO) technique to maximize the energy absorption and specific energy absorption of square, rectangular and circular tubes [19]. Results of MDO showed that the circular tubes have the best response. Further, the MDO technique was used to optimize honeycomb filled aluminium circular tubes. In order to find more strengthening effect, one dense honeycomb with strength of 0.896MPa was used. In comparison with optimum empty

circular tube, the optimum filled tube had less weight while it absorbed the same energy as that of the empty tube.

In a comparative study, Joel S. et al fully characterized the three commonly used energy management systems (expanded polypropylene foam, collapsing honeycomb and hydraulic shock absorbers) in 2.2 m/s pendulum bumper impact testing [17]. They sought to better understand the dynamic energy transfer and absorption of the system components and any synergies that exist between them. The test results showed that the energy absorbing systems which exhibited the best deflection performance when considered as individual components do not always work the most synergistically with the reinforcement beam. Simply examining the energy absorber's performance alone did not truly reflect the ability of the beam/absorber system's ability to manage energy. This observation advocates a system-oriented design concept, as opposed to independent optimization of the constituent components of the final product.

In light of the foregoing review, it is clear that the challenge to design and/or implement an effective and efficient impact energy management system is still alive. The weight of the issue is eminent from the inherent costs implications. Despite there being no express statistics connecting automotive bumpers repair costs and their design-related contribution to road fatalities in Africa, the picture painted by available fatality and crash damage levels is implicitly reflective of the consequential costs, as well as the dire need for sufficient preventive and/or protective measures, e.g. optimal bumpers design. According to an African road safety review report [20] published in December 2000 (and last updated on August 2, 2004), the road safety situation throughout the African

continent is one of the worst in the world. With approximately only 4 % of the world's motor vehicles, its road fatality share is 2 ½ times greater (10%). In several African countries, a motor vehicle is a hundred times more likely to be involved in a fatal crash than in the UK or USA. Estimated costs in six participant African countries (Zambia, Botswana, Kenya, Tanzania, Ethiopia and South Africa) show that, as a percentage of the Gross National Product (GNP), costs per annum range from about 0.8% in Ethiopia and 1% in South Africa to 2.3% in Zambia and 2.7% in Botswana to almost 5% in Kenya and the Kwa Zulu region of South Africa. Based on a cautious estimate, these suggest a regional cost of about $4.65 and $6.2 billion based on 1.5 to 2.0 % of GNP respectively.

As of 2005, the average recent model vehicle in USA incurred crash damage costs of at least $348 per year [21]. In 2003 the costs to repair these vehicles and the damage they caused would have totaled $16 –18 billion, based on an estimated 47 million vehicles. It was estimated that 81% of vehicle damage repair estimates were for front or rear impacts, and 65% of these entailed costs less than $2500. It was felt that bumpers could be expected to play a major role in preventing or limiting the damage. In many cases, vehicles involved in front-into-rear crashes sustain significant damage to safety equipment (lights) and cosmetic parts (hoods, fenders, grilles), with only minor damage to the bumper itself. Often, this results from under-ride, either because the bumpers fail to match up or because the bumpers do not remain engaged during the impact.

The general and specific shortcomings of past and existing bumpers, as reinforced by the express and implicit costs implications, do justify exploration of new design ideologies towards developing better impact energy management systems for automotive bumpers

application. Review of real-world crash damage has indicated three components of good bumper design that have been lacking on many passenger vehicles: compatible geometry, stability during impacts, and effective energy absorption [21]. Bumpers must be located and sized so they engage the bumper systems on the other vehicle with sufficient overlap to account for variations in ride height due to occupant and cargo loading and braking. Once engaged, bumper systems should offer a stable interface and remain engaged throughout the impact. Bumper stability can be influenced by bumper cover geometry, bumper reinforcement bar shape and strength, and energy absorber design. After the geometry and stability requirements have been met, bumpers must still have sufficient energy absorption capabilities to confine damage to the bumper system itself.

The core objective of this research work has been optimization of these performance factors, especially the impact energy management aspect. Further, integration of both absorptive and dissipative impact energy management dynamics are central to the design, while still up-holding the concept of geometrical recovery from after loading.

2.3. Granular mechanics – The design concept

An assessment of the suitability of granular medium for impact energy absorption and/or dissipation was conducted. J.S. Uehara et al [22] gave an overall view of granular mechanics by highlighting the two-fold behaviour of sand, i.e. fragility and high strength depending on the strain rate. At the scale of grain-grain interaction, they suggested that there are only a few possible forces – there can be normal forces perpendicular to the contact plane, there can be static and sliding friction parallel to the contact plane, and there can be inelastic collisions. In context of random granular packing, they noted that

normal forces are random too but can be correlated over long distances in so-called "force chains". Dissipation can be either through inelastic collisions or sliding friction.

Since meteorites generally strike at non-normal angles but nevertheless produce circular craters, it is believed that impacts can be likened to explosions [22]. Extensive data for buried explosives and high-speed ballistic impacts indicate that the crater diameter D_c often scales as a power of energy. For example, the exponent is 1/3 when the energy is dissipated by plastic flow of the medium throughout a volume equivalent to D_c^3; it is ¼ when the energy goes into lifting a volume D_c^3 by a distance D_c against a force of gravity. This "gravity limited" regime was observed in low-speed laboratory experiments by J. Amato and R. Williams [23]. There, steel balls of various diameters D_b were dropped into sand from various heights H; the resulting crater diameters scaled as $D_c \sim (D_b^3)^{1/4}$. For high-speed impacts in loose sand, however, ballistics data support $D_c \sim \rho_b^{1/3} D_b^{5/6} H^{1/6}$.

J.S. Uehara et al [22] focused on the crater depth formed by a projectile impact. They proposed that, if a ball of mass *m* were dropped from rest and formed a crater of depth *d*, then the average stopping force satisfies the equation,

$$F(d) = mgH. \qquad (1)$$

By noting that H is the total drop distance, equal to the sum of initial height above the medium plus the depth of the crater, this simple experiment gives a direct signature of the granular dissipation mechanics. They found that the depth *d* could be much less than the drop height H; therefore, the dissipation force can far exceed the ball weight. They confirmed the works of J. Amato and R Williams [23] that the crater diameter scales as

the ¼ power of the energy of the ball at impact: $D_c \sim (\rho_b D_b^3 H)^{1/4}$. Against expectations, a different scaling law was discovered for the crater depth: $d \sim (\rho_b^{3/2} D_b^2 H)^{1/3}$.

Other interesting findings were that, since the smaller nylon ball and the silicon rubber ball had nearly the same density and diameter, but had very different surface properties (nylon is slick and silicon rubber is tacky), friction between the ball and the grains could not be the dissipation mechanism for stopping the ball. Further, since the "live" and "dead" balls have nearly the same density and diameter, but have different restitution coefficients, no significant energy was transferred to internal degrees of freedom of the ball. Since identical cratering was found in 0.2mm and 1mm diameter glass beads, the grain size is not an important length scale. The depth scales as neither the ball energy nor the ball momentum at impact; i.e. *the diameter and depth are separate lengths set by separate physics* – the crater depth may be the more fundamental length scale, in that it naturally relates to the underlying granular mechanics. The average stopping force acting on the ball can be much greater than the ball, which the granular medium can barely support in a static situation. Friction at the ball surface, collisional granular hydrodynamics, and the plowing of hydrostatic grains, were all ruled out.

In their view, the instantaneous stopping force / impact dissipation may be explained by two possible scenarios: (1) As the ball crashes into the medium, it jams together the grains underneath. The normal force between these grains thus becomes much greater than the hydrostatic pressure. As the ball moves, the grain contacts slide so that each dissipates a total amount of energy given by the normal force times the grain size. New contacts are formed as the old force chains give rise to the dissipation force that

ultimately stops the ball. (2) Another possibility is that dissipation is due to sliding friction between force chains and the surrounding unloaded grains. They asserted that further work was needed to model either of these two effects.

NASA sponsored the Mechanics of Granular Materials (MGM) experiment for flights aboard the U.S Space Shuttle in pursuit of understanding how granular materials behave under low stresses [24]. The project's test cell constituted of cohesionless fine grains of sand (0.1 to 0.3mm diameter) with little variation in size. The specimen was contained in a latex sleeve that was 0.3mm thick and printed with a grid pattern so cameras could record changes in shape and position. In orbit, MGM successfully used the weightless environment of orbital flight to test soil under very low pressures. One of the main findings of the first flight of MGM, on STS-79 (Sept – 1996) was that the lower the confining pressure on the dense specimens, the higher the friction angle became, i.e. the specimens became stiffer. CT scans of the post-flight experimental test cell showed features unlike those seen in ground-based tests. Cross-sections had areas of generally uniform density outside of shear zones. Cross-sections at right angles to the axis of compression showed lower and higher density areas seeming to separate into radial streams, tied together toward the centre of the specimen, and at right angles to the outer surface. In vertical sections, a shear cone and shear plane were visible. MGM-II (on STS-89) results revealed a new phenomenon depicted by an overall volume change, in terms of expansion, and bifurcation instability in terms of relatively uniform bulging [25]. This led to extremely low density specimens, lower than achieved during MGM-I and as a result, a new upper-bound relative density at critical state was distinguished.

The density of granular media varies with the level of compaction, for instance, the density of loosely packed sand visibly increases when the content is shaken at low amplitudes [26]. However, if in addition the density goes beyond a definite threshold, the properties of the sand abruptly change and the granular structure cannot be sheared any longer without a volume increase. To describe this relaxation phenomenon in granular media, Mario Nicodemi et al [26] introduced a lattice model, in which frustration plays a crucial role. By computer simulations of a simple frustrated Ising lattice gas model, they showed that the density of their lattice gas was strongly dependent on the duration and amplitude of simply implemented vibrations. Their data reproduced the logarithmic relaxation behavior found in experiments in a sequence of taps, offering the possibility of also making new predictions for single taps. The data also reproduced the distribution of forces at the bottom of the system as found in real experiments.

In the current study, effort is made to shift from the traditional design platform of capitalizing on properties of material, to relying more on mechanics underlying the functional objective of bumpers. This has been achieved by a progressive process of harnessing the unique behavioral tendencies of granular media through a conceptual practical application. Unlike naturally available granular systems like sand and soil, a granular system is conceptually specified, constituting homogenous, geometrically spherical granules. This replaces the typical random geometric interlocking phenomena and inherent inter-granular friction implications, with one of discrete packing patterns displaying static and rotational sliding friction. Further, even though no moisture is contemplated, the entrapped air is considered to be at room temperature and pressure, with negligible effect on the envisaged granular mechanics.

CHAPTER 3:

PROPOSED ENERGY MANAGEMENT SYSTEM

3.1. General System Description

3.1.1. Introduction: General layout

The proposed impact energy management system proposed here-in consists of four main components, designed to be functionally interdependent; (a.) a skin, (b.) an elastomeric encapsulating membrane, (c.) geometrically spherical balls, and (d.) a base. Figure 3.1 below shows a sketch of longitudinal cross-sectional view of the assembly.

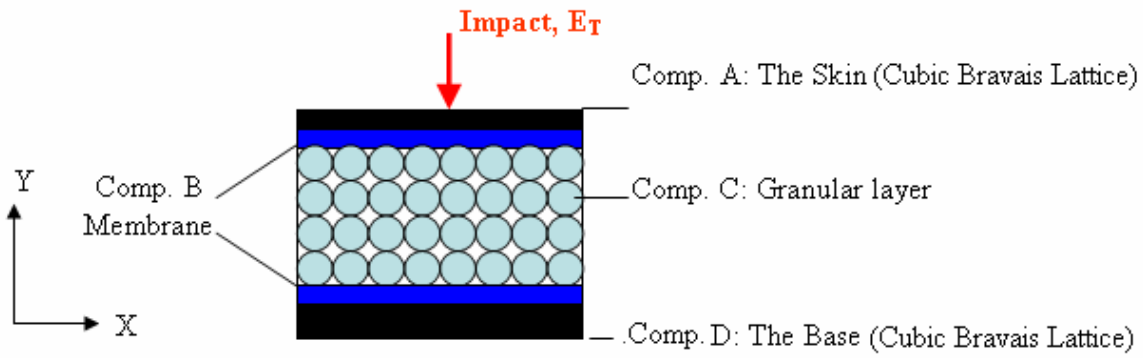

Figure 3.1: Sketch of longitudinal cross-sectional view of the system.

3.1.2. The Skin / Fascia

Component A is the skin, primarily designed for extensive elastic deformation capability and aesthetic purposes. It is designed in such a way that its ability to absorb impact energy does not compromise its ability to conform to the changing profile of the impacting object, and consequently the capsule. Hence it is designed to have good flexural yield strength, i.e. capable of taking very large localized deflections without failure by way of cracking, fracture, and permanent dents, in addition to recovery from physical deformation after the load is removed. Its thickness is just enough to maintain its

profile and alignment with the rest of the vehicle's body; before and after impact(s). It is designed to be able to withstand environmental degradation. To minimize the torsional effect of oblique loading on the entire system, e.g. due to over- and under-rides on automotive bumpers, this component is designed to exhibit differential local deformation, as opposed to being a rigid structure. This way, deformation at any point during impact may be visualized to be approximating the absolute geometrical dimensions of the impacting object's profile at bumper contact.

On the interior face, the skin is moulded with hemispheres (same diameter as that of the encapsulated spheres) so positioned to emulate dimensional geometry of a chosen cubic *Bravais* lattice structure; *Body-Centred-Cubic* (BCC), *Face-Centred-Cubic* (FCC) or *Simple-Cubic*. Their function is to default packing of the encapsulated spheres from their primarily random packing to the particular lattice arrangement. This will also contribute to stability of the entire system by stabilizing the impact interface.

3.1.3. Encapsulating elastic membrane

Component B is a very thin high-strength elastomeric membrane that can exhibit great stretch ratios. Its function is to encapsulate the spheres. It is designed in such a way that double its thickness must be less than the spacing between any two adjacent hemispheres. Since elastomeric materials are rather tacky, an appropriate lubricant on the inner lining is considered necessary in order to improve the systems responsiveness to impacts. Choice of lubricant is specified to be chemically compatible with the material from which the membrane is made. In general, membrane thickness, surface texture and behavioural properties are optimized in line with the entire system's performance specifications, rather than as a component in isolation.

3.1.4. Granular layer

The granular layer (Component C) constitutes loose, randomly packed homogenous spherical balls. As an effort to reduce weight, the spheres are designed to be hollow, or with a lighter core, e.g. polystyrene material. If r and R are the internal and external radii of a typical hollow sphere respectively, it is envisaged that there must be a ratio $\alpha = r/R$ for which the energy absorption and/or dissipation per unit weight of the sphere, is optimal. This value is determined experimentally or by way of simulation. As with the surface texture of the encapsulating membrane, the specification of balls' surface texture is dependent upon an optimization process in context of the entire system. The process is meant to help choose a between either coating them with a suitable lubricant or determining an optimal coefficient of friction. Choice of spheres size is also dependent upon an optimization process.

3.1.5. Base plate

The base (Component D) is similar in design to the skin, but with a slightly thicker wall to provide for fastening of the entire assembly to the main vehicle body. Its biasing hemispheres serve to produce a reflective impulse to the one incident on the skin upon impact, with possible damping effects. Further, the hemispheres serve to improve the grip between the impacting object and the bumper system assembly.

3.1.6. The Sandwich Concept

ASTM defines a structural sandwich as a special form of a laminated composite comprising of a combination of different materials that are bonded to each other so as to utilize the properties of each separate component to the structural advantage of the whole assembly [27]. It consists of three main parts; two thin, stiff, and strong faces separated

by a thick, light, and weaker core. The faces are adhesively bonded to the core to obtain a load transfer between the components. The faces act together to form an efficient stress couple or resisting moment counteracting external bending moment, while the core serves to resists shear and stabilize the fasces against buckling or wrinkling. Besides weight efficiencies among other advantages, one prime advantages of sandwich construction is that the absorption of mechanical energy can in some deformation modes be multiplied compared with monocoque structures due to an imposed shorter mode of buckling waves. Upon loading, the three constituent parts are subjected to different kinds of loading; the faces exhibit almost entirely membrane tension / compression and the core pure shear.

The proposed system is similar to a sandwich construction, with few definitive deviations: (1.) the faces are not bonded onto the core, (2.) the faces are designed to exhibit differential deformation behaviour, (3.) the core is a set of non-bonded granules designed to act like a 'fluid' with a pseudo-hydrostatic pressure as induced by the encapsulating membrane, (4.) a provisional free space between the faces is deemed necessary to accommodate anticipated deformation of the core during loading, and (5.) unlike it's counterpart, the system can barely carry quasi-static loads over wide spans; it's particularly designed for impact loading. Despite these deviations, it still passes the principle criteria of being considered a sandwich, with the commensurate advantages.

3.2. Contextual Application: The Automotive Bumpers

Figures 3.2 (i) and (ii) illustrate the proposed system's excerpt views in the context of an automotive bumper. Component-specific details relating to generalized application of the system are given. However, due to materials and facilities limitations, prototyping is

constrained to available resources as detailed in a later chapter but within reasonable deviations from the contemplated ideals.

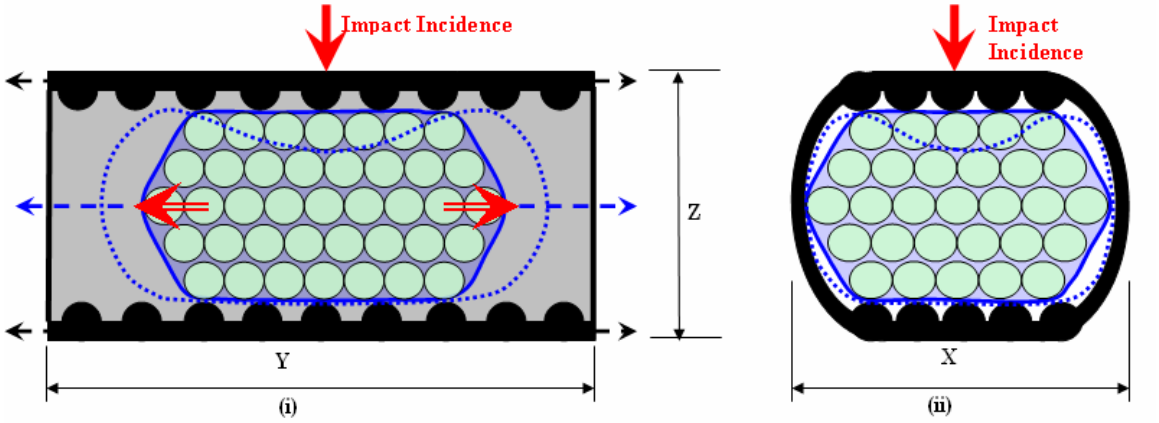

Figure 3.2: Longitudinal (i) and Lateral (ii) cross-sectional views.

3.2.1. The Casing (e.g. combination of fascia, base-wall, and side walls)

The casing illustrated in black color in Figure 3.2 (i) and (ii) is preferably injection-molded as one component. It may as well be moulded in two separate assembly parts. Further, the fascia (face plate) may grossly be webbed to ensure congruence with the exterior profile of neighbouring body panels. Critical material properties of the casing are flexural, impact and tensile strength. Other relevant properties include, but not limited to, heat resistance / conductivity, resistance to environmental degradation, and electrical properties. Just like the afore-mentioned properties, dimensions X, Y, and Z may contextually be specified to requirements.

Ideally, the moulded-with biasing hemispheres have a constant diameter Ø = d for any particular bumper. This diameter is set to be equal to the diameter of the encapsulated spheres (to be explained later). For improvement of shear strength between biasing hemispheres and the casing wall, the circular line of contact maybe filleted. Positioning of the hemispheres (entirely, partially, or a combination there-of) is in accordance with

chosen cubic *bravais* lattice structure(s), viz, Simple-cubic structure, *and*/*or* Face-Centered-Cubic (FCC) structure, *and/or* Body-Centered-Cubic (BCC) structure. Random arrangement of hemispheres, other currently known lattice structures, or plain facing of interior wall may also be considered. Arrangement of hemispheres on fascia's interior side may or may not be a mirror representation of hemispheres on the interior side of base-wall.

The contemplated incident impact is normal, or oblique to the casing surface. Allowable magnitude of the impact depends on the bumper's contextual specifications and/or design requirements.

The wall thickness, t, is required to be even throughout or varying according to desired system optimization. Of prime importance is that the fascia should be able to undergo and withstand large deformations elastically, yet retain its profile before and after crash(es).

3.2.2. Encapsulating Elastic Membrane

The membrane is illustrated in blue colour in Figure3.2 (i) and (ii). The dotted blue line indicates the expected deformation profile during impact. It may be blow-molded as one component to specification, or simply designed from a flat sheet cut to requirements and assembled using an appropriate adhesive. Important material properties include, but not limited to, elongation to rapture, tensile strength, compression set, and allowable working temperature. Just like the aforementioned properties, the importance of other properties such as resistance to chemicals and staining depends of the contextual design environment.

The thickness should as much as possible be uniform throughout its profile. Choice of the

optimal thickness depends on the size of spheres to be so encapsulated, design impact energy, as well as the chosen lattice structure. Dimensions of the membrane capsule are dependent on the required design specifications. However, the entire capsule need be designed to fit inside the casing even under maximum allowable deformation conditions.

An appropriate lubrication of the membrane's interior surface may be considered in the process of optimizing the system's efficiency and/or durability. However, this optimization process constitutes tentative future work. The casing and the capsule are not bonded by any means other than for maintaining capsule inside the casing as may be considered necessary.

3.2.3. Encapsulated Spheres

They are illustrated in olive color in Figures 3.2 (i) and (ii), and otherwise referred to as the granules. Ideally, they are designed to have a common diameter Ø = d, equivalent to the diameter of biasing hemispheres. Target material's properties include, but not limited to, light weight, impact and compression strength, resilience, coefficients of restitution and friction, energy absorption, and hardness. Likewise, other choices of properties like heat and electrical resistance/conductivity vary with design specifications and / or contextual working environment of the particular automotive bumper.

The encapsulated spheres must have a non-sticking surface and are all not bonded to each other, i.e. the only thing keeping them together is the bounding encapsulation elastic membrane. The default granular packing within the capsule is random. Packing density may vary according to desired design outcomes. Ideally, any pre-stretch should be evenly distributed throughout the encapsulation, and voids should be minimal, if any.

As a weight reduction strategy, the spheres may be hollow with an optimally determined wall thickness. Alternatively they may comprise a lighter inner-core material. An appropriate lubrication of the spheres surface, if found necessary, may be considered in the process of optimizing the system's recovery, efficiency, and/or durability.

3.3. Stress – Strain Relationship: Comparative Analysis

It is anticipated that an insight into stress – strain curves of the current and potential impact energy management materials / media constitutes a reasonable ground for comparative appraisal. Accordingly, expanded polypropylene (EPP) foam has representatively been chosen alongside another up-market foam product, Duocel® foam for comparison against granular media.

3.3.1. Expanded Polypropylene (EPP) foam

Expanded polypropylene (EPP) is an already well established material in the automotive market [28]. In bumper cores, side impact panels, head and knee cushions and other

Figure 3.3: Polypropylene monomaterial composite with TPO skin [28]

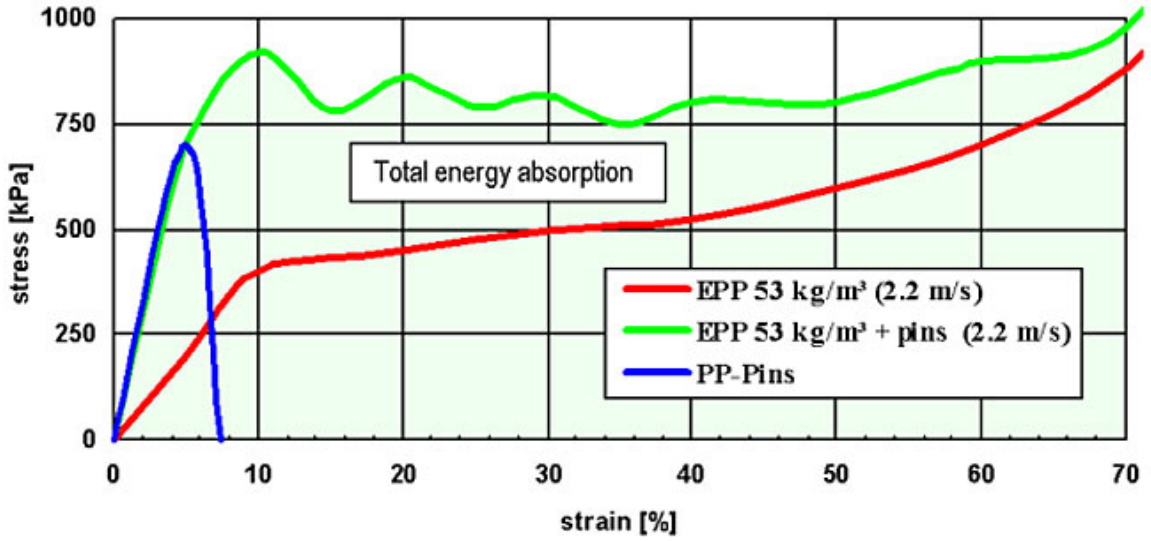

Figure 3.4: Stress-strain curves for EPP, one single pin and FAWOPIN [28]

automotive components, it combines a very good energy absorbing capability with the requirements of recyclability, temperature and chemical resistance, as well as excellent structural stability. Over the last five years, important developments have dramatically improved its performance, materializing to so called monomaterial TPO skin / PP foam composites, as illustrated in Figure 3.3. Alongside relative curves, Figure 3.4 shows the improved stress–strain curve of sample FAWO®-series of products.

A new tool surface technology and the back foaming process (skin moulding) have improved surface properties and the new composite structures have increased energy absorption. Worth mentioning is the tremendous improvement in energy absorption in the EPP field by a patented composite of EPP and injection moulded PP pins [28]. Due to fast increasing uniaxial pressure at the beginning of the pin deformation, this composite enables the excellent energy absorption of the EPP to be optimized from the beginning of deformation along with a large amount of compression.

Despite the aforementioned technological advancements, notice however the composite's tendency towards compaction as the strain exceeds the 70% mark. Beyond this strain regime, the extra impact energy will simply be transferred across the cross-section to the shielded component, object, or surface. Another setback is that the optimal performance for this kind of composite is unidirectionally oriented. Any attempts to make it suitable for multidirectional loading, as in oblique vehicle impacts, would either be impossible or uneconomical.

3.3.2. Duocel® Foam

As an effort to counteract the phenomenal limitations of foams and other porous structures as elucidated in chapter 2, Duocel® foams have been developed by ERG, a Materials and Aerospace Corporation [29]. Figure 3.5 shows the cellular structure of typical Duocel® foam.

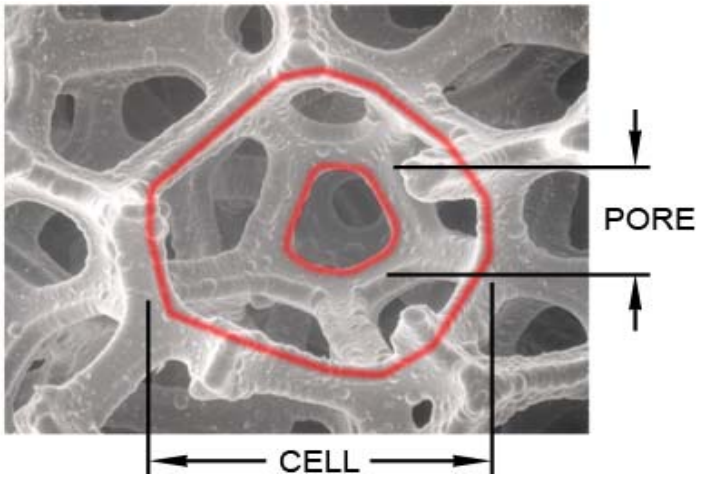

Figure 3.5: Duocel® foam cellular structure [29].

A typical stress – strain plot is as shown below in Figure 3.6, indicating the Elastic, Transition, Plastic, and Densification Zones. These foams have a couple of advantages over conventional foams and honeycomb structures: (1.) Being made of metals, carbon,

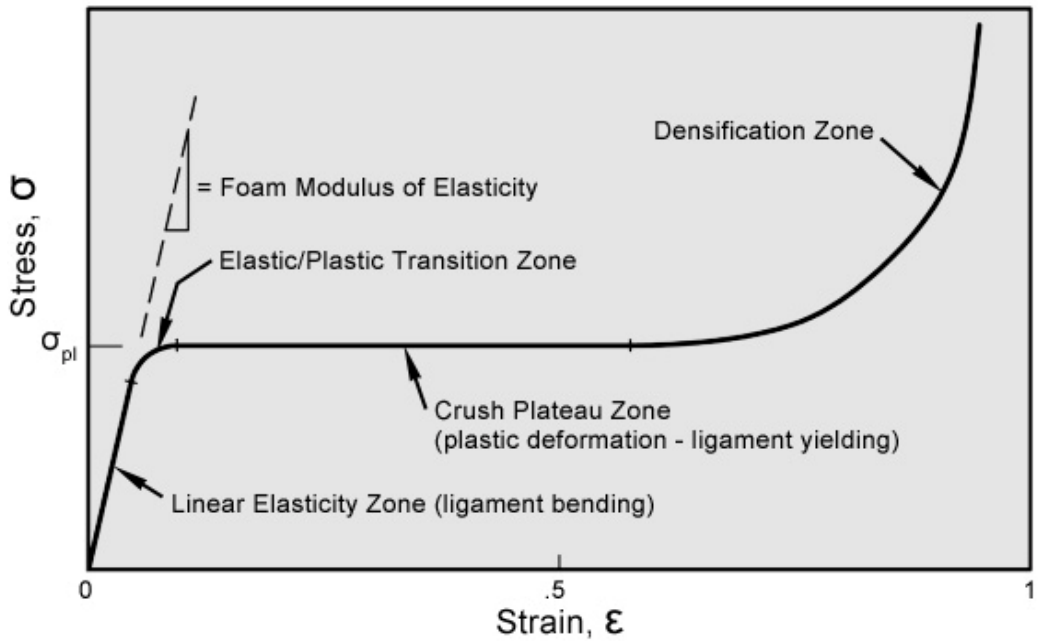

Figure 3.6: Typical stress – strain plot for Duocel® foam [29].

and ceramics, these foams are comparatively insensitive to environmental factors, and thus they can reliably provide predictable energy absorption performance after even years of storage or exposure in extreme military standard environmental conditions, (2.) Unlike honeycombs which are considered one-directional, or "orthotropic" foams, Duocel has the same structure in all three dimensions and is defined as an "isotropic" foam. Accordingly, it has the same stress / strain curve regardless of impact direction, and (3) Duocel foams are open-celled, so they do not hermetically trap gasses that can create a pneumatic "spring" effect at low impact velocities or create rebound. At very high velocities, there is a fluid flow friction effect as the entrained gas is rapidly squeezed out of the open-celled foam structure. In this case there is still no effective spring-back, but the increased initial resistance can provide a convenient "crush plateau enhancement" if the impact is at a much higher velocity than anticipated. This feature can, however, be

controlled by selection of the foam pore size and airflow resistance.

Depending upon the initial relative density of the foam, Duocel exhibits a constant collapse to approximately 50-70% of strain after the typical elastic / plastic transition zone [29]. After this maximum strain regime, it enters into a densification zone with only a marginal room for energy absorption.

It should hereby be noted that the stress – strain plots for EPP and the Duocel® foam are independent of the strain rate. Further, unlike surface area and fluid flow pressure drop which are strictly properties of the foam structure, most foam properties are at least partially affected by (composition and properties of) the base material(s). Their inherent impact energy absorption is characterized by a limitation to the 70% strain, and/or irreversible destruction of the underlying cellular structure.

3.3.3. Granular Media

Unlike the EPP and Duocel® foam as evaluated above, granular media exhibits a number of structural and functional diversities: (1.) the stress – strain response is dependent upon the strain rate; sand can be very fragile and yet demonstrate very high strength depending on the strain rate [22], i.e. shear thinning effect, (2.) granular particles are characterized by a loss of energy whenever the particles interact during global deformation [30] (3.) unlike foams, which are functionally subject to creep, granular materials can support (small) shear stresses indefinitely [30], (4.) the mode of failure depends on the medium's confining pressure; in dense confined packing, failure is often characterized by shear banding whereas fluid shear flow characterizes failure in less constrained granular media, (5.) the maximum shear stress that a medium can carry is dependent upon the shape of

the constituent granules; pentagonal particles have been shown to exhibit higher force anisotropy that leads to enhanced shear strength as compared to circular disks of similar polydispersity [31], (6.) The stress response of a granular media is highly dependent upon the boundary conditions; a tiny change of the boundary conditions may lead to a strong variation in the incremental stress relation and in other cases, these changes may generate large variations of the stress field [32], and (7.) granular media are considered to be dissipative, out-of-equilibrium systems in which stress propagation is highly inhomogeneous and anisotropic [33]; in the solid regime, a granular media system self-organizes in structures, or chains, supporting the stress with an asymmetric distribution about the mean value. By increasing the driving velocity (shear strain rate), however, instantaneous fluidization becomes more and more frequent until the fluid regime is reached, in which the dynamics is collisional and stress distribution is symmetric. It has been averred that, peaks in the rigidity and stress distribution's skewness indicate that a change to the force-bearing mechanisms occurs at the transition to fluid behaviour [33].

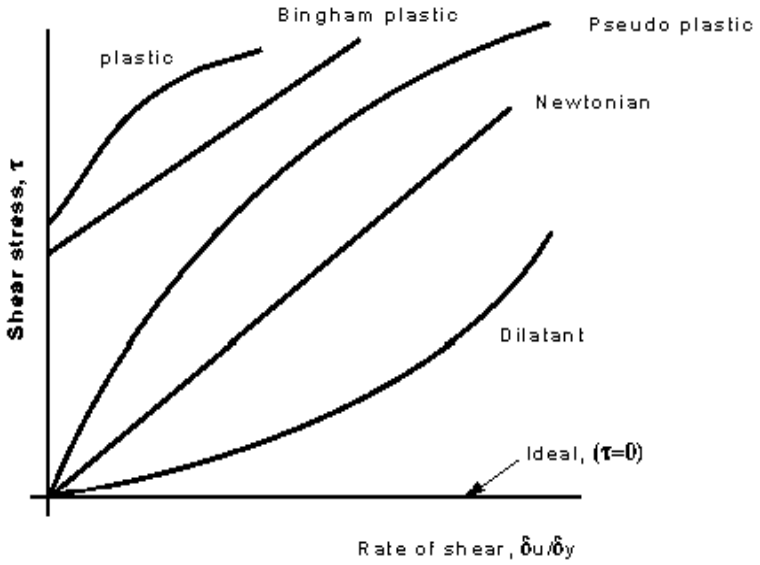

Figure 3.7: Rheogram of Newtonian and non-Newtonian fluids [34]

With the kind of behavioural diversity as already highlighted, one particular stress – strain curve may be misleading, or otherwise representatively inadequate. However, in the context of the proposed system, the deformation zone in characterized by shear flow that is synonymous to a pseudo-plastic non-Newtonian fluid. Figure 3.7 shows a rheogram of pseudo-plastic fluids, with comparative plots for other fluid clusters.

Bearing in mind that the proposed system's core constitutes *granular media encapsulated in an elastic membrane*, afew advantages over foams and honeycombs, even with the latest technology as discussed above, are already apparent: (1.) experimental results contained here-in indicate that the effectiveness of the core is rather highly reliant upon the underlying dissipative granular mechanics, as opposed to the crush strength of the base granular material (glass), (2.) depending on the core's thickness and boundary conditions, granular media can exhibit extensive shear flow without densification, especially due to the spherical nature of individual granules – no inter-locking phenomenon, (3.) the amount of strain that the core can accommodate is dependent upon the encapsulating membrane, rather than the base material for granules so encapsulated – and this can be to the tune of approximately 400 - 850%, (4.) in addition to granular media's stress response being time-dependent, the advantageous visco-elastic effect can further be harnessed through material engineering and/or selection for the encapsulating membrane. (5.) Since the core is multiaxially highly deformable, the direction of impact incidence is not a critical parameter. These advantages depict the great potential incumbent to development of the proposed system to its optimal capacity. This contention has been proven through experimental and theoretical analysis in the chapters following henceforth.

CHAPTER 4:

EXPERIMENTAL DESIGN VALIDATION

4.1. Introduction

It is expected that the type of biasing base plate will influence the deformation characteristics of the system. Therefore an experimental setup to investigate this relationship was executed under *quasi-static* and *dynamic* load conditions. The objective of quasi-static loading was to investigate the system's sensitivity to design parameters such as the type of biasing base plate, type of impact head and bulk density of the core. Comparative analysis was based on the transverse and longitudinal deformation measurements of the capsule. Another critical factor that was investigated was the system's stability upon impact.

Dynamic load testing was done to investigate the system's sensitivity to: (i) the strain rate, (ii) type of biasing plates, (iii) impactor-head profile selection, (iv) relative density of the granular medium, i.e. capsule's bulk density, (v) intergranular contact friction, i.e. effect of lubricating the system.

There is no available standard for the testing. The entire experimental setup was done in close alignment to ISO 6603-2 [35], with few necessary modifications to the apparatus, procedures, and data acquisition as outlined later. This standard is primarily designed for multi-axial instrumented impact testing. A hemispherical striker with either a 10mm or 20mm diameter is used, being dropped or forced mechanically such that its velocity is 4.4 m/s on impact. The standard states that the specimen may be left unclamped. However, it is noted that the test results obtained from clamped and unclamped specimens may be

different due to the freedom of movement of that the specimen has away from the impact point. A detailed sketch of the specimen used and its actual set-up is provided.

4.2. Samples Preparation

Spherical glass beads, 16 ± 0.20mm in diameter were encapsulated in 1mm thick rubber casings. The casing as assembled using *contact adhesive glue* as shown in Figure 4.1. Its material was cut out from an inflatable tube meant for an automotive tyre. A 15mm x 15mm cross sign was slit at the middle section of the capsule for insertion of the beads and thereafter sealed off with a 100mm diameter piece of same material, the latter serving as the tentative impact incidence interface as well.

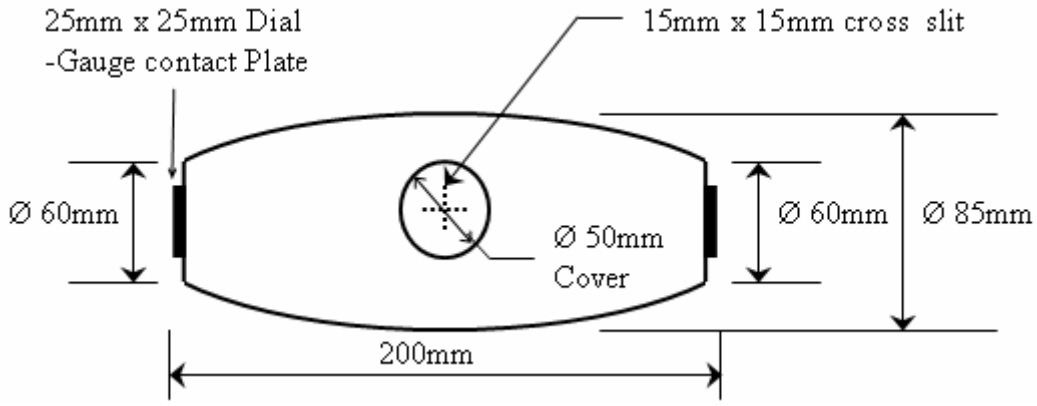

Figure 4.1: Spheres encapsulating rubber casing.

Two 25mm x 25mm smooth composite material plates, 2mm in thickness, were glued on either of the longitudinal ends of the capsule to even out dial gauges readings over these faces. Two categories of capsule sizes were used – Size (A): Ø60mm – Ø85mm – 200mm length, and Size (B): Ø60mm – Ø110mm – 300mm length. For Size A, the bulk density was switched between 250 and 290 glass beads, while that of Size B was switched between 465 and 500 beads.

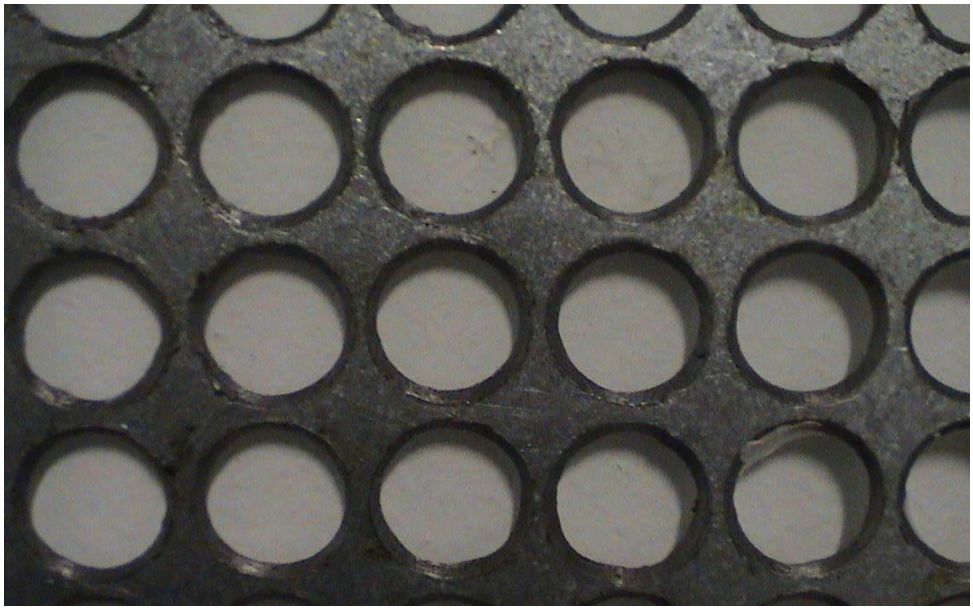

Figure 4.2: Section of sample drilled galvanized lattice template.

Figure 4.3: Pictorial view of mould set-up.

Ø14mm holes were drilled on pieces of 1mm thick, galvanized mild steel sheets as shown in Figure 4.2 in order to mould cubic *Bravais* lattice structure boundary plates. Figure 4.3 shows a pictorial view the female mould set-up. It was made by clamping the respective

holes-templates with a wooden frame, exposing a perforated area measuring 185mm x 300mm.The exposed area of the template and the enclosing wooden frame walls were coated with a thin layer of petroleum jelly to act as a release agent. This was after leveling the entire assembly with aid of threaded screw rods, bolts for height adjustment and a spirit level. Glass beads also coated with petroleum jelly were arranged to cover holes in the exposed area, with incompletely exposed holes being sealed off using a rubber tape.

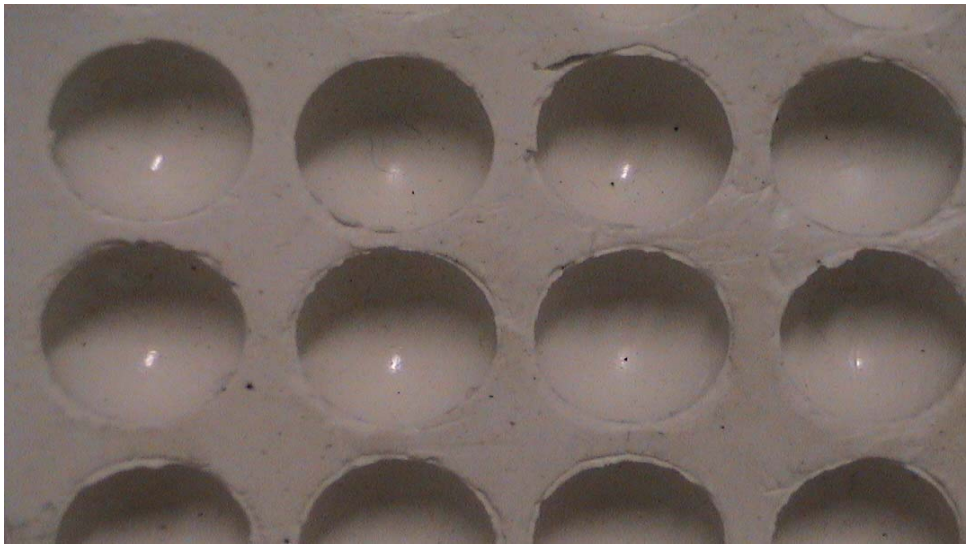

Figure 4.4: Section of sample female silicon mould.

700g of *ELASTOSIL® M4514* liquid silicon was blended with 5%wt Catalyst T26 (silicon hardener) supplied by *Amt South Africa*. The mixture was then slowly poured onto one middle point of the exposed area, allowed to cure for 4 – 6 hours and then unclamped to take out the glass beads. This process left a mould with 160, 198 and 208 almost hemispherical hole-impressions on the mould for BCC, Simple-Cubic and FCC holes-template respectively. The mould was left to cure in ambient conditions over at least 24 hours. Figure 4.4 shows a section of sample female silicon mould displaying

hemispherical holes. For biasing a random arrangement, a smooth flat plate of similar utmost dimensions was used.

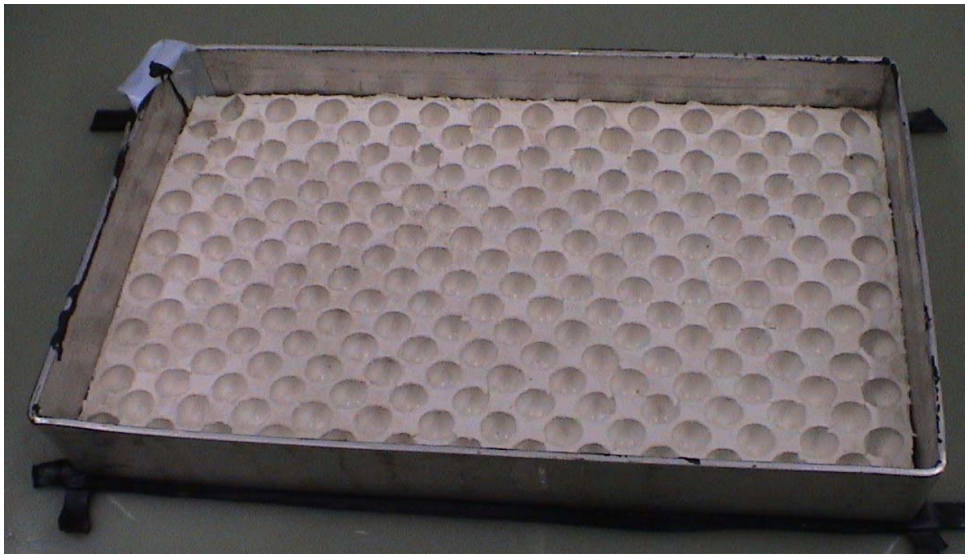

Figure 4.5: Mould for sample cubic *Bravais* lattice plate.

In order to mould the intended (male) cubic lattice plate, a 185mm x 300mm open rectangular tray was made to hold the respective female silicon mould with holes facing up as shown in Figure 4.5. Its interior walls were coated with a thin layer of petroleum jelly. 800g of epoxy resin (LR-20) was carefully blended with 30%wt epoxy hardener (LH-28), poured onto the silicon mould after laying on 4 layers of S-glass fibre mats, all procured from *Amt South Africa*. Setting period of 12 hours was allowed before separating the male composite mould from the silicon mould, leaving it to cure at room temperature for 24 hours. Sample section-views of the *Simple cubic*, *FCC* and *BCC* lattice-biasing plates are shown below in Figure 4.6 (i), (ii) and (iii) respectively. Similar but thinner walled, deflectable BCC and flat "*Face / Skin plates*" measuring 180mm x 180mm were moulded using vacuum assisted resin infusion moulding (VARIM) technique with two layers of the fibre reinforcement mat.

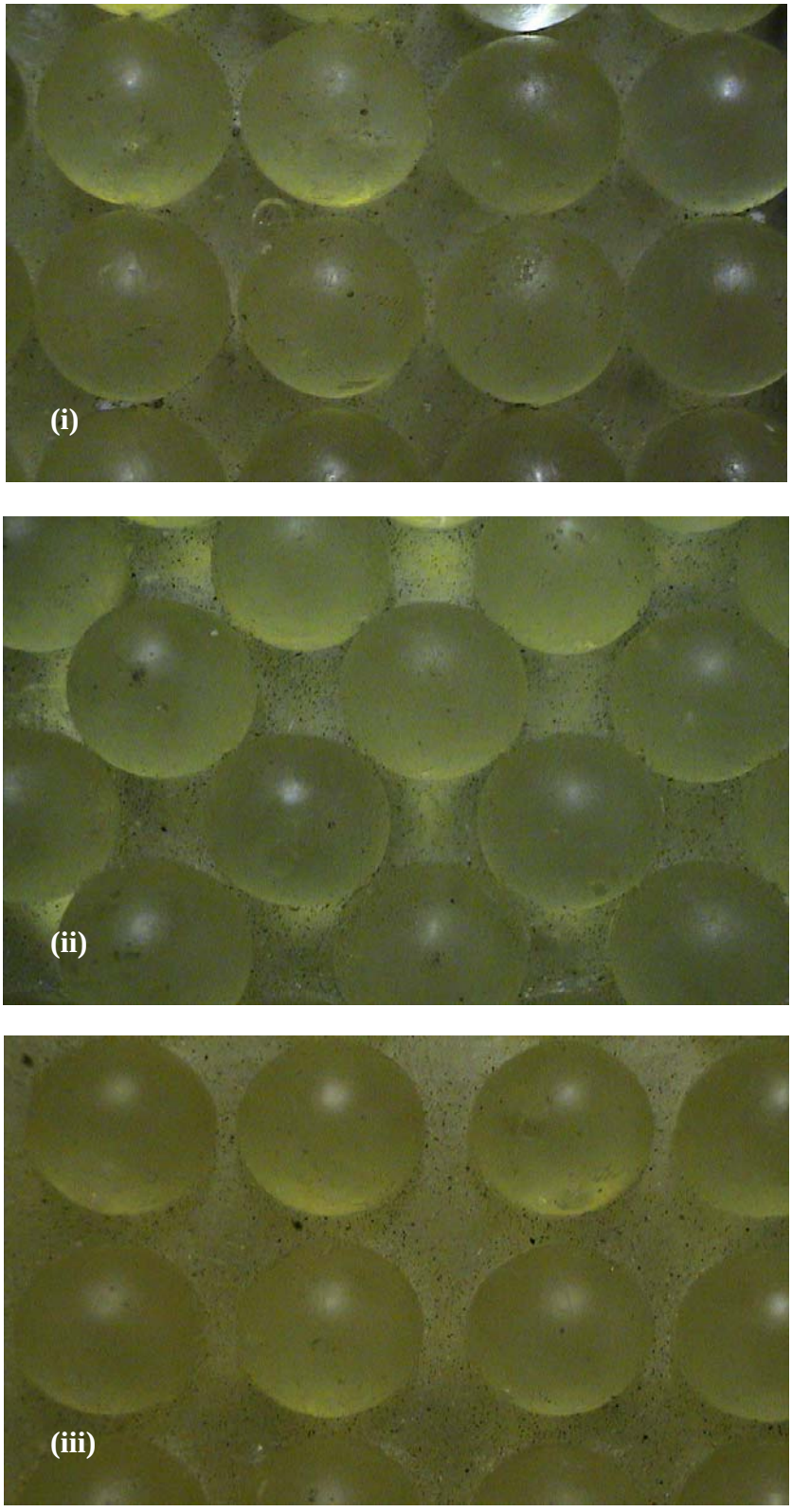

Figure 4.6: Sample section-views for Simple cubic (i), FCC (ii), and BCC (iii) lattice-biasing plates.

4.3. Apparatus Preparation

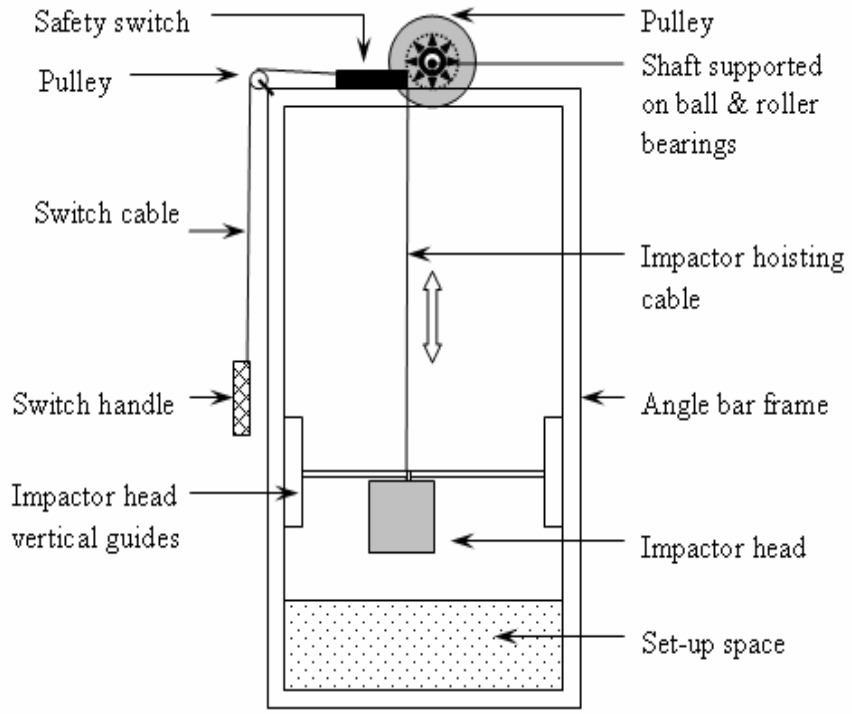

Figure 4.7: Side view of drop-weight testing machine.

Figure 4.7 illustrates general outlay of the drop-weight testing machine used for testing. The machine was designed with a capacity to deliver a maximum impact velocity of 25m/s. It was equipped with a pulley and release switch for manual hoisting and release of the impact load. A test velocity of 2.43 m/s was used, with dial gauges being used for data acquisition. In view of the test parameters, the adverse effects of friction between impactor and specimen as contemplated in the ISO 6603-2 standard were considered negligible and hence ignored. Moving parts of the machine were sufficiently lubricated.

The machine carried a cylindrical mild steel impactor head weighing 50 kg. Two 45mm M12 threaded rods were appropriately welded onto the impactor for fastening in order to obtain *rounded* and *angled* impactor heads by using its cylindrical and tapered surfaces,

respectively. It had a diameter of 180mm and one conical end with an included angle of 145^0. Figure 4.8 shows the impactor as fastened for *rounded* impactor head.

Figure 4.8: The impactor head.

4.4. Experimental Procedure

Some deviations from the ISO 6603-2 standard were in respect of the specimen's specifications and means of data acquisition. Since the test was not aimed at assessing properties of the material(s), but rather the entire system's deformation behaviour, the specimen constituted a representative cross-section of a typical full-scale system. Dimensions of interest were the transverse and longitudinal measures of deformation. Lateral deformation was ignored in view that deformation along one of the axis may contextually be restricted as in the case of automotive bumpers.

Three different and more relevant impactor head types were used; (1) angled impactor head, simulating collision with sharp objects, (2) rounded head simulating collision onto

a pole, and (3) flat head simulating a head-on collision. Flat impactor head was facilitated by putting a flat rigid plate between the capsule and impactor head.

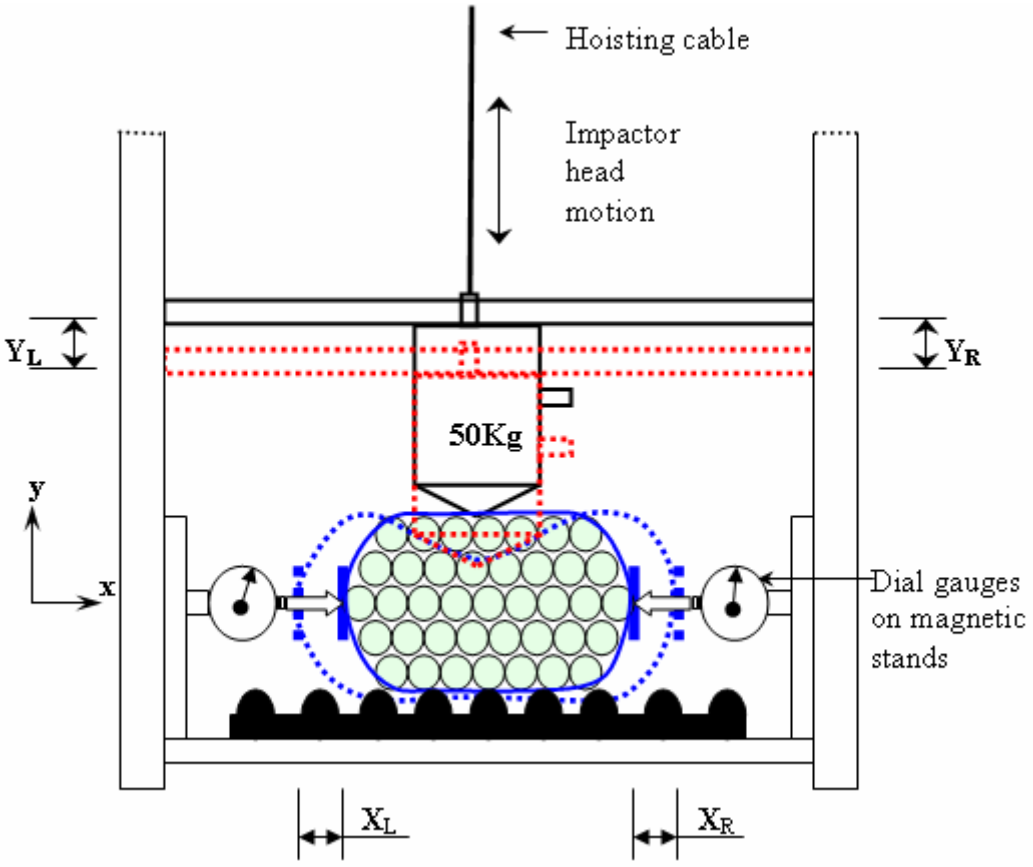

Figure 4.9: Experimental loading set-up.

Four different biasing base plates (BCC, FCC, Simple Cubic and Random) were used, simulating different virtual structural reinforcement within the capsule. The *biasing base plate – capsule – impactor head* set-up is shown in Figure 4.9. The dotted lines show positions after loading.

For quasi-static loading, capsules were laid onto a biasing *Bravais* lattice structure base plate as illustrated in Figure 3. Caution was taken in ensuring that the impactor head was just touching the top surface of the capsule before releasing the load by means of the

manual release switch. Capsule Size (A) was used, with varying bulk densities at different test runs.

Dynamic loading test was performed using a similar set-up but this time the impactor head was hoisted to 300mm above the capsule. Capsule Size (B) was used. Additional tests were run to find: (1) effect of lubricating capsule's interior walls and encapsulated beads. (2) effect of using deflectable identical face plates for *BCC* and *Random* packing plates as in the proposed bumper system.

Longitudinal deformations, X_L and X_R, were measured using dial gauge indicators while the vertical deformations, Y_L and Y_R were measured by means of vernier callipers. Ten readings of were taken for every combination setting of *base plate - bulk density - quasi-static/dynamic loading height–capsule size–natural/lubricated beads and capsule – impactor head type*. Average represent tative longitudinal ($X_{Average}$) and vertical ($Y_{Average}$) deformation values were respectively computed using Equations (2) and (3).

$$X_{Average} = \frac{1}{10}\sum_{i=1}^{n=10}\frac{1}{2}\left[X_{Li} + X_{Ri}\right] \quad (2)$$

$$Y_{Average} = \frac{1}{10}\sum_{i=1}^{n=10}\frac{1}{2}\left[Y_{Li} + Y_{Ri}\right] \quad (3)$$

Comparative deformation quotient was computed for any combination using Equation (4). This quotient was used as the basis of ranking deformation behavioural performance according to pre-determined criterion.

$$Quotient = \frac{Y_{Average}}{X_{Average}} \quad (4)$$

4.5. Results and Discussions

It is clear that the ideal system would be one that gives the best impact energy management. In terms of measurable deformation parameters, $X_{Average}$ and $Y_{Average}$, this system would minimize $Y_{Average}$ and maximize $X_{Average}$. This way, attenuation of impact energy (by re-direction of the impact force vector), would be maximized. As such, this assessment criterion favours the system offering lowest deformation quotient, tending towards 0.5 as in the human system.

	PARTICULARS	**BCC**	**FCC**	**Simple Cubic**	**Random**
	Number of Hemispheres	**160**	**208**	**198**	**N/A**
1	**Angled Head @ 250 Balls**				
	X-AXIS ($X_{Average}$)	5.12	4.09	4.26	5.63
	Y-AXIS ($Y_{Average}$)	45.02	45.28	47.67	43.73
	QUOTIENT	**8.79**	**11.07**	**11.19**	**7.77**
	Ranking	**2**	**3**	**4**	**1**
2	**Rounded Head @ 250 Balls**				
	X-AXIS ($X_{Average}$)	6.39	5.81	5.36	7.84
	Y-AXIS ($Y_{Average}$)	47.13	48.09	49.97	46.88
	QUOTIENT	**7.38**	**8.28**	**9.32**	**5.98**
	Ranking	**2**	**3**	**4**	**1**
3	**Rounded Head @ 290 Balls**				
	X-AXIS ($X_{Average}$)	5.43	5.36	4.73	5.70
	Y-AXIS ($Y_{Average}$)	53.30	54.52	56.70	51.34
	QUOTIENT	**9.82**	**10.17**	**11.99**	**9.01**
	Ranking	**2**	**3**	**4**	**1**

4	**Flat Head @ 290 Balls**				
	X-AXIS ($X_{Average}$)	4.46	5.05	5.86	4.73
	Y-AXIS ($Y_{Average}$)	28.28	29.29	31.53	26.26
	QUOTIENT	**6.34**	**5.80**	**5.38**	**5.55**
	Ranking	**4**	**3**	**2**	**1**

Table 4.1: Consolidated comparative results for quasi-static loading.

However, for impact engineering purposes, additional factor(s) may constitute a major or even critical assessment criterion, for instance, the system's stability during and immediately after impact. Other factors may include the extent of system's ability to regain dimensional and functional form after impact, possibility of multiple impact loading cycles, stress / shock wave propagation and so on.

Quasi-static loading results are as shown in *Table 1*. With reference to the deformation quotients, it is evident that the biasing plate's effectiveness ranking is the same for both angled and rounded impactor head types, viz; random packing gave the lowest deformation quotient, followed by BCC, FCC and Simple Cubic lattice structure plates respectively. However, for flat head, random plate maintained its ranking while ranking for the other three plates was completely reversed. Generally, the relative magnitude of deformation quotient was greatest when a rounded impactor head was used, followed by angled and flat head impactor heads respectively.

For the rounded impactor head, increasing the capsule's bulk density by 16% increased the deformation quotients by 51%, 33%, 29% and 23% for Random, BCC, Simple Cubic, and FCC plates respectively. For bulk density of 290 beads, corresponding respective

sensitivities to variation of impactor head type from flat to rounded head were 62%, 55%, 123% and 75% respectively. Based on arithmetic average of these sensitivity levels, BCC showed the least vulnerability to the two investigated design parameters, followed by FCC, Simple Cubic and Random biasing plates. This observation is reinforced by the repetitive instability of dial gauge indicator readings after impact as witnessed especially with the Random plate, and occasional instances with FCC and Simple Cubic plates.

The general disparity in magnitude of longitudinal deformation as compared to vertical deformation may be attributed to four factors. (1.) tapered design of the capsule in longitudinal axis offers more control over the global hydrostatic flow of the discrete incompressible fluid of spheres, than otherwise would be if the capsule were to have a uniform cylindrical cross-section. (2.) The longitudinal distance between the reference surfaces is much longer than the vertical distance (trunk diameter of the capsule), viz, 200mm versus ø85mm and 300mm versus ø110mm for *Size (A)* and *Size (B)* capsules respectively. (3.) The loading axis is vertical and the longitudinal axis deformation was primarily responsorial. These factors are, however, subject to the more determinant granular mechanics. (4.) Since cratering in granular mechanics is primarily radial, displacement of this geometric incompressible fluid dampens along the longer longitudinal axis relative to the shorter vertical axis. (5.) It is suggested that virtual structures conforming to the respective biased lattice structure does resist the transverse deformation at the zone on impact incidence. (6.) It is possible that granular shear thinning phenomenon comes in to play at the interface of impactor/face plate and capsule.

	PARTICULARS	BCC Lubricated	BCC Dry	FCC	Simple Cubic	Random
1	**Rounded head @ 465 Balls – Base plate only**					
	X-AXIS ($X_{Average}$)	8.32	5.19	6.48	6.27	7.36
	Y-AXIS ($Y_{Average}$)	61.89	52.58	55.73	57.46	60.96
	QUOTIENT	**7.44**	**10.13**	**8.60**	**9.16**	**8.28**
	Ranking		***Last***	**2**	**3**	***First***
2	**Rounded head @ 465 Balls – Base plate & identical Face plate**					
	X-AXIS ($X_{Average}$)		11.25			10.56
	Y-AXIS ($Y_{Average}$)		41.65			45.21
	QUOTIENT		**3.70**			**4.28**
	Ranking		***First***			***Last***

Table 4.2: Consolidated comparative results for dynamic loading.

Dynamic loading results are shown in *Table 4.2*. They show a radical change in the system's behaviour as compared to quasi-static loading trends. Based on the quotient criterion, random plate maintained its ranking despite its higher level of instability relative to quasi-static loading scenario. Unlike quasi-static loading where its *first* rank is based on having the minimum vertical deformation and maximum longitudinal deformation, it maintained the same rank as in dynamic loading by recording maximum values for both deformations. Coupled with the high instability immediately after loading, these maxima (especially in vertical deformation) may be interpreted as poor control of the dynamic load. Comparatively, BCC recorded both the minimum vertical and longitudinal deformations, giving the *last* quotient ranking. It displays a strong sense of control on the granular mechanics within the capsule as indicated by its consistent

stability under both quasi-static and dynamic loading scenarios. FCC and Simple Cubic plates may also be considered to offer better control of dynamic load because they recording both lower vertical and longitudinal deformations than the random plate. Generally, their overall ranking remained the same regardless of loading method, despite their instability being slightly more under dynamic loading.

Lubrication of encapsulated beads and interior walls of the capsule improved BCC plate performance by about 25%. However, a slit measuring approximately 15mm occurred on the transverse side of capsule after seventh impact run. The single dispelled bead was replaced and this point used as the impact incidence point for the remaining three runs. This rapture may be attributed to the chemical effect of the carbon-based petroleum jelly on the capsule's rubber material, which is carbon-based as well.

Use of an identical but flexible face/skin plate between capsule and impactor head generally improved (lowered) the quotients for the tested BCC and *Random* packing plates by 63.46% and 48.31% respectively. The sharp reversal of quotient ranking between the two is worth noting. BCC recorded both lowest vertical and highest longitudinal deformations. This represented more than double the longitudinal deformation (116.76%), and a significant reduction in vertical deformation (20.79%). Corresponding values for *Random* plate were 43.48% and 25.84%. The new ranking confirmed that BCC plates offered better control of dynamic load than Random packing plates. The increase in longitudinal deformation as compared to vertical deformation points to spontaneous formation of virtual structural reinforcement near plates surfaces by biasing the packing of encapsulated spheres during impact.

Effectiveness of current bumpers and similar systems lay in the traditional aspect of harnessing properties of materials from which their constituent components are made. No glass beads are found to be broken. Since glass generally has low impact strength, effectiveness of the system lays in granular mechanics and influence of their packing pattern. This represents a successful attempt in shifting from the traditional design platform by concentrating on the energy dissipation dynamics of the system's components.

4.6. Conclusions

By manipulating boundary conditions using appropriate lattice structure plates, encapsulated geometrical granular media can be used to effectively manage impact energy. Of the cubic *Bravais* lattice structures, BCC proved to work better with the proposed energy management system than random packing, which characterizes naturally existing granular media. System's lubrication with an appropriate lubricant improves its functional performance and recovery of geometry. By optimization of design parameters, the deformation quotient may be driven towards 0.5. Future works may entail, among others, investigation of effect of *capsule's wall thickness, sphere sizes, granules' geometry*, as well as *their respective intrinsic mechanical properties* on the impact energy absorption and/or dissipation trends, ideally through discrete element modeling (DEM). Energy scaling for optimized system may then be conducted.

CHAPTER 5:

IMPULSE WAVE PROPAGATION MODEL

5.1. Introduction

It is expected that during impact, encapsulated granular medium as used in the proposed system continuously undergoes a number of structural phases. This view is supported by the comparative preference of BCC biasing plates in favour of the other two cubic lattice plates. Further, this agrees well with the theoretical understanding of sensitivity of granular media to boundary conditions. It can be said that the system's performance is partially influenced by the type of biasing plate. An in-depth understanding of the impulse wave propagation through such structures will aid modeling and quantitative analysis during design, for example, in determining the optimal cross-sectional thickness of the capsule for a particular design impact load. In this section, BCC structure has been evaluated from a structural point of view, incorporating tentative static and dynamic implications of impact loading. Generalized material properties are assumed throughout the modeling purposes.

5.2. BCC – The Illustrative Model

BCC can simplistically be looked at structurally as having the basic construction of one sphere resting centrally on top of other four spheres, with the pattern being repeated. Any loading onto the top sphere gets shared amongst the four spheres beneath it. Due to the disequilibrium nature of granular media, an effort has been made in separating the static and dynamic components of such loading in the ensuing modeling of impulse wave propagation. The dynamic component takes into account the absorptive aspect of the

spheres owing to elasticity of material, and dissipative aspect attributable to impulsive inter-granular collisions. The static component emanates from relative structural positioning of granules in a representative lattice unit cell, most importantly, the definitive lattice angle between normal lines of contact. It is imperative that the angle has effect on re-direction of the impulse wave vector, thereby affecting the resulting absorptive and dissipative granular mechanics. A three dimensional, nodal cross-sectional representation of BCC lattice structure is shown in Figure 5.1.

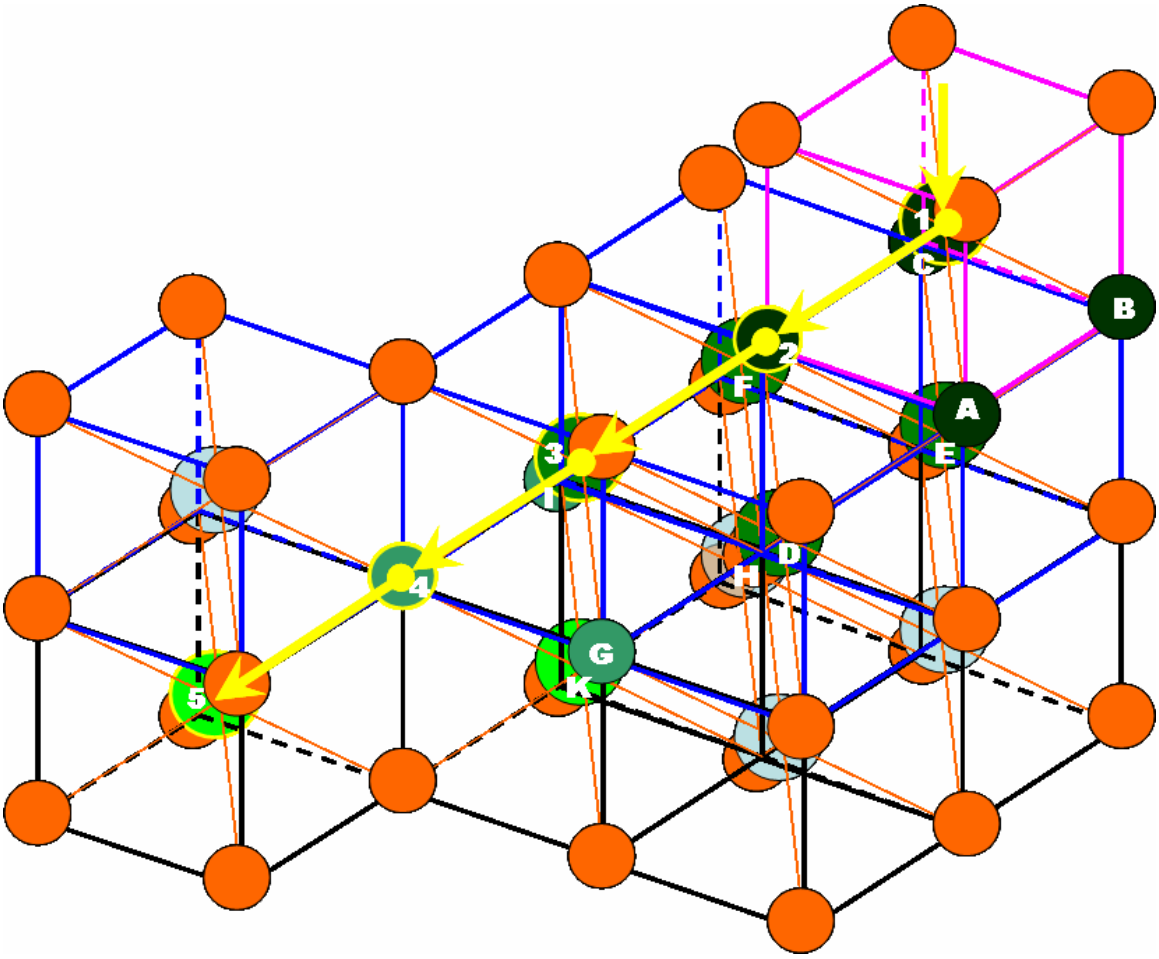

Figure 5.1: 3D nodal, cross-sectional representation of BCC structure.

The nodes are only illustrative of relative positions and are not representative of size, while the lines depict normal lines-of-contact through centres. Three different layers are

illustrated as differentiated by colour coding; (i) top layer – pink, (ii) middle layer – blue, and (iii) bottom layer – black. Wave propagation across the layers is in this context taken to be indicative of the depth of penetration from the incidence side, i.e. damping path along the (perpendicular) axis of impact. Length, width, and height of the structure is as cut out from a cubic block encompassing three unit cells in either of the three Cartesian planes.

5.3. BCC – The Vector Model

5.3.1. Primary Waves

Let the initial impulse, J, be incident on sphere 1, which is at the centre of a BCC structure as illustrated. Since impulse is a vector quantity unlike energy, and the initial direction may not necessarily be in the vertical axis, we may write;

$$J'_v = \beta J \qquad (1)$$

where J'_v is the incident impulse on sphere 1 in the vertical direction, and β is a correction trigonometric factor. For simplicity, it is assumed that there are no losses at the interface between the impact and sphere 1.

The impulse J'_v will be shared equally by the four balls lying in the plane perpendicular to the axis of incidence i.e. spheres 2, A, B, and C. The resultant vertical impulse incident on each of the four spheres will be equivalent to $\frac{1}{4} J'_v$ as illustrated in figure 5.2. The zig-zag section simply signifies an absorptive and/or dissipative interaction at any paired contact. Notice that θ is constant for all similar points throughout the BCC virtual lattice structure.

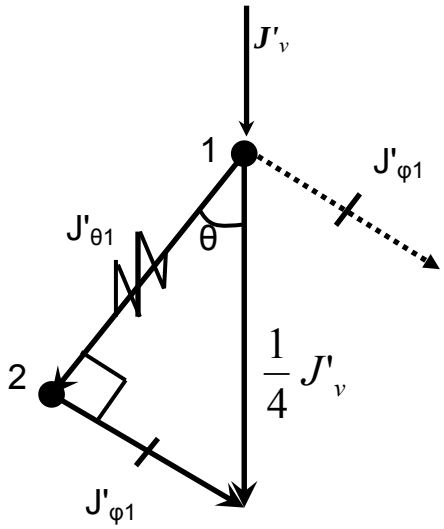

Figure 5.2: Impulse vector resolution.

Considering sphere 2 for instance and choosing the normal line of contact between spheres 1 and 2 to correspond with one of the perpendicular components of $\frac{1}{4} J'_v$, resolution into $J'_{\theta 1}$ and $J'_{\varphi 1}$ gives:

$$J'_{\theta 1} = \frac{1}{4} J'_v \, Cos\ \theta \quad , \tag{2}$$

and

$$J'_{\varphi 1} = \frac{1}{4} J'_v \, Sin\ \theta \quad , \tag{3}$$

Assuming imperfect elastic inter-granular collisions along normal lines, impulse incident onto sphere 2, $J'_{\theta 2}$ will only be a fraction of impulse from sphere 1 in that direction. Introducing a constitutive transfer dissipation factor, α, at every similar paired contact:

$$J'_{\theta 2} = \alpha \, J'_{\theta 1}$$

$$or \quad J'_{\theta 2} = \frac{1}{4} \alpha \, J'_v \, Cos\ \theta \quad , \tag{4}$$

With reference to physical implications of $J'_{h\theta 2}$ as illustrated in figure 5.3, the component $J'_{\theta 2}$ evidently has a dispersive effect on the incident impulse wave by virtue of re-directing it from the axis of incidence. This dispersive effect is dependent upon the size of angle θ as well as the magnitude of reaction vectors, which are on the other hand dependent upon the local hydrostatic pressure holding the structure in place. The component as modified by the transfer factor represents the dynamic aspect of the impulse wave propagation. It is influenced by the material from which the spheres are made and other factors that influence the nature of direct inter-granular collisions such as the bulk density, linear and/or angular velocity of spheres just before collision, and the effect of secondary collisions (re-bounds).

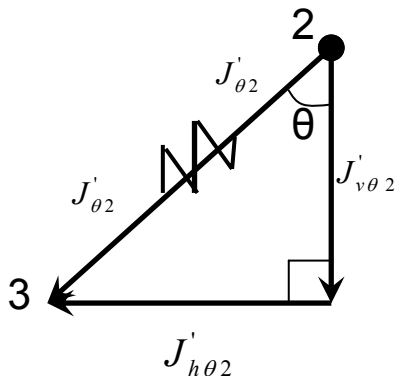

Figure 5.3: Resolution of the impulse along normal line of contact.

The corresponding vertical component of impulse acting on sphere 2 as a result of $J'_{\theta 2}$, may be obtained by resolving $J'_{\theta 2}$ as illustrated in Figure 5.3, giving:

$$J'_{v\theta 2} = \frac{1}{4}\alpha J'_{v} Cos\theta . Cos\theta \quad , \qquad (5)$$

It should be noted here that the $J'_{\varphi 1}$ is not directed to any particular sphere and is hence considered to contribute to general wave damping and disequilibrium of the entire

structure (secondary waves to be discussed later). Its effect is more relevant to the *static* than dynamic scaling of the structure and its influence on the system is predominantly dictated the lattice structure's geometry. Nevertheless, its vertical perpendicular component, $J'_{v\varphi 2}$, does reinforce the vertical component of $J'_{\theta 2}$ by virtual of contact between sphere 1 and 2, whereby:

$$J'_{v\varphi 2} = \frac{1}{4} J'_v \, Sin\theta . Sin\theta \quad , \tag{6}$$

Combining equations (5) and (6) gives total vertical component of impulse on sphere 2:

$$J'_{v2} = \frac{1}{4} J'_v \left(\alpha \, Cos^2\theta + Sin^2\theta\right) \quad , \tag{7}$$

Sphere 2 similarly rests on 4 other spheres, i.e. spheres 3, D, E, F. These spheres will equally share the vertical component of impulse incident on sphere 2 but not the component along the normal line of contact. The latter will fully be transferred onto sphere 3 only, subject to the transfer dissipation factor, α.

Accordingly, the normal component transferred to sphere 3, $J'_{\theta 3}$, from sphere 2 will be given by:

$$J'_{\theta 3} = \alpha J'_{\theta 2}$$

$$or \qquad J'_{\theta 3} = \frac{1}{4} \alpha^2 J'_v \, Cos\theta \quad , \tag{8}$$

The corresponding vertical component on sphere 3 due to $J'_{\theta 3}$ will be;

$$J'_{v\theta 3} = J'_{\theta 3} \, Cos\,\theta$$

$$or \qquad J'_{v\theta 3} = \frac{1}{4} \alpha^2 J'_v \, Cos\theta . Cos\theta \quad , \tag{9}$$

In addition to this, the vertical component from sphere 2 attributable to $J'_{\varphi 1}$ will be shared further by the four load bearing spheres;

$$J'_{v\varphi 3} = \frac{1}{4} J'_{v\varphi 2}$$

$$= \frac{1}{4}.\frac{1}{4} J'_{v}\, Sin\theta . Sin\theta$$

$$or \qquad J''_{v\varphi 3} = \left(\frac{1}{4}\right)^2 J''_{v}\, Sin\theta . Sin\theta \quad , \tag{10}$$

By combining equations (9) and (10) we obtain the total vertical impulse on sphere 3:

$$J'_{v3} = J'_{v\theta 3} + J'_{v\varphi 3}$$

$$= \frac{1}{4}\alpha^2 J'_{v}\, Cos\theta . Cos\theta + \left(\frac{1}{4}\right)^2 J''_{v}\, Sin\theta . Sin\theta$$

$$or \quad J'_{v3} = \frac{1}{4} J'_{v}\left(\alpha^2 Cos^2\theta + \frac{1}{4} Sin^2\theta\right) \quad , \tag{11}$$

Sphere 4 similarly receives the normal component from sphere 3 subject to the constant dissipation factor and an equitable share of $J'_{\varphi 1}$ as the rest of spheres G, H, and I:

$$J'_{\theta 4} = \frac{1}{4}\alpha^3 J''_{v}\, Cos\theta \tag{12}$$

$$and \quad J'_{v4} = \frac{1}{4} J'_{v}\left(\alpha^3 Cos^2\theta + \left(\frac{1}{4}\right)^2 Sin^2\theta\right) \quad , \tag{13}$$

In general: $$J'_{\theta n} = \frac{1}{4} J'_{v}\left(\alpha^{n-1} Cos\theta\right) \tag{14}$$

$$and \quad J'_{vn} = \frac{1}{4} J'_{v}\left(\alpha^{n-1} Cos^2\theta + \left(\frac{1}{4}\right)^{n-2} Sin^2\theta\right) \quad , \tag{15}$$

At this point, notice that equations (14) and (15) bear a common term $\left(\frac{1}{4}J_v^{'}\right)$, which is may be considered a structural signature of impulse wave "sharing". Since the angle θ for a particular lattice structure is also a constant, it simply means that the propagation in the longitudinal direction is purely dependent upon the dissipation factor α whereas propagation in the vertical direction is further influenced by virtual structural geometry. As the number of iterations increase to n >>> 1, both the vertical and longitudinal impulse vector components tend to 0 (a typical wave damping phenomenon). Damping factors in both cases vary between zero and unity. It is imminent that these factors will be equal at some point, in which case:

$$\alpha^{n-1}Cos\,\theta = \alpha^{n-1}Cos^2\theta + \left(\frac{1}{4}\right)^{n-2}Sin^2\theta$$

$$or \qquad Cos^2\theta - Cos\,\theta + \left(\frac{1}{4}\right)^{n-1}\alpha^{1-n}Sin^2\theta = 0 \quad , \qquad (16)$$

This is typical of a quadratic equation of the general form $Ax^2 - Bx + C = 0$ with two possible solutions. It is suggested hereby that, these two possible points represents two nodes of impulse wave interference. This implies some form of bifurcations within the granular media in the vicinity of impact incidence.

5.3.2. Secondary Waves

There are at least two sources of secondary impulse waves within the structure: (1.) Re-bounds or reverberations at paired contacts along the path of $J_{\theta n}^{'}$. This category of waves will tend to propagate along similar path as their parent waves. (2.) Waves due to non-equilibrium state of the system as a result of, among others, (i.) effects of $J_{\varphi 1}^{'}$ type of impulse wave vectors, and (ii.) insufficiency of hydrostatic pressure as induced by the

encapsulating membrane, i.e. weaker reactions to $J'_{h\theta n}$ vector components resulting to intra-layer collisions as illustrated in Figure 5.4. Horizontal straight lines represent centre

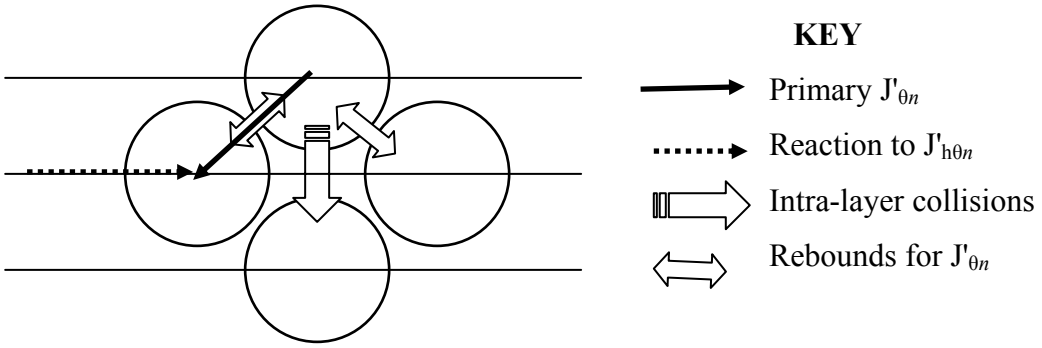

Figure 5.4: Scheme of secondary impulse waves.

planes for three granular layers in a BCC lattice structure. Gaps between the spheres simply indicate the instability associated with paired contacts during collisions.

It is expected that the intra-layer secondary waves do form absorption / dissipation patterns as their parent wave, J', i.e. being re-directed as $J'_{\theta n}$ and $J'_{\varphi n}$. This would result into an array of conical wave damping paths. The conical formation would be symmetrical about the central axis of impulse incidence subject to the trigonometric correction factor, β. Possible interferences between primary and secondary waves would result to clearly defined bifurcations bands. It may be difficult to witness the pertinent impulse wave propagations phases as discussed herein due to: (1.) instability of the transient virtual structures, and (2.) the short time-scales aspect of impact impulse waves. Nevertheless, the damping effect of these structures on the incident impulse wave prevails.

5.4. BCC - Quantitative Example

Working with a tentative factor $\alpha = 0.5$, $\theta = 55^0$ (Approximate θ for BCC), and initial

incident impulse $J_v^{'}$ = 100Ns, typical values of $J_{\theta n}^{'}$ and $J_{vn}^{'}$ are tabulated in Table 5.1, with part 2 of the table showing values for similar data but with a transfer factor of 0.75. Due to space limitations, only values for 6 layers have been presented on the table but the workings were extended to at least 13 layers.

Ball Numbering (*n*) i.e. Vertical Position	1	2	3	4	5	6
Longitudinal position	0	1	2	3	4	5
Part 1 (α = 0.5)						
$J_{\theta n}^{'}$	0	7.170	3.585	1.792	0.896	0.448
$J_{vn}^{'}$	100	20.888	6.250	2.077	0.776	0.323
Part 2 (α = 0.75)						
$J_{\theta n}^{'}$	0	10.755	8.066	6.049	4.537	3.403
$J_{vn}^{'}$	100	22.944	8.820	4.518	2.864	2.017

Table 5.1: Sample working values for BCC

Graphical representation of the values is shown in Figure 5.5 below. On the horizontal axis, *n* represents the spheres as numbered in Figure 5.1 as well as the order of granular layers. The second scale starting from 0 represents the distance from incidence axis (*d.i.a*) in terms of unit lattice cells. Since values of the magnitude of $J_{vn}^{'}$ at start are much greater than maximum value on the graph, the respective starting sections have been left out from the graph (first two layers).

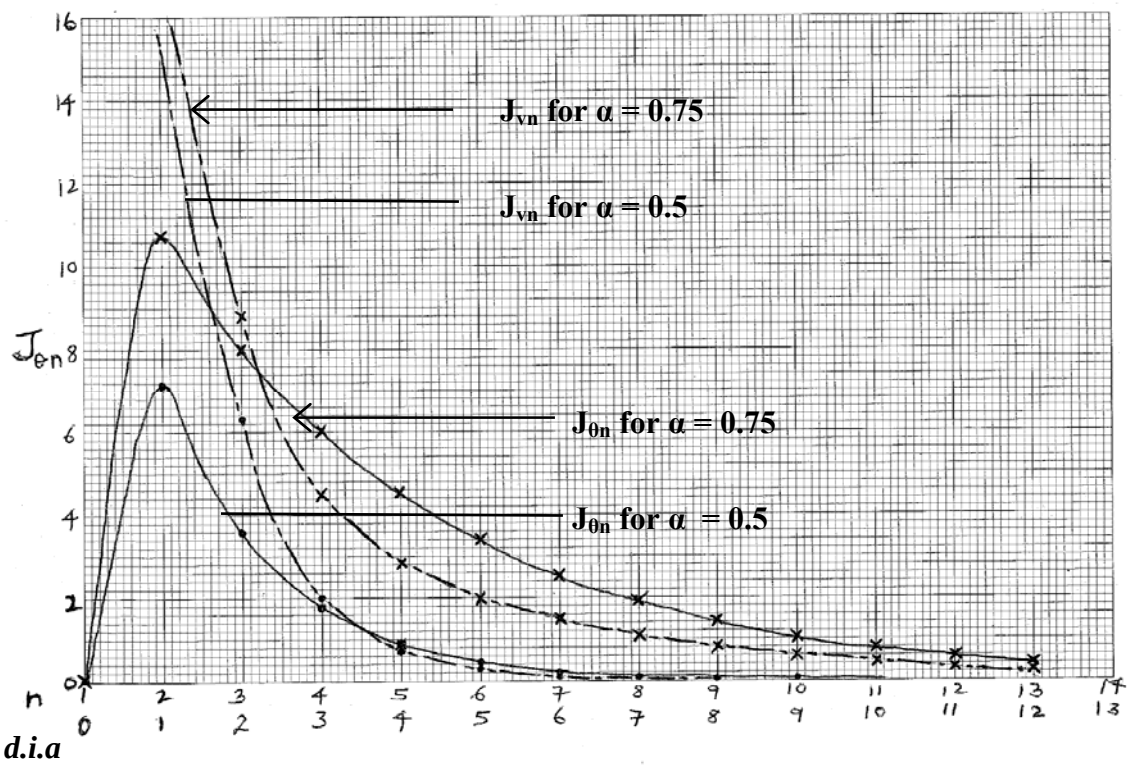

Figure 5.5: Graphs of $J'_{\theta n}$ and J'_{vn}.

Both graphs of $J'_{\theta n}$ are highly skewed to the right and asymptotic. This interprets to greater impulse dispersion in close proximity to the axis of incidence. The extent of wave propagation in the longitudinal direction seems to vary proportionally with the transfer factor. Sharp peakedness represents the abrupt critical aversion of impulse wave upon interception by the structure's first layer.

A similarity of trend is also evident for J'_{vn} graphs for both transfer factors. They both portray a very sharp gradient over the first few layers, a feature commonly associated with granular media when subjected to high strain rates. Both graphs are also asymptotic but with a higher damping rate than their corresponding $J'_{\theta n}$ counterparts.

An insight into the marginal variation of $J'_{\theta n}$ and J'_{vn} from one layer to the next indicates

that they stabilize at almost the same time. For $\alpha = 0.5$, this occurs at around the 10^{th} and 11^{th} layer (or 9 and 10 unit cells from the axis of incidence). This stabilization region is an important design factor in that it hints towards the optimal number of granular layers for a particular set of incident impulse and transfer factor. As a rule of thumb, the number of layers suggested by the stabilization region may be considered to be more than the actual number required because in practice, impulse will more often than not be incident upon more than one granule, thereby resulting into more sets of propagation paths, increased interferences, and implicitly more damping effects. However, this should be considered in the light of suitably determined design safety factors.

It is worth noting the convergences between $J'_{\theta n}$ and J'_{vn} as predicted by equation (16). As can be seen from the graph, the first convergence occur within the first few layers (J'_{vn}) and a few lattice cells away from the axis of impulse incidence ($J'_{\theta n}$). Thereafter, the value of J'_{vn} remain consistently lower than $J'_{\theta n}$ until their next convergence towards Zero. This partly explains the reasons as to why longitudinal deformation was consistently greater than vertical deformation during experimental validation of the proposed system as documented in Chapter 4.

From a practical design point of view, the concept of equal distribution of incident impulse amongst granules of the intercepting layer holds true. Considering a motor vehicle of 2000 Kg traveling at 90 Km/h (or 25m/s), the total impulse works out to 50,000 Ns. Using a BCC structure with a set of design elements collectively giving a transfer factor of 0.5, this relates to a layer of 500 granules, each carrying 100 Ns. Assuming the spheres to be equal in size with a diameter of 16mm, this would mean an

interface layer of, say, 50 x 10 granules, which would fit in a bumper fascia area measuring approximately 1m x 0.2m (Length x Width) and about 10 layers interpreting to approximately 0.1m. Bearing in mind that currently active standards call for 8 Km/h (or 2.22m/s), this dimensional analysis not only exemplify the great potential of the proposed system with respect to design space optimization, but also the possibility of raising the benchmark.

CHAPTER 6:

IMPACT ENERGY MANAGEMENT

6.1. Introduction

As mentioned earlier, glass is generally known to have a low impact or crash strength. Experimental drop-weight tests conducted cyclically on the proposed system from a height of 0.3m (2, 43 m/s or 8, 73 km/h) showed no breakage of the system's glass beads. The statutory stipulated FMVSS velocity is 8km/h for automotive bumper systems. This shift of design focus from material's strength to dissipation dynamics may be optimized through analytical review of the systems behavior and variation of the system's parameters and / or loading conditions. In light of the numerous possible design applications, an effort to circumvent experimentation is explored. A mathematical analysis has been done as another helpful design tool. Focus is on the system's impact energy management mechanisms.

The system has been broken down into four main components; the *skin, encapsulating-membrane*, *granular media*, and *base plate*. Each one of them is considered to absorb and/or dissipate impact energy through one or more mechanisms. Factors affecting the efficiency of each component in the global context of the system have been investigated and considered in the mathematical modelling process.

6.2. Mathematical Model – The Sandwich Concept

For purposes of the modeling process, the sandwich concept has been adopted. None of the components through the thickness is bonded to each other, including the granular medium. At any point of impact incidence, the system's components may be considered

to constitute a *non-bonded sandwich panel,* with different impact energy absorption and/or dissipation mechanism as illustrated in Figure 6.1 below:

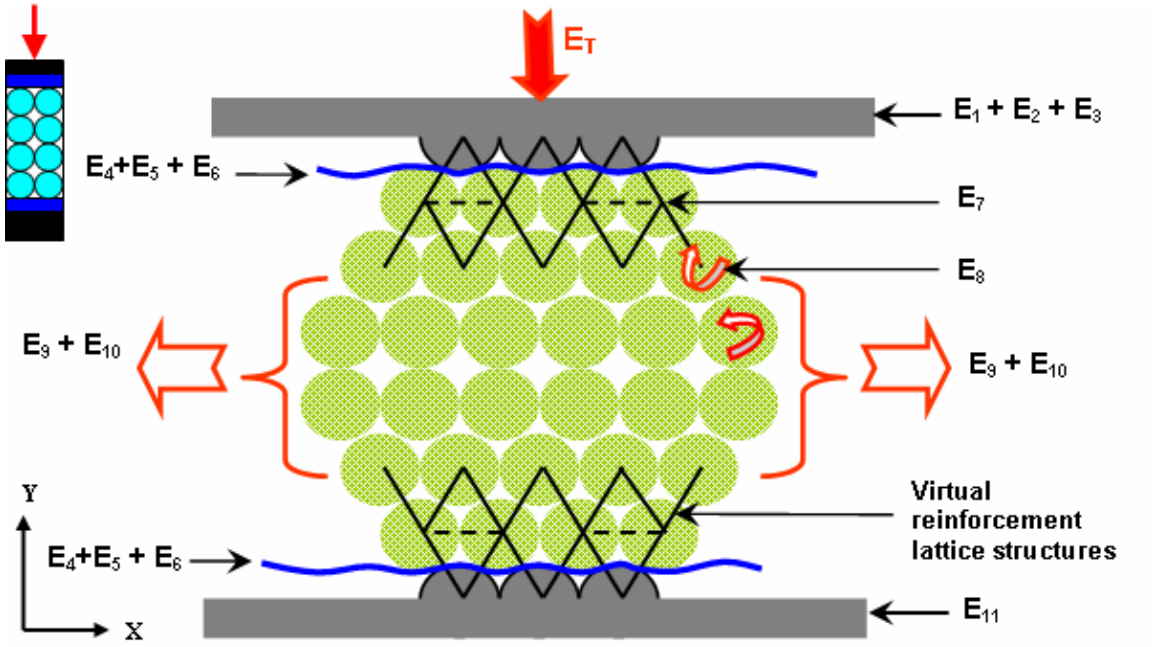

Figure 6.1: Scheme of energy absorption / dissipation components.

By applying the *energy balance approach*, total impact energy absorbed and/or dissipated by the system, E_T, will be given by:

$$E_T = \sum_{i=1}^{10} E_i \qquad (1)$$

where E_i = energy absorbed / dissipated by components A, B, C, and D in different modes. Each mode is unique to the properties of the constituent material as well as the geometrical features and inherent behavior.

In the mathematical modeling process, three general assumptions have been made;

(1.) that no failure occurs: i.e. the system absorbs and/or dissipates all the impact energy (within the design range) without damage to the constituent components, and maintains its intact profile after the impact). (2.) The spheres are to be in uniform contact with each

other *before* and *after* loading cycles. (3.) Energy dissipation through heat and sound is considered to be minimal. (4.) Minimal pre-stretch of the membrane before and after loading. (5.) There is sufficient minimal support of the back (base) plate e.g. from body panels of the vehicle.

6.3. The skin / Fascia

Main modes of energy absorption visualized for this component are: (a) Energy as a result of elastic compression of the component's wall, localized at the area of impact contact surfaces; E_1, (b) Energy attributable to shear stresses; E_2, and (c) Energy due to elastic deflection, localized around the impact incidence region; E_3.

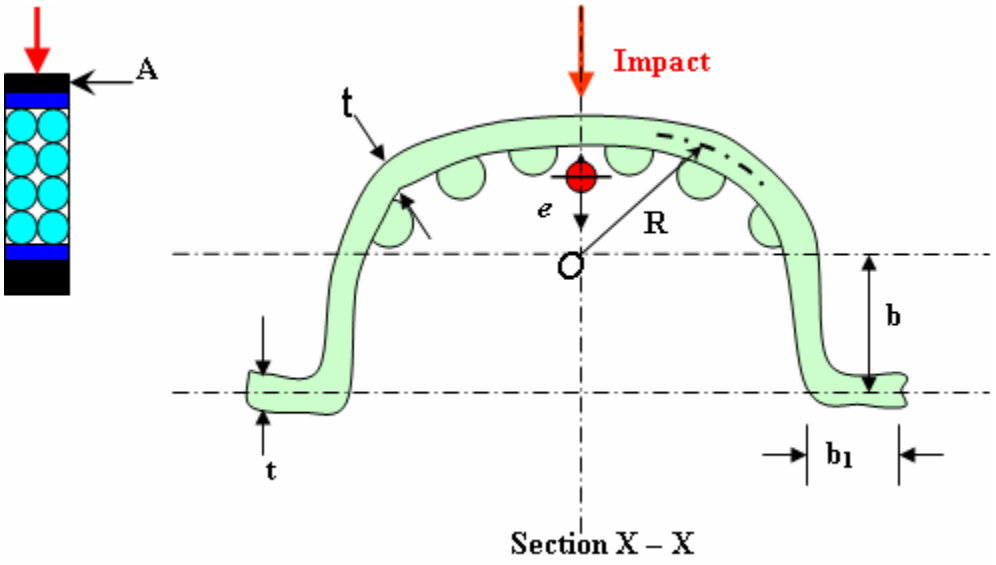

Figure 6.2: Fascia cross-section.

6.3.1. Energy due to elastic wall compression, E_1

In the context of an automotive bumper system, Figure 6.2 shows a typical general transverse cross-section of a fascia (*skin*). By virtue of the cross-sectional thickness *t* being small, the energy absorbed by way of localized elastic compression of the material, E_1, may be considered negligible and has consequently been neglected.

6.3.2. Shear stresses energy, E_2

At the point of impact, the load will induce transverse shear stresses τ_{xy} and τ_{xz} in the section due to the nature of loading as illustrated in Figure 6.3. This is in addition to the normal stress, σ_x due to flexure. Assuming the load acts through the shear centre, no shear stress τ_{xy} and τ_{xz} due to torsion are in play.

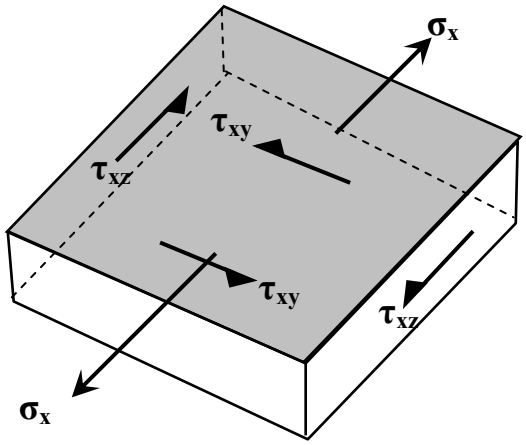

Figure: 6.3: Normal and transverse stresses.

From the general cross-sectional profile shown in Figure 6.2, the shear centre [36] is considered to be at a distance *e* from *O* where:

$$e = \left\{ \frac{12 + 6\pi\frac{b+b_1}{R} + 6\left(\frac{b}{R}\right)^2 + 12\frac{b}{R}\frac{b_1}{R} + 3\pi\left(\frac{b_1}{R}\right)^2 - 4\left(\frac{b_1}{R}\right)^2\frac{b}{R}}{3\pi + 12\frac{b+b_1}{R} + 4\left(\frac{b_1}{R}\right)^2\left(3 + \frac{b_1}{R}\right)} \right\} \qquad (2)$$

One can simplify equation (2) by varying *b* and b_1 or even putting them to zero. Energy absorption attributable to global bending moments has consequently been considered to be negligible as compared to the localized elastic strain energy at this zone. As such, the conventional two-dimensional deformation theory is rendered inadequate. Instead, a non-linear model developed by David J. Steigmann [37, 38] has been adopted, estimating the

energy of a thin body generated in response to a given kinematically possible three-dimensional deformation.

6.3.3. Elastic strain energy, E_3

Based on the localized nature of deformation conceptualized at this zone, the Euler equations for the estimate of strain energy are deemed applicable. The total strain energy, E_3, may be given by adapting Steigmann's equation [38] as;

$$E_3 = \int_k U\left(\vec{F}(x)\right)dV = E + O\left(\varepsilon^5\right), \tag{3}$$

where $E = \int_\Omega W\left(d, g, h, F, D, G\right)dA$ (4)

in which $W = \varepsilon U\left(F + d \otimes k\right) + \frac{1}{24}\varepsilon^3 \begin{Bmatrix} P\left(F + d \otimes k\right).\left(G + h \otimes k\right) \\ + \mathrm{M}\left(\mathrm{F} + \mathrm{d} \otimes \mathrm{k}\right)\left[D + g \otimes k\right].\left(D + g \otimes k\right) \end{Bmatrix}$ (5)

is the strain energy through order $O(\varepsilon^4)$ per unit area of Ω, $r(u)$ $(= \hat{y}_0)$ is the map from the plate mid-surface Ω to its deformed image, ω, and d(u), g(u), h(u) are *director* fields defined on Ω. These are the coefficient vectors in the expansion;

$$\hat{y}\left(u,\zeta\right) = r(u) + \zeta\, d(u) + \frac{1}{2}\zeta^2 g(u) + \frac{1}{6}\zeta^3 h(u) + O(\zeta^4)\,, \tag{6}$$

and $F = \nabla r$ maps Ω' to the tangent plane $T_{\omega(u)}$ of the deformed mid-surface ω at point r(u). However, since it may be cumbersome to ascertain some of these parameters in practice, the general equations for thin plate or slender beams may be used for estimation purposes.

6.4. Thin Encapsulating Membrane

6.4.1. Localized elastic compression; E_4

Rubber and other elastomeric materials are basically cellular in structure, allowing a certain percentage of set under compression. This energy absorption mode applies to membrane impact points that are tangentially sandwiched between encapsulated granules

and the skin's biasing hemispheres. By virtue of the membrane thickness (+/-1mm) and impact surface area, energy so absorbed has been considered negligible, and hence neglected. Since there is no significant relative motion between the membrane and surfaces around it during impact, energy dissipation through friction has also been deemed negligible and similarly ignored.

6.4.2. Elastic Membrane Stretching

6.4.2.1. Global Elastic Strain Energy; E_5

In the context of an automotive bumper system, transverse (z – axis) deformation has conceptually been constrained to minimal, in order to maximize *free* granular media flow in the x (longitudinal) and y (axis of incidence) directions. Since the encapsulated granular content is not a rigid solid, and the stretch is differential, stretching of the membrane will tend to be localized at the region of impact incidence, as well as at the two free extreme ends of the capsule along longitudinal axis. Degree of stretch will, however, be a maximum at the point of impact as the impacting object seeks to displace a bulk granular volume equivalent to its own. For modeling purposes, the impact loading is assumed to be below some critical value that would cause membrane failure by rupturing / tearing off, taking thermal-effects into consideration and other working environmental conditions.

To model the stretch effect, an axisymmetric deformation of a circular membrane by a smooth sphere as illustrated by Kuo Kang Liu and Bing Feng Ju [39] has been adopted – see Figure 6.4.

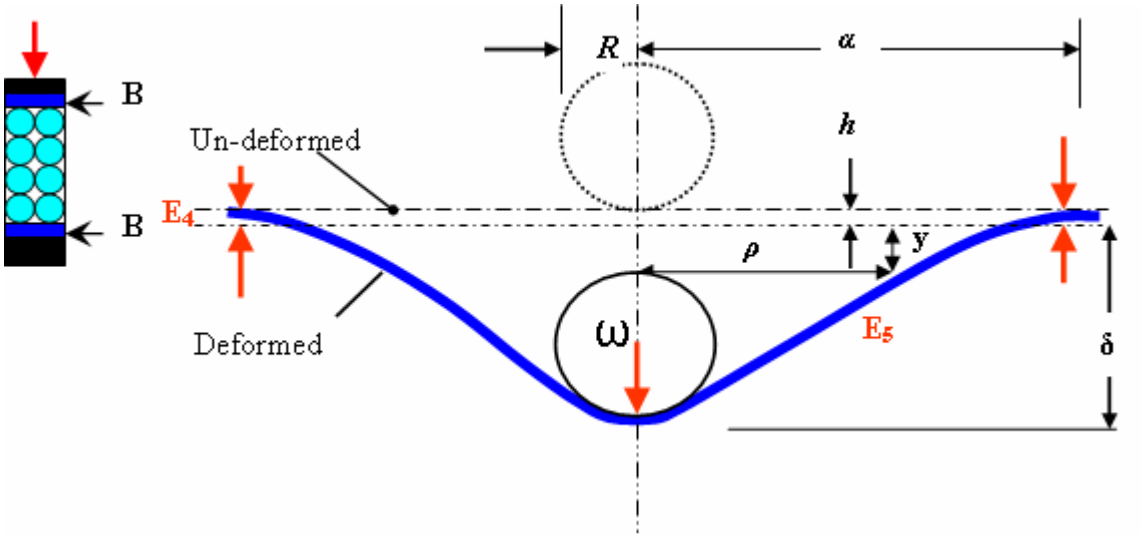

Figure 6.4: Sketch of membrane deformed by a sphere.

It is suggested that when a central load ω is applied to a film, which has elastic modulus *E*, undeformed radius *a,* and thickness *h*, via a sphere of radius *R*, a displacement δ will correspondingly occur at the pole [39]. The membrane was assumed to be an isotropic 3D incompressible (rubber-like) material exercising a Mooney-Rivlin constitutive behavior. For such a material, the strain-energy function, W, was accordingly given as:

$$W = C_1(I-3) + C_2(II-3) = C_1[(I-3) + \alpha(II-3)] \qquad (7)$$

where C_1 and C_2 are the material constants with the dimensions of stress, C_1 is equal to $E/6$; $\alpha = C_1/C_2$ and its value was given as 0.1 in their study. The parameters *I* and *II* are the strain invariants which may be expressed in terms of the principal stretch ratios, λ_1 and λ_2, as $I = \lambda_1^2 + \lambda_2^2 + \lambda_1^{-2}\lambda_2^{-2}$ and $II = \lambda_1^{-2} + \lambda_2^{-2} + \lambda_1^2\lambda_2^2$.

Numerical solutions of the governing equations give the relationship between the force applied to the membrane and its corresponding deformation [39]. They gave their result in terms of dimensionless load Y and deformation X, respectively, as:

$$Y = \frac{6\varpi}{E\,h\,R} \tag{8}$$

and $$X = \frac{\delta}{R} \tag{9}$$

For membrane of $a/R = 5.0$ and without pre-stretch, Y can be given as a function of X [39]

$$Y = 0.78\,X + 0.075\,X^2 \qquad (0 \le X \le 1.7). \tag{10}$$

In this equation, the parameter X is calculated based on the measured central displacement δ normalized by R. The profile of the deformed membrane can be computed and expressed in terms of the distance ρ and displacement δ from the central axis to a specific point at membrane.

Since the granules are incompressible and assumed to be in uniform contact, displaced granular volume at impact incidence region approximately equals the granular volume stretching the membrane axially at the free ends. As such, arithmetic sum of strain energy at both longitudinal ends equals the strain energy at impact incidence region. Using W as obtained from Eqn. (7), total strain energy may thus be approximated as:

$$E_5 = 2W \tag{11}$$

6.4.2.2. Distributed Local Elastic Strain Energy; E_6

At the impact interface, encapsulated granules at the periphery tend to lock into receptive spaces created by the biasing hemispheres lining the interior walls of skin and base plate. Assuming little or no sliding between hemispheres and membrane, the peripheral granules individually stretch the membrane locally. The strain energy absorbed may be approximated as:

$$E_6 = 2\,n\,W_g \tag{12}$$

where W_g is the strain energy per locked granule within the impact incidence surface area A, and n is the number of the so locked spheres (granules). Equation (7) applies equally in determination of W_g. Multiplier factor of 2 serves to accommodate the reflective effect of skin and base plate hemispheres. Area A depends on shape of impactor surface, and the relationship between A and n varies from one lattice structure to another, e.g. for BCC,

$$n = \frac{3}{16}.\frac{A}{r^2} \tag{13}$$

where r is the radius of granules. This latter equation varies from one lattice to another.

6.5 The Encapsulated Granular Media Layer

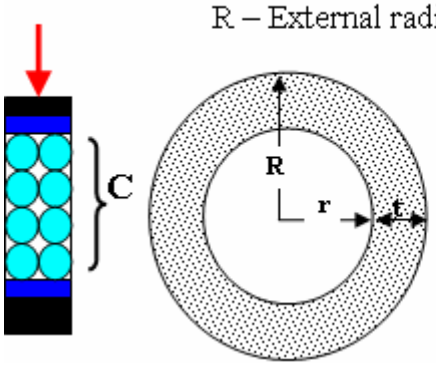

r – Internal radius
R – External radius

Tentative Ø = 10mm
α = r / R

α	0.75	0.67	0.50	0.33	0.25	SOLID
r	3.75	3.33	2.50	1.67	1.25	
t	1.25	1.25	2.50	3.33	3.75	5

Figure 6.5: Solid / Hollow / Soft-core Spheres.

Sample sphere and inherent sample relations for a 10mm diameter are illustrated in Figure 6.5. The possible energy absorption and/or dissipation modes for this section of the assembly are (1.) normal forces perpendicular to contact plane, through virtual lattice geometry; E_7, (2.) static and sliding friction parallel to the contact plane; E_8, and (3.) global linear displacement; E_9, as a result of collapse of unit local lattice structures and granular fluid flow at the interior of the capsule. However, these phases are interdependent, characterizing discrete granular transitional dynamics synonymous to that

of an incompressible fluid.

At this zone, it is hereby contended that the impact force engages the encapsulated spheres at three inter-dependent phases. (1.) the biasing hemispheres lock the peripheral spheres in the capsule into lattice structural arrangement by default. This process is consequential to the so called 'geometric frustration' [40] typically known to characterize hard-sphere systems. This kind of frustration is generated by the constraints imposed by the hard-core repulsion of neighboring grains and the subsequent interlocking which leads to non-local cooperative macroscopic re-arrangement. (2.) as far as possible, the lattice structures so formed will behave like a structural reinforcement grid beneath the elastomeric membrane. Energy will be absorbed elastically by way of normal forces at the points of contact of adjacent spheres along the line joining their centers. During this phase, no slipping is contemplated. (3.) As the impacting object seeks to displace a global volume of spheres equivalent to its own volume, the lattice structural dimensions will disintegrate, starting with the spheres furthest from the biasing hemispheres – apparently spheres at the central axis of the capsule. This disintegration will entail massive energy dissipation through slipping, instantaneous inversion of unit lattice structures, and initiation of rapid granular flow.

During the three phases, random collisions will be dominant and energy dissipation and / or absorption will be dependent on the nature of the collisions, which are on the other hand dependent on magnitude and rate of the incident impact. Despite every sphere being in constant contact with more than one other sphere (8 for BCC, 4 for FCC and 3 for Simple cubic lattice), the contact between any pair is typically representative of any other

pair of contacts. However, not all of these contacts are load bearing, especially with reference to the normal component. The distribution of the impact force as shared amongst the impact bearing spheres (4 for BCC, 2 for FCC and 1 for Simple cubic), and the angle of distribution varies from one lattice structure to another. The paired collision model has been adopted in analyzing the energy balance implications in this zone of the capsule.

In modeling oblique collisions of elastic spheres, Maw, Barber, and Fawcett [41] extended the Hertz theory of impact, and through numerical integrations of the forces involved during the collisions, established that three regimes exist in a typical impact. At *low angle* of incidence, the contact surfaces always include a central region where the particles stick, while at *high values of this angle*, slipping persists throughout the collision. At *intermediate angles*, the collision involves both sticking and slipping contacts. They showed that under suitable circumstances, elastic strain energy stored in the solid is recoverable, so the tangential velocity of the point of contact may be reversed.

On the basis that theories of rapid granular flows cannot realistically incorporate the details of the Maw, Barber, and Fawcett theory, and because real spheres are inelastic, Walton proposed a simplified impact model based on three constant coefficients [42]. The *first* characterized the incomplete restitution of the normal component of the relative velocity at the point of contact. The *second* arises in collisions that involve sliding. Here, the latter is assumed to be resisted by Coulomb friction, and the tangential and normal components of the impulse are related by the coefficient of friction. The *third* arises in collisions that return a fraction of the energy stored on elastic deformation of both

surfaces to the component of the contact velocity tangent to the spheres. Here, Walton assumes for simplicity that these collisions do not involve sliding and treats the reversal of the tangential velocity at the contact point using a constant coefficient of tangential restitution.

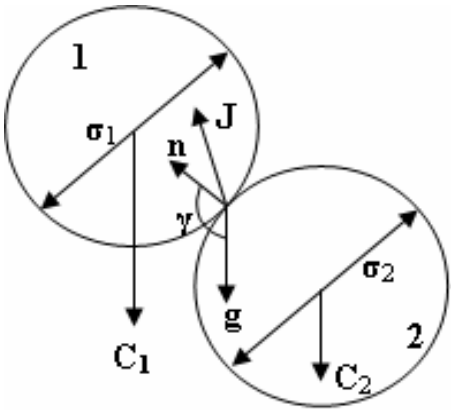

Figure 6.6: Typical geometry of a binary collision projected on the collision plane as depicted by Foerster et al. The velocities are shown before the impact.

Figure 6.6 shows the adopted binary collision as depicted by Samuel F. Foester et al [43]. They experimentally calculated the velocities of the particles emerging from a collision from the balances of linear and angular momenta and from the relations prescribed by Walton's impact model. They showed that a simple model based on three constant coefficients (Coulomb friction, normal, and tangential restitution) captures the behavior of the impact over a wide range of incident angles. However, they differed with the model to the extent of demonstrating that the tangential coefficient is not a constant. They considered two colliding spheres of diameters σ_1 and σ_2 and masses m_1 and m_2 with centers located at r_1 and r_2.

During the collision, sphere 2 exerts an impulse J onto sphere 1 [43]. Accordingly, the velocities before and after collision can be related by:

$$m_1\left(c_1^{'}-c_1\right)=-m_2\left(c_2^{'}-c_2\right)=J \tag{14}$$

and $$\left(2\frac{I_1}{\sigma_1}\right)\left(\varpi_1^{'}-\varpi_1\right)=\left(2\frac{I_2}{\sigma_2}\right)\left(\varpi_2^{'}-\varpi_2\right)=-n\times J\,, \tag{15}$$

where C_1 and C_2 are the translational velocities, ω_1 and ω_1 are the respective angular velocities prior to the collision, $I = m\sigma^2/10$ is the moment of inertia about the centre of a homogenous sphere, and $n \equiv (r_1 - r_2) / | r_1 - r_2 |$ is a unit normal defined along the line joining the centers of the two spheres. The primes denote the corresponding post-collision velocities.

In order to determine the impulse, the relative velocity g of the point of contact was defined [43] as:

$$g=\left(c_1-c_2\right)-\left(\frac{\sigma_1}{2}\varpi_1+\frac{\sigma_2}{2}\varpi_2\right)\times n. \tag{16}$$

In the normal contact phase, Eqns. (14) and (15) have been used to relate the contact velocities before and after collision as [43]:

$$g^{'}-g=\left(\frac{7}{2m^*}\right)J-\left(\frac{5}{2m^*}\right)n\left(J.n\right), \tag{17}$$

where $m* \equiv \left(m_1^{-1}+m_2^{-1}\right)^{-1}$ is the reduced mass. The usual coefficient of restitution e characterizes the incomplete restitution of the normal of g [43],

$$n.g^{'}=-en.g\,, \qquad 0\le e\le 1 \tag{18}$$

In the sliding phase, the tangential and normal components of the impulse are related by the coefficient of friction μ [43],

$$|\,n\,\mathrm{X}\,J\,|=\mu\,(n\,.\,J), \qquad \mu\ge 0 \tag{19}$$

Combining Equations (15), (16) and (17) provides an expression for the impulse in terms of the normal and tangential components of g [43],

$$J^1 = -m^*(1+e)(g.n)n + \mu m*(1+e)\times \cot\gamma\left[g - n(g.n)\right], \tag{20}$$

where the superscript (1) denotes collisions that involve sliding as contemplated in phase (1.) and (3.), and γ is the angle between g and n,

$$\cot\gamma \equiv g.n \,/\left|g\times n\right| \tag{21}$$

As γ increases, sliding is deemed to cease when

$$n\times g^{'} = -\beta_0 n\times g\,, \tag{22}$$

or equivalently at a value γ_0 of the collision angle, such that

$$(1+\beta_0) = -\frac{7}{2}(1+e)\mu\cot\gamma_0\,, \qquad 0\le\beta_0\le 1 \tag{23}$$

where β_0 is the tangential coefficient of restitution [43].

In this simple model, collisions with $\gamma \ge \gamma_0$ were assumed not to involve sliding, in which case the impulse was found by combining Eqns. (17), (18), and (22),

$$J^2 = -m*(1+e)(g.n)n - \left(\frac{2m*}{7}\right)(1+\beta_0)\left[g - n(g.n)\right], \tag{24}$$

Likewise in this expression, the superscript (2) denotes collisions that do not involve sliding, as contemplated in phase (2.).

6.5.1. Virtual Reinforcement Elastic Energy, E_7

Generally, impulsive energy dissipation implications for any of the aforementioned three phases, E_{J_i}, may be expressed as:

$$E_{J_i} = \frac{1}{2} V J_i N_i \tag{25}$$

where V is the impact velocity onto the system, J_i is the impulse at phase i, and N_i is the average number of load bearing contact pairs for the particular lattice structure at phase i, and is dependent on the contact area of impacted surface, A, size of spheres (radius r), and depth of the impulse at that particular phase as determined along the axis of impact incidence. For simplicity, depth may be expressed in terms of equivalent number of granular layers.

By using the value of impulse J as given in Eqn. (24) for phase 2, E_7 works out to:

$$E_7 = E_{J_2} = \frac{1}{2} V J_2 N_2 \tag{26}$$

For instance, since only 4 out of 8 pairs of granules that form a unit BCC lattice are load bearing, the corresponding value of N_2 may be derived as:

$$N_2 = \frac{1}{2} n_2 \tag{27}$$

where n_2 is the number of granules active at phase 2. For BCC, n_2 may be determined as:

$$n_2 = \frac{3}{16} . \frac{A}{r^2} . d_2 \tag{28}$$

where A and r are as defined in Eqn. (13), and d_2 is the depth of impulse propagation through phase 2. It is worth noting that for two or more integrated layers of paired contacts, all pairs of contact become load bearing and as such, $n_2 = N_2$.

Value of d_2 is determined from the impulse wave propagation as modeled in Chapter 5 i.e. estimating the layer at which the impulse wave tends toward zero. The general equations were given as:

$$J'_{\theta n} = \frac{1}{4} J'_v \left(\alpha^{n-1} Cos\,\theta \right) \tag{29}$$

$$and \quad J'_{vn} = \frac{1}{4} J'_v \left(\alpha^{n-1} Cos^2\theta + \left(\frac{1}{4} \right)^{n-2} Sin^2\theta \right) \quad , \tag{30}$$

where $J_{\theta n}$ and J_{vn} denotes corresponding dispersive and vertical impulses at nth granular layer, α is the dissipative impulse transfer factor for the paired contacts; θ is the angle between J_v and J_θ; Since these equations are independent of radius of the granules, size does not count. Angle θ is a constant for any particular lattice structure and J is independent of the dissipative mechanisms of the system. This leaves α as the only determinant factor of the dissipative behaviour thus determined at phase 2.

6.5.2. Paired Contacts: Sliding / Spinning / Frictional Dissipation, E_8

Using the value of impulse J as given by Eqn. (20), energy dissipated at phase 1 and 3 may be determined as:

$$E_8 = E_{J_1} + E_{J_3} \quad = \frac{1}{2} V J \left[N_1 + N_3 \right] \tag{31}$$

where, for simplicity purposes $N_1 \approx N_3 = 8(d\text{-}1)$ for BCC.

6.5.3. Energy dissipation due to granular shear flow; E_9

Granules in this section of the capsule may be analyzed from a hydrostatic perspective. Analysis of factors that configure granular flow may hereby be broadly categorized into at least three clusters of properties: (1) Inelastic-Vs-Elastic particles, (2) Smooth-Vs-Frictional particles, and (3) Homogenous-Vs-Heterogeneous particulate composition. Other equally important aspects of granular media are the geometry of individual particles (determines the granular packing in space), the hydrostatic pressure and boundary conditions; the nature of confinement.

In context of the granular capsule within the conceptual bumper assembly model, flow may be simplified to a uni-axial flow for analytical purposes. Argument here is that flow in the vertical and transverse directions will be negligible as compared to the longitudinal flow along the central X-axis. Since the flow will be a response to an impact, it will accordingly be instantaneous, possibly resulting in permanent dislocation of individual granules despite reform of the capsule to normal profile after withdrawal of the impact; thus a mode of energy dissipation.

Predictions for rapid granular flow are derived from kinetic theories that exploit analogies between the colliding particles and agitated molecules in a dense gas [44]. The theories produce a set of partial differential equations and boundary conditions. Due to the necessary simplification of cases for analytical solutions purposes, these differential equations are generally solved numerically by discretizing the flow domain and by employing numerical techniques that are robust enough to handle non-linearities in the system of equations. Success of theories in predicting practical flows is dependent upon an accurate experimental determination of the properties of individual impacts.

H.Xu et all [44] suggested that the principal difference between granular flows and dense gases is that kinetic energy is dissipated in collisions. They considered cases in which the collisional energy dissipation is small (as assumed in the model of the granular capsule). They reviewed the equations of the kinetic theory for the conservation of mass, momentum, fluctuation energy, and species concentration. They illustrated their solutions for shear flows in rectilinear or axisymmetric rectangular channels with or without a body force.

The conservation laws of mass, momentum, and fluctuation energy for a collisional granular flow of identical spheres of diameter σ have been derived as [44, 45]:

$$\frac{\partial \rho}{\partial t} + \nabla (\rho u) = 0 \tag{32}$$

$$\rho \frac{\partial u}{\partial t} + \rho u . \nabla u = \nabla . T + \rho f \ , \tag{33}$$

$$\frac{3}{2}\rho\frac{\partial T}{\partial t} + \frac{3}{2}\rho u . \nabla T = -\nabla . q + T : \nabla u - \gamma \ , \tag{34}$$

where $\rho = \rho_s \nu$ is the density of granular fluid, ρ_s is the material density of the spheres, $\nu = \frac{\pi n \sigma^3}{6}$ is the particle volume fraction, n is the number density of spheres, u is the mean velocity, T is the stress tensor, f is the body force per unit mass, $T \equiv \frac{1}{3} < C . C >$ is the granular temperature, C is the particle velocity relative to the mean flow, q is the flux of fluctuation energy, and γ is the volumetric collisional dissipation rate of kinetic energy.

The stress tensor has the same form as in ordinary fluids [44]:

$$\mathrm{T} = \left[-P + \left(\lambda - \frac{2}{3}\eta \right) \nabla . u \right] I + \eta \left[(\nabla u) + (\nabla u)^{\mathrm{T}} \right] \tag{35}$$

where P is the pressure, I is the identity tensor, λ and η are the bulk and shear viscosity, respectively.

The flux of fluctuation energy satisfies Fourier's law [44]: -

$$q = -k \nabla \mathrm{T} \qquad (\equiv E_9) \tag{36}$$

where k is the conductivity of fluctuation energy.

For flows of smooth, slightly inelastic, identical spheres, Jenkins and Rickman [45] derived constitutive relations for pressure, transport coefficients, and energy dissipation rate. To the lowest order of $1 - e$, where e is the coefficient of restitution for collisions between two flow spheres, their results are

$$P = 4\rho FGT \ , \tag{37}$$

$$\lambda = \frac{8}{3\sqrt{\pi}}\rho\sigma GT^{1/2} \ , \tag{38}$$

$$\eta = \frac{8J}{5\sqrt{\pi}}\rho\sigma GT^{1/2} \ , \tag{39}$$

$$k = \frac{4M}{\sqrt{\pi}}\rho\sigma GT^{1/2} \ , \tag{40}$$

$$\gamma = \frac{24}{\sqrt{\pi}}(1-e)\rho\frac{T^{3/2}}{\sigma}G \ , \tag{41}$$

where $G = \upsilon g_o(\upsilon)$ and $g_o(\upsilon) = (2 - \upsilon) / [2(1 - \upsilon)^3]$ is the Carnahan and Starling [46] radial distribution function at contact for identical spheres. The functions F, J and M of υ are

$$F = 1 + \frac{1}{4G} \ , \tag{42}$$

$$J = 1 + \frac{\pi}{12}\left(1 + \frac{5}{8G}\right)^2 \ , \tag{43}$$

and

$$M = 1 + \frac{9\pi}{32}\left(1 + \frac{5}{12G}\right)^2 \ , \tag{44}$$

Jenkins and Chang [47] showed that these constitutive relations can be extended to nearly elastic, slightly frictional spheres. The expressions for pressure, viscosities and conductivity remain unchanged to the lowest order, while the additional dissipation of kinetic energy due to friction is taken into account by using an effective coefficient of restitution e_{eff} that replaces e in (41). Following Walton's simple impact model [48] and the experimental verification of Foerster et al [7], Jenkins and Chang [47] distinguished sticking (or rolling) collisions characterized by a coefficient of tangential velocity restitution β_0, and sliding collisions featuring a Coulomb friction coefficient μ that represents the ratio of the tangential and normal impulses in gross slip. For small $1 - e$ and small μ, they derived the coefficient of restitution

$$e_{eff} \equiv e - \frac{1}{2} a_1 + \frac{1}{2} a_2 \frac{b_1}{b_2}, \tag{45}$$

where

$$a_2 = \frac{5}{2}\frac{\mu}{\mu_0}\left[\frac{\pi}{2}\mu_0\left(1 - \frac{2}{\pi}\arctan\mu_0\right) + \frac{\mu_0^2 - \mu_0^4}{\left(1+\mu_0^2\right)^2}\right],$$

$$a_1 = \frac{\mu}{\mu_0}\left[\pi\mu_0\left(1 - \frac{2}{\pi}\arctan\,\mu_0\right) + \frac{2\mu_0^2}{1+\mu_0^2}\left(1 - 2\frac{\mu}{\mu_0}\right)\right],$$

$$b_1 = \left(\frac{\mu}{\mu_0}\right)^2 \frac{\mu_0^2}{1+\mu_0^2} \;;\; b_2 = \frac{1}{2}\frac{\mu}{\mu_0}\left[\frac{\pi}{2}\mu\left(1 - \frac{2}{\pi}\arctan\mu_0\right) + \frac{\mu_0^2}{1+\mu_0^2}\right]$$

and $$\mu_0 \equiv \frac{7\left(1+e\right)}{2\left(1+\beta_0\right)}\mu \tag{46}$$

6.5.4. Boundary Conditions; E_{10}

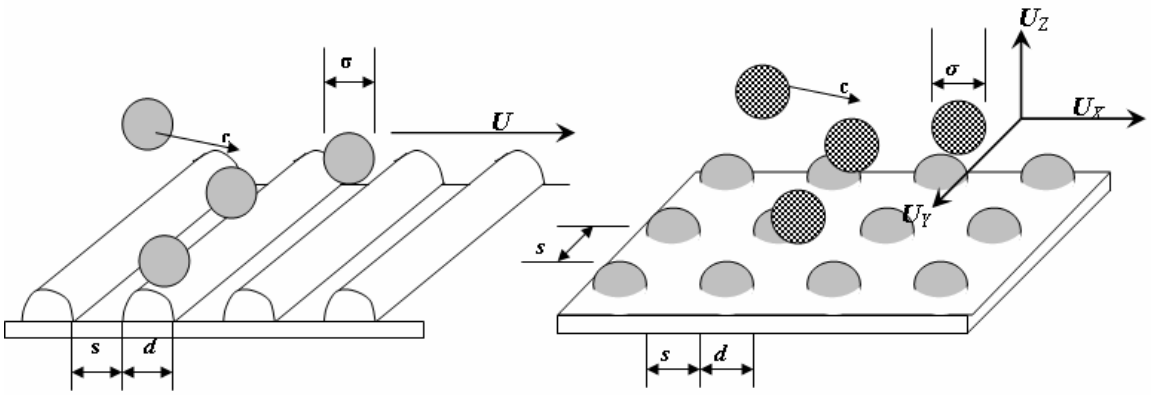

Figure 6.7: (i) Bumpy boundary – cylinders as illustrated by Jenkins et al (ii) Bumpy boundary – hemispheres.

At the interface between the granular flow phase and the lattice structures, there will be some energy flux implications as the lattice granules resist, and / or disintegrate to join, the flow. At the extreme limit, all the lattice granules will have joined the flow and the hemispherical bumps on the fascia and basal plate will be resisting the granular flow. The velocity gradient from the boundary walls to the central axis of flow conforms to a laminar flow, similar to Newtonian fluids.

Boundary conditions for the stress and energy flux are derived by considering changes in momentum and fluctuation energy of the flowing particles in their collisional interactions with the boundary [44]. In collisional granular flows, bumpy boundaries have long been regarded as a convenient way of imparting momentum and fluctuation energy to the flowing grains. Since all preceding calculations assumed that the relative mean "slip" velocity between the grains and the wall is small compared with the particle fluctuation velocity, Jenkins et al [45] extended these previous works to large slip. Accordingly, they calculated the wall stresses and fluctuation energy flux between a flow of smooth,

inelastic spheres and a bumpy wall featuring half cylinders of diameter d and separated by s as illustrated in Figure 6.7(i) above [44]. In the context of the granular capsule, Figure 6.7(ii), hemispheres are a good approximation of half cylinders in a bi-axial flow field, with

$\boldsymbol{d} = \boldsymbol{\sigma}$. As such, the analysis for boundary conditions may be approximated to be representative of both models in either flow direction.

From geometrical considerations, Jenkins et al [49] applied their results at a distance ½ (d + σ) away from the line of centers of the bumpy wall,

$$N^B = \frac{1}{2}(1+e_w)\rho\chi T\left(1+\frac{v^2\sin^2\theta}{3T}\right), \tag{47}$$

$$S^B = \frac{1}{2}(1+e_w)\rho\chi T\sqrt{\frac{2}{\pi}}\frac{v}{\sqrt{T}}(\theta\csc\theta-\cos\theta), \tag{48}$$

and

$$Q^B = \frac{1}{2}(1+e_w)\rho\chi T^{\frac{3}{2}}\sqrt{\frac{2}{\pi}}\left[(\theta\csc\theta-\cos\theta)\frac{v^2}{T}-\theta\csc\theta(1-e_w)\right]. \tag{49}$$

where N and S are the normal and shear stresses at the boundary, respectively, the superscript B denotes smooth bumpy cylindrical boundaries, Q is the fluctuation energy flux through the boundary into the flow, and e_w is the coefficient of restitution for collisions between a flowing sphere and the half-cylinders, v is the slip velocity, ρ and T are evaluated at ½ (d + σ) away from the wall, and $\theta \equiv \arcsin\left(\frac{d+s}{d+\sigma}\right)$ is a parameter characterizing the bumpiness of the boundary. The factor χ accounts for the effects of excluded area and collisional shielding on the collision frequency between the spheres and the boundary. Although the exact value of χ is not known, solutions of the governing

equations only require ratios of the shear stress or the energy flux to the normal stress, from which χ cancels out.

Assuming that the normal stress at a frictional, bumpy wall is the same as the normal stress at a frictionless bumpy wall, Xu [50] provided a stress ratio and a flux of fluctuation energy that are valid over a large range of dimensionless slip v / $\sqrt{T}$ for a frictional, bumpy boundary to be approximately,

$$N = \frac{1}{2}(1+e_w)\rho\chi T\left(1+\frac{v^2\sin^2\theta}{3T}\right), \tag{50}$$

$$\frac{S}{N} = \left(\frac{S}{N}\right)^B + \left(\frac{S}{N}\right)^F \tag{51}$$

and hence, $Q = Q^B + \Delta Q^F \quad \equiv \boldsymbol{E_{10}}$ (52)

where $$\left(\frac{S}{N}\right)^B = \sqrt{\frac{2}{\pi}}(\theta\csc\theta - \cos\theta)\frac{\frac{v}{\sqrt{T}}}{1+\frac{v^2}{3T}\sin^2\theta}$$

is the contribution of the bumps to the shear stress, and

$$\left(\frac{S}{N}\right)^F = \min\left(\frac{\sqrt{3}}{14}(1+\beta_{0w})\frac{v_{rel}}{\sqrt{T}},\ \mu_w\right)$$

is the frictional contribution. Q^B is given by (49) and

$$\Delta Q^F = \min\begin{pmatrix} NT^{1/2}\sqrt{\frac{\pi}{2}}\left[7\mu_w^2 - \frac{\pi}{2}\mu_w\left(1-\frac{v_{rel}^2}{3T}\right)\right] \\ NT^{1/2}\sqrt{\frac{\pi}{2}}\frac{7}{3}\mu_w^2 \end{pmatrix} \tag{53}$$

is the contribution to the energy flux due to friction only.

6.6. Base Plate: Bending moments, shear, compressive stress Energy

Figure 6.8 shows the cross-sectional view of base plate (Component D). Further assumptions made here include (1.) that negligible shear loading exists between the flat plate and the attached biasing hemispheres, and (2.) that the layer is expected to function strictly within its elastic limits, which are meant to be below or equal to those of the motor-vehicle structural panels. Its behavior may thus be generalized to that of a slender beam, whereby external work done by the impact force may be equated to the internal strain energy attributable to both bending and transverse shear stresses.

Figure 6.8: Component D with biasing hemispheres.

For a simply supported three point bending member of constant cross-section, the elastic strain energy due to bending, U_b, is given by [51];

$$U_b = \frac{P^2 L^3}{96EI} \tag{54}$$

where P is the load at a given point on the load deflection curve, L is the support span of the beam, E is the material's modulus of elasticity, and I the first moment of the cross-sectional area. For more precise results, this latter value may be moderated to account for the effect of hemispheres attached to the slender beam, thereby replacing I with a derived effective moment of area, $I_{eff.}$ The corresponding deflection, Δ_B, at the mid-point of the support span, may be determined by an energy method as;

$$\Delta_B = \frac{PL^3}{48EI} \tag{55}$$

where $I_{zz} = bh^3/12$ for a rectangular cross-section with breadth *b* and thickness *h*.

For the same loading set-up, the elastic strain energy due to transverse shear stress, U_τ, is given by [51];

$$U_\tau = \frac{fP^2Lh^2}{96GI} \tag{56}$$

where *f* is a form factor, equal to 1.2 for a rectangular cross-section. For most metals, G ≈ 0.4 E and it has been found that [51];

$$U_\tau = U_b\left(\frac{3h^2}{L^2}\right) \tag{57}$$

and for slender beams; L/h = 10, $U_\tau = 0.03U_b$ which may be neglected. Since the deformation of this member is limited to the allowable deflection of the automotive panels to which it will be attached, the insignificance of U_τ has been imposed. By virtue of the component being thin, the elastic strain energy absorbed through localized elastic compression has as well been considered negligible and hence neglected.

For generality with respect to constituent material diversity, we may combine Eqns. (54) and (57), to obtain:

$$E_{11} = U_b + U_\tau \quad = \frac{P^2L^3}{96I}\left[\frac{1}{E} + \frac{f}{G}\left(\frac{h}{L}\right)^2\right] \tag{58}$$

For the conceptual automotive bumper system, the energy absorbed and dissipated according to Eqn. (1) may now be expressed as:

$$\mathbf{E_T = E_3 + E_5 + E_6 + E_7 + E_8 + E_9 + E_{10} + E_{11}} \tag{59}$$

where the respective values of $\mathbf{E_i}$ are as given by Equations (3), (11), (12), (26), (31), (36), (52) and (58) respectively.

6.7. Conclusions

Of the eight components in equation (59), some modes are absorptive while others are dissipative. Calculations based on experimental data and dimensions indicated that a greater percentage of the incident impact energy is dissipated, the rest being absorbed and released later after the impact load is removed. Bearing in mind that the system recovers dimensionally after unloading, these results represent a potential breakthrough into non-destructive impact energy management. As mentioned during the system's experimental validation stage, further works need be done in order to optimize the system by harnessing these absorption/dissipation mechanics to preferred proportions. This may be supplemented by optimal selection of materials and dimensional analysis, preferably in conjunction with discrete element simulation analysis.

CHAPTER 7:

PROTOTYPING AND DAMAGE MECHANISMS:

7.1. Introduction

Federal Motor Vehicle Safety Standards (MVSS) and Canadian Motor Vehicle Safety Standards (CMVSS) test velocity for automotive bumpers is 8km/h. The stipulated test velocity for side impact protection is 54 km/h. In the real-world crash circumstances, vehicles travel at velocities above these values. Therefore a prototype of the proposed system was tested at speeds closer to real-world bumper situations. To this end, a sample representing the longitudinal sections of a full-scale bumper was manufactured and tested for failure. Damage analysis was done on the sample after it was subjected to a drop weight impact. ISO 6603-2 has been used as a guideline to this non-standardized test [35].

7.2. Sample preparation:

Figure7.1 : A Prototype Capsule – Top view.

Figure 7.1 shows the prototype's capsule before being filled up with glass beads. The capsule was fabricated from 1mm thick tyre tube material using a similar process as in Chapter 4. The capsule dimensions were Ø 100 x 300mm long. In order to avoid pre-

stretch, the capsule was filled with 1, 040 spherical glass beads having a diameter of 16 ± 0.2mm. Beads were lubricated with a thin layer of petroleum jelly.

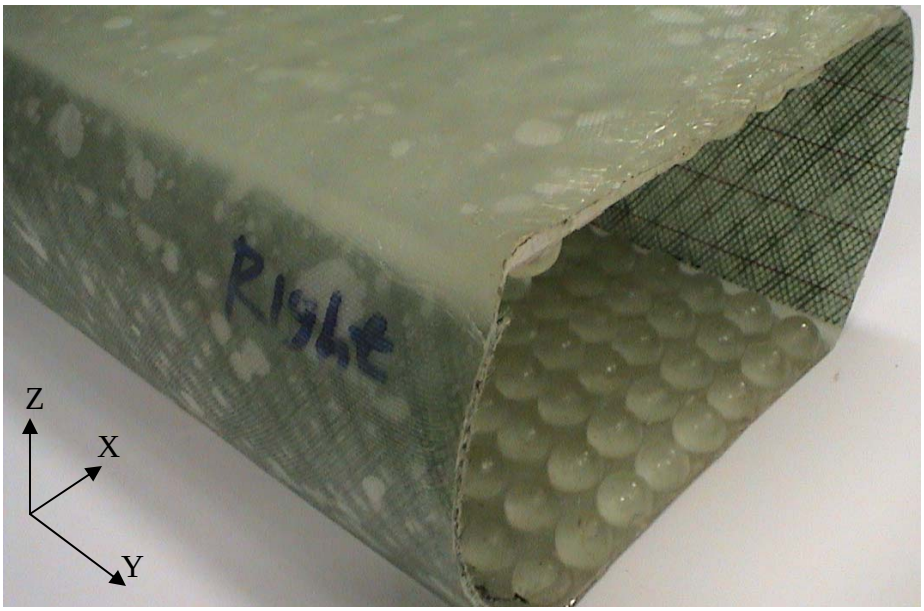

Figure 7.2(i): Experimental Prototype Casing – Pictorial view.

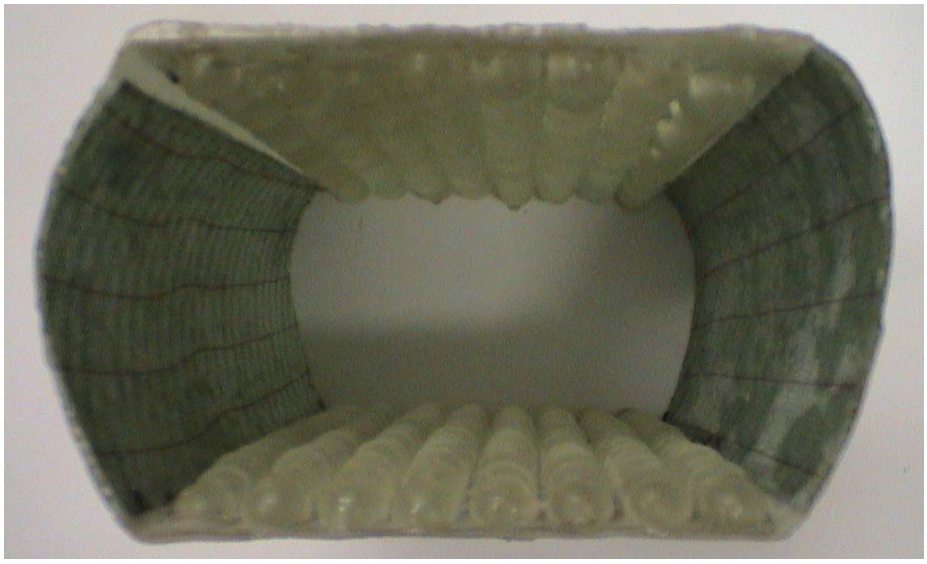

Figure 7.2(ii): Perspective Side-view of Prototype Casing.

Figure 7.2(i) shows a pictorial view of the experimental prototype casing while Figure 7.2(ii) shows a perspective side view of the casing, showing hemispheres lining the interior fascia and base walls. X-Axis as indicated in Figure 7.2(i) represents the lateral

axis, Y-Axis the longitudinal axis, and Z-Axis the (transverse) axis of impact incidence. The casing was moulded as one piece through a multi-step hand lay-up process. The top side was reinforced with 6 layers of woven glass fibre, while the base has 10 layers. Side walls have 3 layers with the intention of having more flexibility in the direction of impact, so as to direct more of the impact energy to the core itself. The optimal number of layers or design of casing is subject to an optimization process beyond the scope of current research. The same combination of epoxy resin – hardener system is used as described in Chapter 4, including the curing method. External dimensions are 280mm x 150mm x 120mm (L x W x H). Gap between biasing hemispheres on the fascia interior and those on the base wall was measured to be 90mm. Both fascia and base wall surface area carried 128 hemispheres each {8 rows (W) x 16 columns (L)}.

7.3. Procedure:

A 50mm sandwich panel of corrugated paper cardboards was used as a loading platform for the prototype. This was selected to simulate deformable vehicle body panels. Drop weight test was performed from a drop height of 2300mm, delivering a 6.72 m/s (24.18 Km/h) velocity just before impact. A cylindrically profiled impactor head {Ø180mm x 200mm (L)} weighing 50 Kg was used. The sample was set-up in such a way that its longitudinal axis was perpendicular to the central axis of the cylindrical impactor head. Damage assessment was evaluated on basis of physical examination of the sample immediately after impact.

In an effort to track down the deformation behaviour during impact, a SONY® Digital Handycam with 120x digital zoom is used to record the impact. It was positioned

approximately 3m away from the sample set-up area for safety reasons. Walls of the casing were marked for ease of identifying any changes during the damage assessment.

7.4. Results and Discussion:

It was expected that the casing, encapsulating membrane and the glass beads will absorb the impact energy to different extents. Since facilities available for tracing the deformation and damage mechanisms were limited, analysis of the physically visible form of failure was considered to be indicative of the underlying mechanisms. Visual images before and after impact were analysed. The analysis is shown here in three sections; the casing, capsule, and the platform. These sections are representative of three main domains of the proposed system's design.

7.4.1. The casing

The casing forms a boundary around the core. It also serves as an interface between the impacting object and the vehicle. An understanding of its damage can therefore help in the review of its design for optimal performance of the bumper system as a whole.

The impactor was centrally aligned, with its central axis lying perpendicular to the longitudinal axis of the casing. The unevenness of the edges has negligible effect(s) on the casing's performance.

Corresponding views of the casing's exterior walls *before* and *after* impact loading are shown as (i) and (ii) respectively in Figures 7.3 – 7.6. All walls of the prototype were inspected before impact loading. Randomly scattered light patches are evident, indicating inter-laminate air entrapment during the hand lay-up process. It was expected that these patches would potentially lower the structural strength of the prototype. However, there appears to be no such cause-effect relationship.

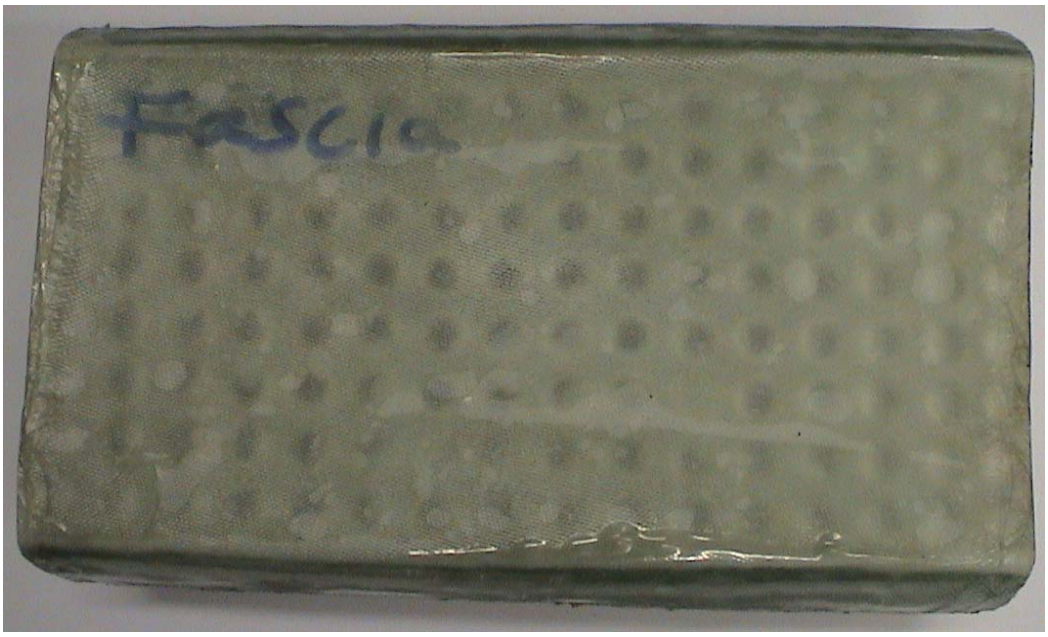

Figure 7.3(i): Fascia Wall *Before* Impact.

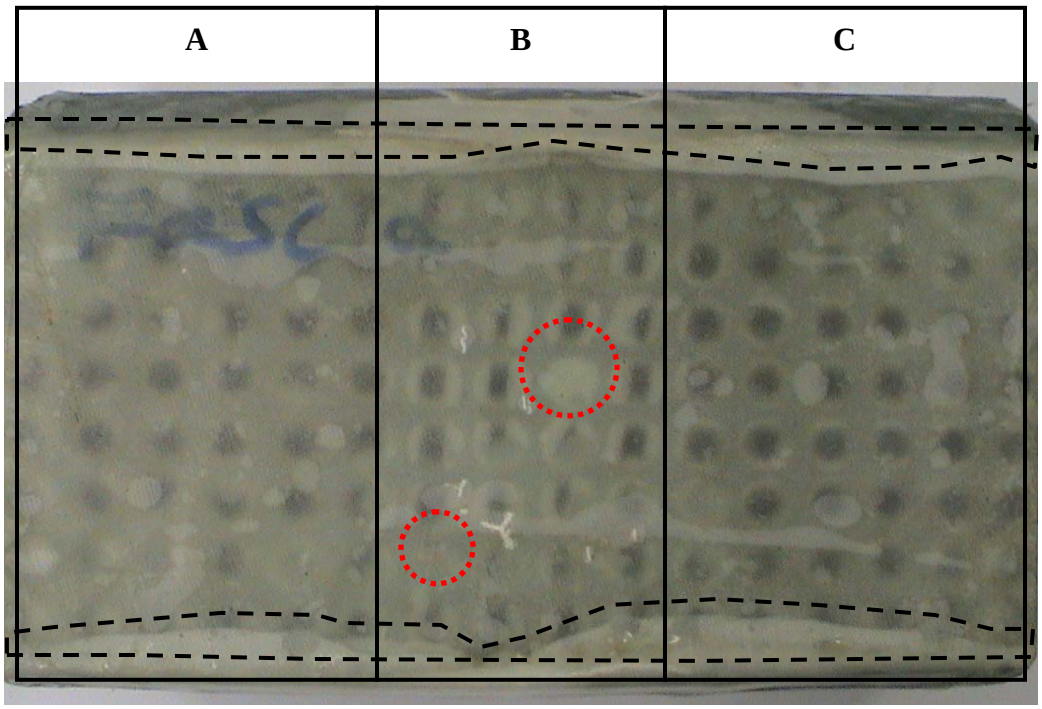

Figure 7.3(ii): Fascia Wall *After* Impact.

Dotted lines mark bands of interlaminate delamination. Given that these bands run longitudinally to both ends of the section, it means that the delamination was mainly

attributable to forced opening of hinged boundaries between fascia and side walls. The bands are relatively wider in partitions A and B as marked out in Figure 7.3(ii) and narrowing down towards the lateral central axis of partition B. A similar tendency is visible towards both longitudinal ends of the prototype. This variation in delamination band width may be a reliable indicator of shear stress distribution within the fascia.

The darker, spots on the fascia are the reverse views of biasing hemispheres that line the interior. These spots are more distinct on the fascia wall than on the base wall and this is due to there being more reinforcement fibre layers in the latter (shown later in Figure 7.4(i). Partition B shows hemispheres' that are bordered with delamination. The hemisphere location circled in dotted line indicates an extreme case of all-round delamination. These bands of delamination appear to be almost straight and aligned to the lateral axis. Since the central axis of the cylindrical impactor head was also in the lateral direction and no similar bands appear in partitions A and C, it can be concluded that the fascia deformed primarily through flexural bending about the lateral axis. Another contributing factor is that the relatively more rigid hemispheres themselves were not individually reinforced along with the fascia wall, thereby being susceptible to detachment.

Unlike the fascia wall, there are no visible signs of delamination on the base wall except for longitudinal bands at the respective hinged boundaries with side walls. As with the fascia, these delamination bands emanate from forced flexure of the hinged joints. Uniformity of surface features before and after the impact especially around the hemispheres indicates that the base wall does not undergo any significant deformation. It

also indicates that very little or no impact load was transferred to the base wall. It could also be relatively less sensitive to the impact energy sharing amongst the system's components because it has more reinforcement. Views of the base wall are shown in Figures 7.4(i) and (ii). The difference in clarity of hemispheres' transparency images is due to lighting effects.

Figure 7.4(i): Base Wall *Before* Impact.

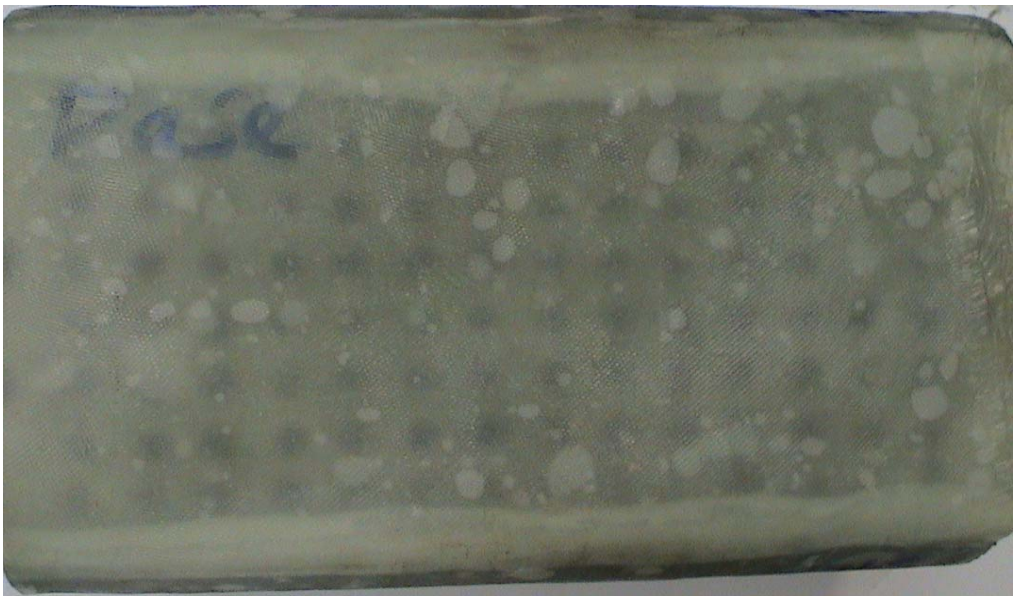

Figure 7.4(ii): Base Wall *After* Impact.

The side walls were damaged the most. These walls act as struts supporting the fascia. Should their flexural capability be inadequate, then there are high chances of longitudinal failure. This failure would most likely occur either at the top (fascia), or at the bottom (base wall), or along the longitudinal central axis, or at any combinations of the three locations.

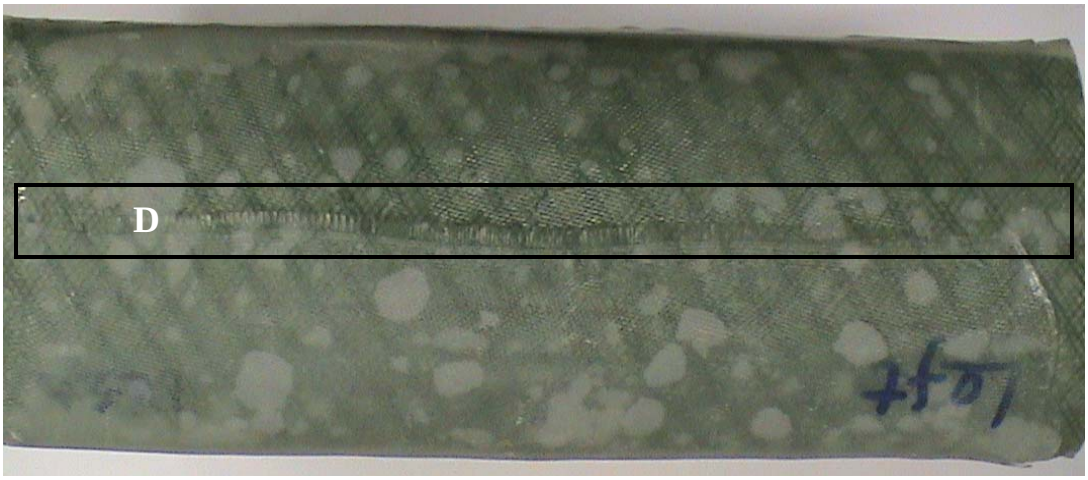

Figure 7.5(i): Left-side Wall *Before* Impact.

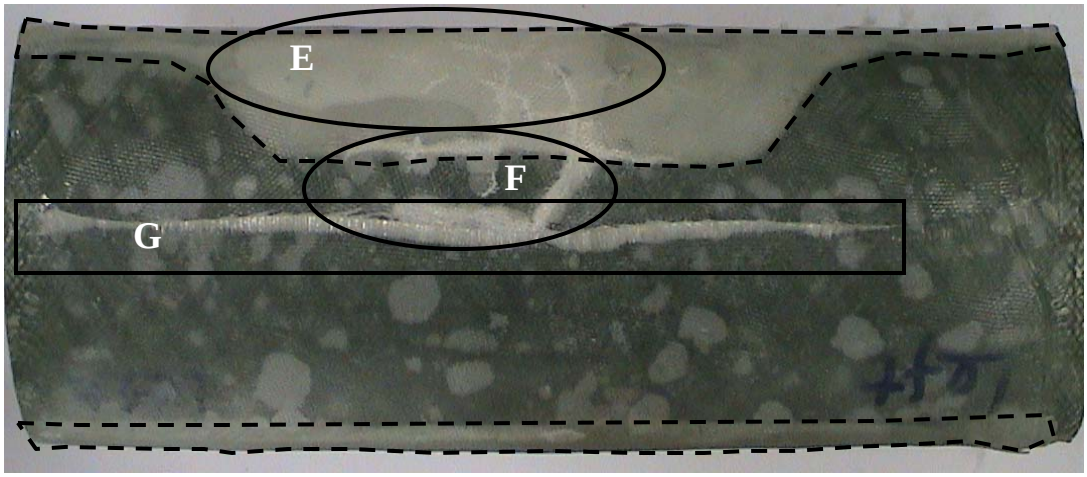

Figure 7.5(ii): Left-side Wall *After* Impact.

Partition D shows the edge-line of the last fibre reinforcement laminate wound around the casing. This edge-line does form a delamination front as highlighted in partition G in Figure 7.5(ii). This shows shear stress concentration about the wall's longitudinal central

axis. The stress is nevertheless significantly lower as implied by proportionate damage at the top and bottom. This may be attributed to the curved profile meant to allow easy bending in the transverse direction. The flexure allows transfer of impact load from fascia to the primary energy absorbing and/or dissipating core (encapsulated granular layer). It also acts as a spring, partly contributing towards dimensional recovery of system's profile.

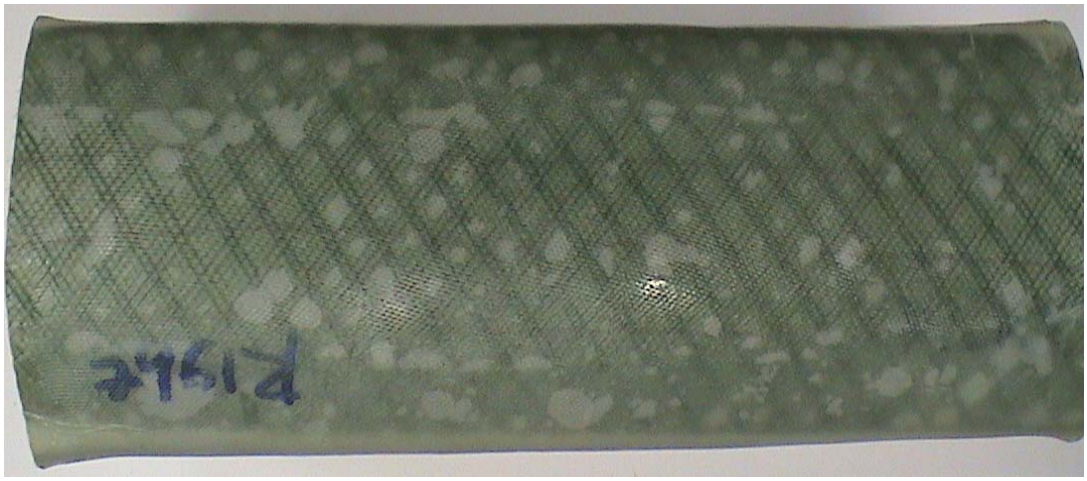

Figure 7.6(i): Right-side Wall *Before* Impact.

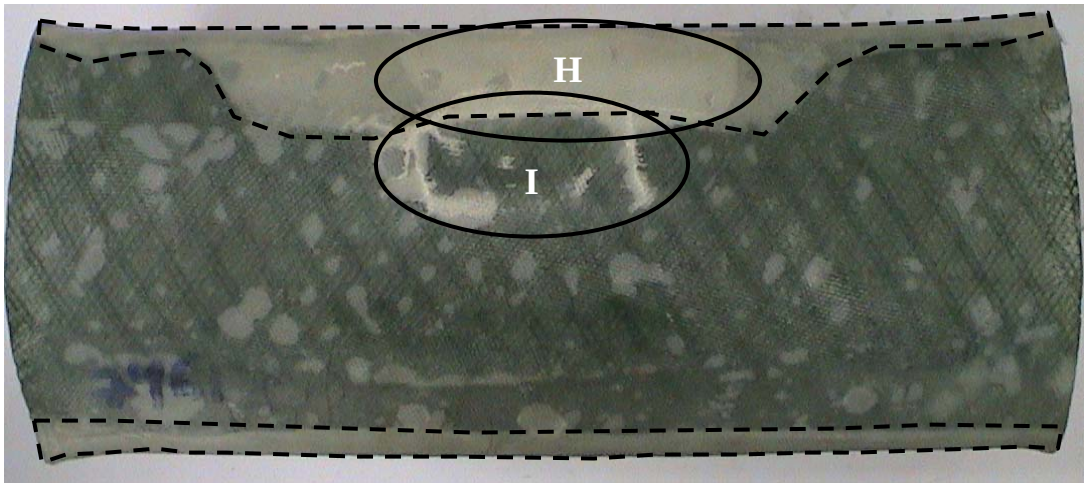

Figure 7.6(ii): Right-side Wall *After* Impact.

Figures 7.5(ii) and 7.6(ii) show that both side walls also failed at the top and bottom boundaries. Top boundaries incurred much more damage (interlaminate delamination)

than the bottom boundaries as highlighted in dotted lines. The damage is almost symmetrical. Partitions E and H highlight regions of relatively greater interlaminate delamination, most probably involving shear failure between the fibre layers. Partitions F and I show an outline of reinforcement fiber break-out.

Damage in these regions suggests failure under three transverse regimes: (1.) Initial delamination as the impactor compresses the side. At this stage, the delamination is primarily along the longitudinal hinged boundary. (2.) Further delamination occurs as the impactor imparts its profile onto the casing. Having undergone it maximum flexure, the side walls then tend to behave like rigid beams undergoing bending about the lateral axis. The rigidity is enhanced by support from the continuously deforming core. In addition to delamination in the first regime, other layers enter the delamination process. The side walls enter this regime at the same time with the fascia due to their being relatively weaker than the fascia in terms of fibre reinforcement layers. (3.) Once the pseudo-beams (side walls) reach their ultimate load, the reinforcement fibre fractured. These three regimes are progressive, and occur during the full cycle of transverse deformation of the entire system.

Upon removal of capsule from the casing, two hemispheres of the 128 are fully detached from the fascia wall. Figures 7.7(i) and (ii) show the damage views. Spots circled in dotted line in Figure 3(ii) have been identified as their original locations. Hemisphere (i) has been linked to the spot marked with relatively bigger circle. Voids (circled-out in Figure 7.7) extending from their plane surface to the body of these hemispheres may be responsible for the detachments. The plane surface of hemisphere (i) show a texture

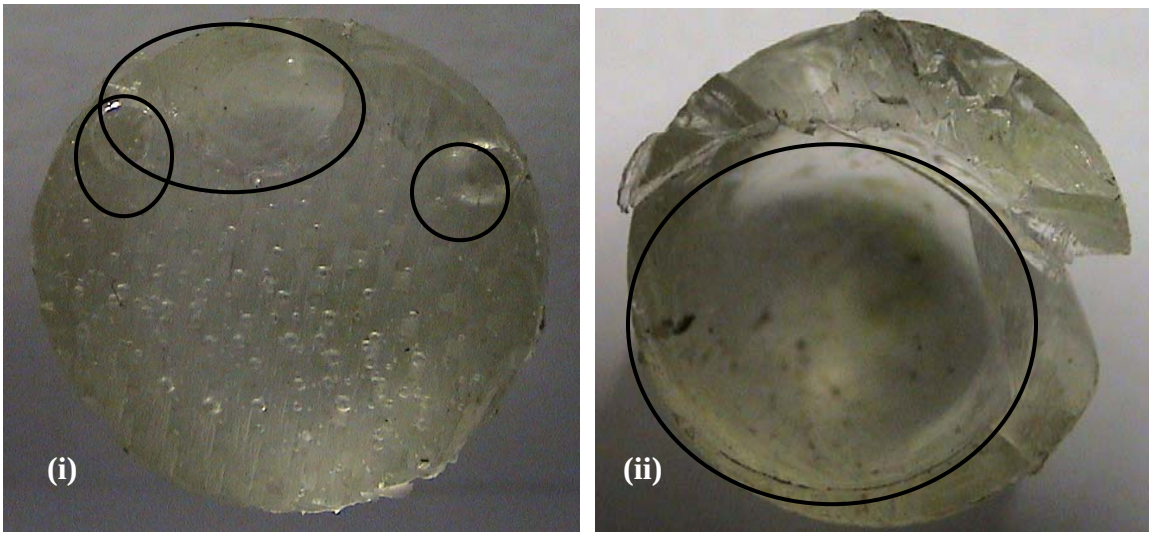

Figure 7.7: Sheared (i), and Fractured (ii) hemispheres.

comprising of patterned imprints conforming to an interface between matrix and woven fibre reinforcement laminate. This relates to detachment through delamination. On the contrary, surface texture for hemisphere (ii) is characterized by sharp edges typical of brittle fracture. Since the two hemispheres were in close proximity to each other, it is expected that the size of voids determined the failure mode.

From the foregoing analysis, it is evident that the casing absorbed and dissipated some of the impact energy. The absorption was through elastic deformation while dissipation was through delamination and fracture. These modes of damage can however be minimized through improved manufacturing methods, structural design, and materials engineering and/or selection.

7.4.2. The capsule

The capsule constitutes two parts; *encapsulating membrane* and the *encapsulated glass beads*. The two parts work in unison as one, behaving like a highly deformable physical solid. Failure of one of the parts may precede the other, thereby indicating a need for

individualized evaluation. While such evaluation may be related to the properties of respective material, it does not undermine the synergistic behaviour of the capsule as a whole.

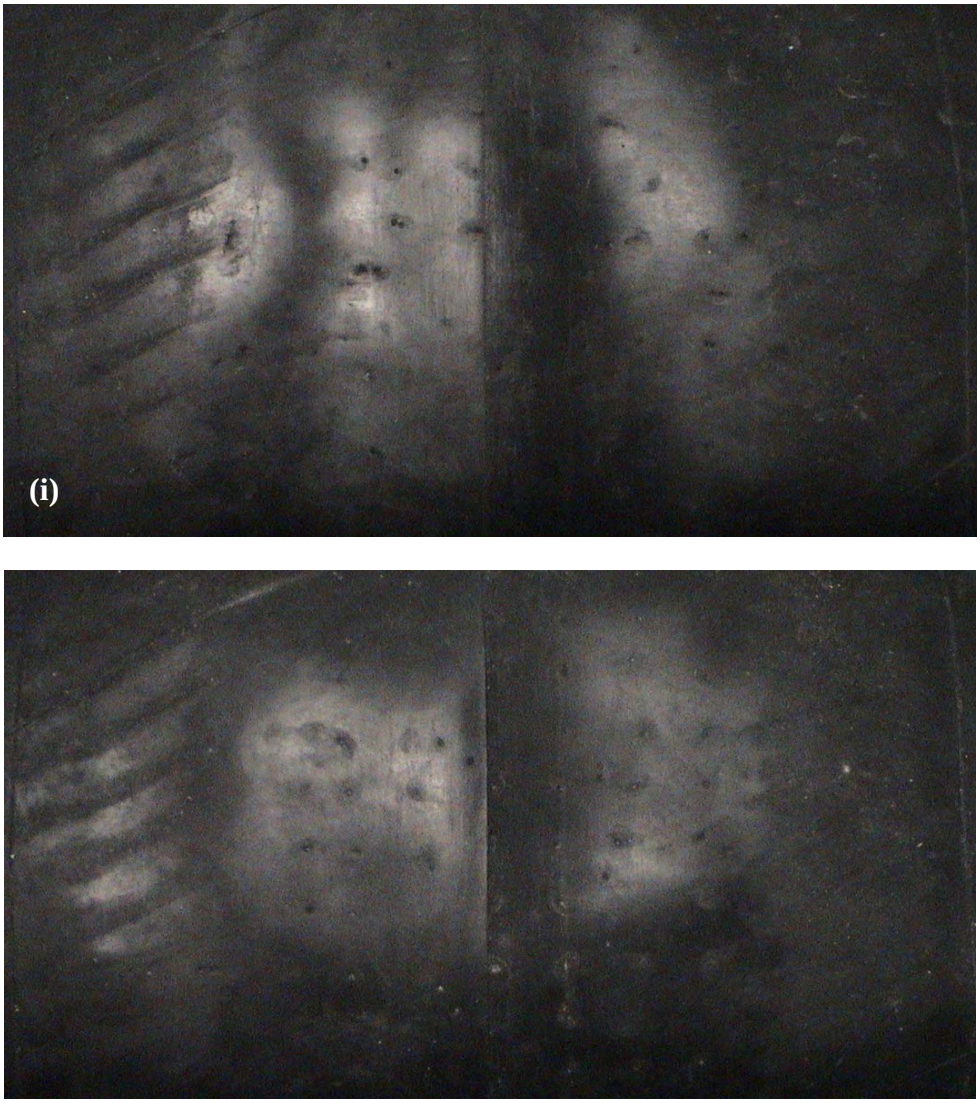

Figure 7.8: Surface of membrane facing interior of fascia (i) and base wall (ii).

Figure 7.8 (i) and (ii) show the face of encapsulating membrane bordering the interior side of fascia and base wall respectively. The images were captured on corresponding regions of the capsule on its respective sides. Both surfaces show pore-like piercing. This may have resulted from: (1.) direct compression of membrane between hemispheres and

encapsulated glass beads, and (2.) Localized stretching of the membrane. Either of the two events could have preceded the other, or they could have occurred simultaneously. Since the piercing is not patterned into any linear manner as the arrangement of hemispheres, these events must have occurred during a transition phase as the encapsulated beads sought to slot into the intended locations in alignment with fascia's biasing hemispheres.

It is evident that the extent and severity of piercing is almost the same on both sides. Subject to allowable deformation modes, this similarity confirms that the base plate behaves in a responsorial manner to the fascia. The base plate initiates an impulse wave that is essentially reactive to the one initiated by the fascia upon impact load interception.

Re-run of video-recording of the experiment has identified three stages of the impact: (1.) the impactor deform the system transversely. During this stage, sides of the cardboard platform rise above the bottom longitudinal edges of the prototype. This is accompanied by deformation of the prototype as a whole (2.) The impactor bounces back into air and the system seem to simultaneously bounce back to its initial shape. (3.) Being a drop weight test, the impactor goes down on the prototype and comes to rest after a few short bouncing oscillations.

From visual inspection, all the 1040 encapsulated glass beads remained intact after impact. Based on hemispheres encompassed within partition B of the fascia {Figure 7.3(ii)}, approximately 32 encapsulated beads participated in interception of the impact load. This number is further reduced by virtue of the capsule's curved profile especially in the longitudinal and lateral directions. The reduction is a general design limitation

relating to longitudinal span of the prototype. It can however be circumvented or minimized by reducing the height of frustums at both free ends of the capsule.

It can be said that deformation of the capsule, which represents bulk flow of the encapsulated glass beads, is a form of impact energy management. The flow integrates granular movement through spinning, sliding, inter-granular collisions, and shear flow as discussed in earlier chapters. These diverse granular mechanics in effect reduces the capsules susceptibility to damage or ultimate failure. The capsules deformability depends on the encapsulating membrane capacity, and consequently the ability to 'absorb' energy over a relatively larger strain than typical rigid and/or foam structures. In light of the magnitude of impact load used on the prototype and the impact velocity, it is imperative that the capsule could take even a higher magnitude of impact energy.

7.4.3. The platform

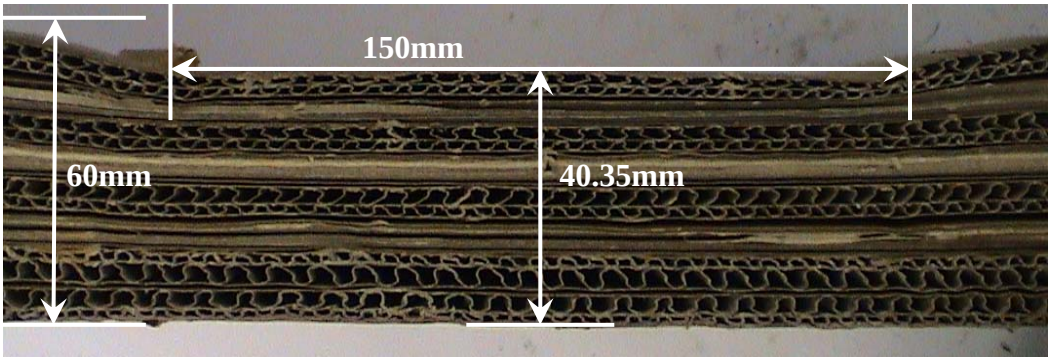

Figure 7.9: Paper corrugated sandwich.

Figure 7.9 shows transverse deformation view of the paper corrugated sandwich panel. The 150mm span corresponds to the lateral axis of the casing's base wall. Its transverse measurements before and after impact indicate a 19.65mm deformation, i.e. approximately 33% compression. It is suggested that a greater proportion of this deformation occurred due to impact load transmission by the side walls directly to the

platform. This happened as the side walls experienced the three failure regimes as suggested earlier on. Since total recorded transverse deformation of platform and prototype was 42mm, this interprets to 22.35mm deformation of the latter at resting position. However, the prototype fully recovered its dimensional profile as ascertained through measurements of the gap between interiors faces of fascia and base wall immediately after the load is removed.

A follow-up drop-weight test was run with weakened side walls as shown in Figure 7.10. The corresponding compressed thickness was 44.40mm, representing 26% compression. This indicates that more impact energy can be directed to the core (capsule) by appropriate design of the casing, thereby reducing the residual amount of impact energy that is transferred to the vehicle.

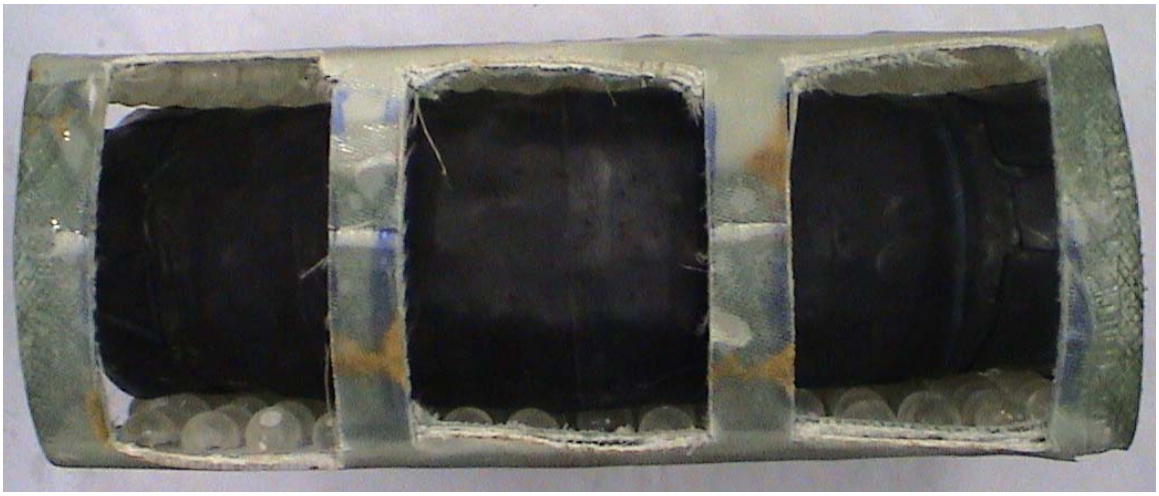

Figure 7.10: Prototype casing with weakened side walls.

The reduced damage on the platform reiterates the view that a rigid capsule would tend to transfer impact load direct to the vehicle instead of the core. This unfavourable tendency can however be minimized by appropriate design as mentioned earlier.

7.5 Conclusions and recommendations:

Typical automotive bumper systems rely mainly on impact energy absorption. This implies reliance on properties of the constituent materials, usually designed into rigid structures. In this study an alternative system has been proposed, characterizing a shift from this traditional design focus. The proposed system relies mainly on non-destructive impact energy dissipation. This is achieved through a process of optimizing the characteristic dissipative mechanics of granular media.

Two theoretical models have been developed around the proposed system; (1.) impulse wave propagation model, and (2.) impact energy management model. The first model indicates that granular media can be used effectively to re-direct the impulse wave away from its axis of incidence. The resulting effect is that the impulse wave is attenuated before reaching the back side of the system. The second model demonstrated that impact energy is shared amongst the individual components of the system, with a relatively greater proportion of the energy being dissipated through non-destructive granular mechanics. These mathematical models have been validated by experimentation on a scaled model. In the low-to-medium velocity regime, the system fully recovers dimensionally after impact. Theoretical indications are that these findings will be reproduceable on a full scale model.

Future work should be on full scale automotive bumpers and should be based on the failure mechanisms as identified. It is recommended that attention be given to the following areas: (i.) the nature of contact between hemispheres and the respective walls to which they are attached, (ii.) weight and impact properties of the granular media, (iii.)

optimal properties of the encapsulating membrane material, (iv.) appropriate lubrication (v) flexibility of the fascia to maximize localized deformation (vi) integration of the proposed system into currently existing bumper systems, (vii.) simulation on stress and energy distribution at various points of contact and points of impact loading, and (viii) optimization of the entire system through dynamic simulation.

REFERENCES

1. BMW Bumpers - Car Parts Wholesale. [Online]. Available: http://www.carpartswholesale.com/cpw/bmw~bumpers.html, [Accessed 6 January 2007].

2. Plastics Car Bumpers & Fascia Systems. [Online]. [2004]. Available: http://www.plastics-car.com/s_plasticscar/doc.asp?CID=418&DID=1332, [Accessed 6 January 2007]

3. Drew Winter. 1994. The Bumper Materials War – Plastics Increasingly Used in Automobile and Light Truck Bumpers. [Online] Available: http://www.findarticles.com/p/articles/mi_m3165/is_n1_v30/ai_14979251, [Accessed 6 January 2007].

4. Consumer Bumper Quality Disclosure Bill. [Online]. 2004. Available: www.smartmotorist.com/bum/bum.htm, [Accessed 6 January 2007].

5. Fascia (Car). [Online]. 2007. Available: http://en.wikipedia.org/wiki/Fascia_(car), [Accessed 7 January 2007].

6. Jeep Cherokee Front Bumpers. [Online]. 2005. Available: http://www.innerauto.com/Jeep_Parts/Jeep_Cherokee_Parts/Jeep_Cherokee_Bumpers, [Accessed 7 January 2007].

7. Carpenter, K.H. and Kerr, L.L. 1973. The 1973 General Motors Hydraulic-Pneumatic Energy Absorber Bumper System. SAE Preprints, (n730031): 8p.

8. ERG: Duocel® – Impact Energy Absorption Information. [Online]. Available: http://www.ergaerospace.com/foamproperties/applicationguide/energy.htm, [Accessed 26 January 2009].

9. Lampinen B.E. and Jeryan R.A. 1982. Effectiveness of Polyurethane Foam in Energy Absorbing Structures. SAE Preprints, 820494p.

10. Journal article: P.R. Stupak, J.A. Donovan - Geometry, Load Spreading, and Polymeric Foam Energy Absorber design: SAE Technical Paper Document No: 920333

11. Weller, Peter A. 1973. Urethane Energy Absorbers for Automobile Bumpers. American Chemical Society, Division of Rubber Chemistry, Papers, v2 (n730025): 21p.

12. Niebylski L.M., Fanning R.J. 1972. Metal Foams as Energy Absorbers for Automobile Bumpers. Wire, May 22-26: 7p.

13. Evans, Darin A. and Morgan, Terry. 1993. Engineering Thermoplastic Energy Absorbers for Bumpers. Polymer Engineering and Science, v33 (n21): 1381-1389.

14. Shuler, S., Santhanam, S. and Chaudhari, T. 1995. Use of Parametric Modelling in the Development of Energy Absorber Applications. International Solar Energy Conference, v1: p691-697.

15. Journal article: Kay Ogiyama, Jongneung Hyun, Inwon Chang - Beamless Bumper System: SAE Technical Paper Document No: 2003-01-0212.

16. Journal article: Michael E. Carley - Advancements in Expanded Polypropylene Foam Energy Management for Bumper Systems: SAE Technical Paper Document No: 2004-01-1700.

17. Journal article: Joel Santella, Andrew Day, Dan Moore - Energy Transfer Characteristics of Thermoplastic Bumper Beams in a Pendulum Impact: SAE Technical Paper Document No: 920523.

18. Alghamdi A.A.A. 2001. Collapsible Impact Energy Absorbers: an Overview. Thin Walled Structures 39(2001): 189-213.

19. Hamidreza Z., Matthias K. 2006. Optimum Honeycomb Filled Crash Absorber Design. Materials and Design (2006).

20. Africa Road Safety Review Final Report. [Online]. Available: http://safety.fhwa.dot.gov/about/international/africa/africa.htm, [Accessed 26 January 2009].

21. Journal article: David Andrew Aylor, Danny L. Ramirez, Matthew Brumbelow, Joseph M. Nolan - Limitations of current Bumper Designs and Potential Improvements: SAE Technical Paper Document No: 2005-01-1337.

22. Uehara, J.S., Ambroso, M.A., Ojha, R.P., and Durian, D.J: Low speed impact craters in loose granular media. Phys Rev Lett. 2003 May 16;90(19):194301. Epub 2003 May 13.

23. Amato, J. and Williams, R. American Journal of Physics, 66, 141(1998).

24. Mechanics of Granular Material. [Online]. Available: http://Science.nasa.gov/NEWHOME/headlines/pdf/MGM.pdf, [Accessed 10 May 2007].

25. Mechanics of Granular Materials. [Online]. Available: http://bechtel.colorado.edu/~batiste/microg/microg.html,[Accessed1Oct 2007].

26. Nicodemi, M., Coniglio, A., and Herrmann, H. J.: The compaction in granular media and frustrated Ising Models. J. Phys. A: Math. Gen 30 No 11 (7 June 1997) L379 – L385.

27. Zenkert, D., The Handbook of Sandwich Construction, Chameleon Press Ltd, London, United Kingdom, 1997.

28. Polypropylene foam parts for automotive applications. [Online]. Available: http://www.sovereign-publications.com/fageradala.htm, [Accessed 23 January 2009].

29. Material specific properties of Duocel® foams. [Online]. Available: http://www.ergaerospace.com/foamproperties/matspecificproperties.htm, [Accessed 23 January 2009].

30. Granular material. [Online]. Available: http://en.wikipedia.org/wiki/Granular_material, [Accessed 16 January 2009].

31. Emilien, A, Farhang, R, Robert, P, and Gilles, S.: Influence of particle shape on shear stress in granular media. eprint arXiv:0709.2241 (Sept 2007).

32. Evesque, P.: Stress propagation in granular media: Breaking of any constitutive state equation relating local stresses together by a change of boundary conditions. Poudres & Grains 7, 1 – 18 (October 1999).

33. Dalton, F, Farrelly, F, Petri, A, Pietronero, L, Pitolli, L, and Pontuale G.: Shear Stress Fluctuations in the Granular Liquid and Solid Phases. The American Physical Society. PRL 95, 138001 (2005).

34. Fluid Mechanics and Fluid Properties. [Online]. Available: http://www.cartage.org.lb/en/themes/sciences/physics/Mechanics/FluidMechanics/FluidMechanics/NatureFluids/NatureFluids.htm, [Accessed 23 January 2009].

35. ISO 6603-2: Puncture Impact Behaviour of Rigid Plastics.

36. Srinath, L. S.: Advanced Mechanics of Solids. Fourth Reprint, 1987, Tata McGraw-Hill Publishing Company Ltd.

37. Steigmann, D. J.: Thin-plate theory for large elastic deformations. International Journal of Non-Linear Mechanics. 42, Issue 2, March 2007, Pages 233-240.

38. Steigmann, D. J.: Asymptotic finite –strain thin-plate theory for elastic solids. Computers and Mathematics with Applications. 53 (2007) 287 – 295

39. Kuo Kang Liu and Bing Feng Ju: A novel technique for mechanical characterization of thin elastomeric membrane. Journal of Physics D: Applied Physics, 34 No. 15, L91-L94 (7 August 2001).

40. Nicodemi, M., Coniglio, A., and Herrmann, H. J.: The compaction in granular media and frustrated Ising Models. J. Phys. A: Math. Gen 30 No 11 (7 June 1997) L379 – L385.

41. Maw, N., Barber, J. R. and Fawcett, J. N.: The oblique impact of elastic spheres. Wear 38, 101 (1976).

42. Walton, O. R.: Granular solids flow project. Quarterly Report, January – March 1988, UCID-20297-88-1, Lawrence Livermore National Laboratory, 1988.

43. Foerster, S. F., Louge, M.Y., Chang, H., Allia, K.: Measurements of the collision properties of small spheres. Phys. Fluids A6, 1108 – 1115 (1994).

44. H.Xu, M. Louge, A. Reeves: Solutions of the kinetic theory for bounded collisional granular flows. Continuum Mech. Thermodyn. (2003) 15: 321 – 249.

45. Jenkins, J.T., Richman, M.W.: Grad's 13-moment system for a dense gas of inelastic spheres. *Arch. Rat. Mech. Anal.* 87, 355 – 377 (1985).

46. Carnahan, N.F., Starling, K.E.: Equation of state for non-attracting rigid spheres. *J. Chem. Phys.* 51, 635 – 636 (1969).

47. Jenkins, J.T., Chang, C.: Kinetic theory for identical, frictional, nearly inelastic spheres. Phys. Fluids. 14, 1228 – 1235 (2002).

48. Walton, O.R.: Numerical simulations of inelastic, frictional particle-particle interactions. In: Roco, M.C. (ed.): Particulate Two-Phase Flow, pages 884 – 911. Butterworth-Heinemann (1993).

49. Jenkins, J.T., Myagchilov, S., Xu, H.: Nonlinear boundary conditions for collisional grain flows at bumpy, frictional walls. *under review* (2002).

50. Xu, H.: Studies of gas-particle interactions in microgravity. PhD dissertation, Cornell University, Ithaca NY 14850, USA (2003).

51. Strain energy methods. [Online]. Available: me.queensu.ca/courses/MECH422/Lecture13.ppt, [Accessed 12th Nov. 2007]

LIST OF PUBLICATIONS

Publications

1. **Patent Rights: Impact Energy Management System:**

   Filed through the DUT's Directorate of Technology Transfer and Innovations.

2. **Mwangi F. M and Kanny K.: Development of Granular-Medium-Based Energy Management System for Automotive Bumper Applications: International Journal of Computers and Structures: Computational Structures Technology - CST 2008 (Special Issue) –** ***Under Review***

3. **Mwangi F. M and Kanny K.: Impulse Wave Propagation Through Granular Composite Structures: Mathematical Model: International Journal of Impact Engineering –** ***Under Review***